An NKX2-1/ERK/WNT feedback loop modulates gastric identity and response to targeted therapy in lung adenocarcinoma

Rediet Zewdu[1,2]; Elnaz Mirzaei Mehrabad[1,3]; Kelley Ingram[1,4]; Pengshu Fang[1,4]; Katherine L. Gillis[1,4]; Soledad A. Camolotto[1,2]; Grace Orstad[1,4]; Alex Jones[1,2]; Michelle C. Mendoza[1,4]; Benjamin T. Spike[1,4]; Eric L. Snyder[1,2,4]

1. Huntsman Cancer Institute,

2. Department of Pathology, University of Utah, Salt Lake City, UT 84112

3. School of Computing, University of Utah, Salt Lake City, UT 84112

4. Department of Oncological Sciences, University of Utah, Salt Lake City, UT 84112

Corresponding author: eric.snyder@hci.utah.edu

Key words: Lung adenocarcinoma, Targeted therapy, Lineage switching, NKX2-1, ERK, WNT

ABSTRACT

Cancer cells undergo lineage switching during natural progression and in response to therapy. NKX2-1 loss in human and murine lung adenocarcinoma leads to invasive mucinous adenocarcinoma (IMA), a lung cancer subtype that exhibits gastric differentiation and harbors a distinct spectrum of driver oncogenes. NKX2-1 is required for optimal tumor initiation, but dispensable for growth of established tumors, in $BRAF^{V600E}$ driven disease. NKX2-1-deficient, $BRAF^{V600E}$ driven tumors resemble human IMA and exhibit a distinct response to BRAF/MEK inhibitors. Whereas BRAF/MEK inhibitors drive NKX2-1-positive tumor cells into quiescence, NKX2-1-negative cells fail to exit the cell cycle after the same therapy. BRAF/MEK inhibitors also induce cell identity switching in NKX2-1-negative lung tumors within the gastric lineage, which is driven in part by WNT signaling and FoxA1/2. These data elucidate a complex, reciprocal relationship between lineage specifiers and oncogenic signaling pathways in the regulation of lung adenocarcinoma identity that is likely to impact lineage-specific therapeutic strategies.

32 **INTRODUCTION**

33 Lung adenocarcinoma (LUAD), the most common cause of cancer death worldwide, exhibits
34 significant heterogeneity in tumor cell identity and overall differentiation state (Travis et al., 2011).
35 The state of LUAD differentiation correlates closely with prognosis, intrinsic therapeutic sensitivity,
36 and drug resistance (Campos-Parra et al., 2014; Rotow and Bivona, 2017; Russell et al., 2011).
37 Recent work by our lab and others has shown that the pulmonary lineage specifier NKX2-1/TTF1
38 is a central regulator of LUAD growth and identity (Maeda et al., 2012; Snyder et al., 2013). NKX2-
39 1 is expressed in ~75% of human LUAD, and NKX2-1 negative tumors confer a worse prognosis
40 than NKX2-1-positive tumors (Barletta et al., 2009). The specific role of NKX2-1 in LUAD
41 depends, in part, on the driver oncogene (Maeda et al., 2012; Skoulidis and Heymach, 2019;
42 Snyder et al., 2013). The majority of LUADs harbor mutually exclusive mutations in driver
43 oncogenes that signal through the mitogen activated protein kinase (MAPK) pathway, including
44 *EGFR* (14% of cases), *KRAS* (29%) and *BRAF* (7%) (early stage cases, reviewed in (Skoulidis
45 and Heymach, 2019). In this disease, active forms of the RAS family of small GTPases stimulate
46 the RAF/MEK/ERK kinase cascade to drive proliferation, survival and invasion.

47 Treatment-naïve *EGFR*-mutant LUADs almost always express NKX2-1, and genetically
48 engineered mouse models (GEMMs) suggest that NKX2-1 is required for optimal growth of
49 *EGFR*-mutant LUAD (Maeda et al., 2012). Intriguingly, case reports suggest NKX2-1 expression
50 can be lost when *EGFR*-mutant LUADs acquire drug resistance during a lineage switch to
51 squamous cell carcinoma (Levin et al., 2015). In contrast to *EGFR* mutant LUAD, NKX2-1
52 expression is lost in a subset of *KRAS* and *BRAF* mutant tumors (Skoulidis et al., 2015; Zhang et
53 al., 2015). In a *Kras*^{G12D}-mutant LUAD GEMM, *Nkx2-1* deletion enhances tumor growth and
54 causes pulmonary to gastric transdifferentiation (Snyder et al., 2013), which is driven by the
55 transcription factors FoxA1 and FoxA2 (Camolotto et al., 2018). Stochastic NKX2-1 loss has a
56 similar effect on a distinct *KRas*-mutant LUAD GEMM (Maeda et al., 2012). *Nkx2-1*-deficient
57 murine tumors closely resemble invasive mucinous adenocarcinoma (IMA), a subtype of NKX2-

58 1-negative human LUAD that also expresses gastric markers. Human IMAs often harbor
59 mutations in *KRAS* (62% of cases), occasionally *BRAF* (3%, including point mutations and
60 fusions), but rarely *EGFR* (0.6%) (Cha and Shim, 2017). These studies suggest that there can
61 be selective pressure for LUAD to either retain or downregulate NKX2-1 expression depending
62 on the specific signaling networks activated by a given driver oncogene.

63 MAPK signaling is generally considered to drive proliferation and survival in LUAD, and
64 has become a therapeutic target in some contexts (Ferrara et al., 2020). For example, small
65 molecule inhibitors of BRAF and its downstream kinase MEK have recently shown clinical efficacy
66 in *BRAF*-mutant LUAD (Khunger et al., 2018). However, mechanisms underlying heterogeneous
67 responses remain to be identified. MAPK signaling also regulates differentiation state in a variety
68 of tissues, including the stomach, depending on the magnitude and context of its activity
69 (Mendoza et al., 2011; Osaki and Gama, 2013). We have previously shown that *Nkx2-1* deletion
70 in $KRAS^{G12D}$ driven LUAD leads to IMA with high levels of MAPK activity, as assessed by levels
71 of active (phosphorylated) ERK1/2 (pERK). In contrast, *Nkx2-1* deletion in alveolar type-2
72 pneumocytes causes hyperplasia with low levels of pERK (Snyder et al., 2013). IMA and NKX2-
73 1-negative hyperplasia both express some common pan-gastric markers (e.g., HNF4A),
74 demonstrating that loss of NKX2-1 causes pulmonary to gastric transdifferentiation independent
75 of elevated ERK activity. However, the cells in each lesion have a discrete morphology and form
76 lesions with distinct architectures, suggesting that oncogenic signaling downstream of $KRAS^{G12D}$
77 dictates the specific identity adopted by an NKX2-1-deficient lung cell.

78 We have sought to dissect the role of NKX2-1 in *BRaf*-mutant LUAD using a GEMM of
79 this disease. Here, we show that NKX2-1 regulates cellular identity, oncogenic signaling and
80 response to MAPK pathway inhibition in *BRaf*-mutant adenocarcinoma. Our data show that the
81 level of MAPK pathway activity dictates the specific identity adopted by NKX2-1-negative tumor
82 cells within the gastric lineage. This identity shift is mediated in part by WNT signaling, which is
83 increased after MAPK inhibition in IMA models.

84

85 **RESULTS**

86 *Activation of oncogenic BRAF in the absence of NKX2-1 from the pulmonary alveolar epithelium*
87 *leads to the development of invasive mucinous adenocarcinoma*

88 To dissect the role of NKX2-1 in mutant BRAF-induced lung adenocarcinoma, we utilized
89 two established mouse strains bearing recombinase-activatable alleles of *BRaf*^{V600E}. In the first
90 mouse model, Cre-sensitive conditional alleles of *BRaf* (*CA/*+) (Dankort et al., 2007), *Trp53* (*f/f*)
91 (Jonkers et al., 2001), *Rosa26*$^{LSL\text{-}tdTomato}$ (Madisen et al., 2010), and *Nkx2-1* (*f/*+ or *f/f*) (Kusakabe
92 et al., 2006) were recombined in the mouse lung epithelium upon intratracheal delivery of virus
93 expressing Cre recombinase. Recombination of these alleles simultaneously activates BRAF^{V600E}
94 and tdTomato expression while eliminating p53 and NKX2-1 expression. Mice of the genotype
95 *BRaf*$^{CA/+}$*;Trp53*$^{f/f}$*;Nkx2-1*$^{f/+}$*;Rosa26*$^{LSL\text{-}tdTomato}$ are hereafter referred to as BP mice and mice with
96 the genotype *BRaf*$^{CA/+}$*;Trp53*$^{f/f}$*;Nkx2-1*$^{f/f}$*;Rosa26*$^{LSL\text{-}tdTomato}$ are hereafter referred to as BPN mice.
97 Initial evaluation of histological (H&E) and molecular features revealed mucin production and
98 gastrointestinal differentiation state in *Nkx2-1*-deficient tumors, including expression of HNF4A,
99 PDX1, Gastrokine 1, Cathepsin E, and Galectin-4 (Fig. 1a and Supplementary Figure 1a). In lung
100 tumors, NKX2-1 is required for sustained expression of pulmonary state marker genes such as
101 those encoding the surfactant proteins (*Sftpb* and *Sftpc* (Snyder et al., 2013)) and the cell surface
102 protein CD36 (Camolotto et al., 2018). Accordingly, immunohistochemical analysis showed that
103 mucinous NKX2-1-negative tumors in BPN mice lack expression of pro-surfactant proteins B and
104 C as well as CD36 (Supplementary Figure 1b). Overall, NKX2-1-negative tumors in the *BRaf*^{CA}
105 model bore a close resemblance to those previously seen in the KRAS^{G12D} GEMM and human
106 IMA (Snyder et al., 2013).

107 Despite similar morphologic phenotypes in the BRAF^{V600E} and KRAS^{G12D} models, *Nkx2-1*
108 deletion had a profoundly distinct effect on tumor initiation when combined with either of these
109 oncogenes. Whereas *Nkx2-1* deletion augmented tumor initiation by KRAS^{G12D} (Snyder et al.,

110 2013), it significantly impaired tumor initiation by BRAF^{V600E}. *Nkx2-1* deletion led to a lower tumor
111 burden 8 weeks after initiation (Fig. 1b) and significantly prolonged overall survival (Fig. 1c). We
112 also quantitated tumor grade to better characterize tumor progression in this study and determine
113 the predominant tumor type at the time of euthanasia. For BP tumors, we utilized the grading
114 criteria described in (Winslow et al., 2011). Almost all tumors were grade 1-2 (average ~98% of
115 overall tumor burden), and grade 3 tumors were rare (Fig. 1d). As BPN tumors are morphologically
116 distinct from BP tumors, we needed to develop a grading scheme specifically for the cellular
117 morphologies observed in this genotype. Accordingly, we characterize endpoint BPN tumors as
118 'low grade' if they are essentially identical to BPN tumors at early timepoints: tumor cells contain
119 abundant intracellular mucin, low nuclear to cytoplasmic ratio, and small nuclei with minimal
120 pleomorphism (Fig. 1a). In contrast, we consider BPN tumors to be 'high grade' if they have
121 diminished or absent mucin production, increased nucleus to cytoplasm ratio, and increased
122 nuclear size and pleomorphism (Supplementary Figure 1c). Based on these grading criteria, we
123 found that high grade BPN tumors comprised a much greater proportion of the NKX2-1-negative
124 tumor burden than low grade BPN tumors (~74% vs. 26%) (Fig. 1d). Thus, in this model, loss of
125 NKX2-1 is compatible with tumor progression to a high grade state, despite its impairment of
126 tumor initiation. These data suggest that BP mice succumb primarily to an abundance of low
127 grade tumors. In contrast, the lower initial tumor burden in BPN mice provides more time for
128 tumors to grow and progress to a high grade state before compromising pulmonary function.

129 In the KRAS^{G12D} model, we previously showed that inducing loss of lineage specifiers in
130 established neoplasms can have distinct consequences when compared to lineage specifier loss
131 at the time of tumor initiation (Camolotto et al., 2018). Models that enable gene manipulation in
132 established tumors may be more physiologically relevant to tumor progression than models in
133 which all genetic perturbations are present during tumor initiation. We therefore used a dual
134 recombinase system in the present study to assess the role of NKX2-1 in the established
135 BRAF^{V600E} lung adenocarcinomas. Mice harboring FlpO-recombinase sensitive alleles of *BRaf*

136 (*FA/+*) (Shai et al., 2015), *Trp53* (*frt/frt*) (Lee et al., 2012), and *Rosa26* (*FSF-Cre*^{ERT2}) (Schönhuber
137 et al., 2014) were transduced with FlpO expressing adenovirus to recombine the above Flp-
138 sensitive alleles and establish BRAF^{V600E}-induced lung lesions. After 3 or 6 weeks of tumor
139 growth, *Nkx2-1*$^{f/f}$ alleles underwent Cre-based recombination upon injection of mice with
140 tamoxifen. To generate NKX2-1-positive controls, a cohort of mice with the same genotype were
141 injected with vehicle (corn oil). In contrast to vehicle controls, *Nkx2-1* deletion drove transition of
142 established tumors to invasive mucinous adenocarcinoma (IMA) (Fig. 2a and Supplementary
143 Figure 2a). Collectively, these results and previous work from other labs indicate that *Nkx2-1*
144 deletion promotes a cell lineage switch in LUAD driven by either KRAS^{G12D} or BRAF^{V600E} (Maeda
145 et al., 2012; Snyder et al., 2013).

146 We next evaluated the effect of NKX2-1 loss on the growth of established BRAF^{V600E} -
147 driven tumors. At early timepoints (3 weeks after tamoxifen treatment), *Nkx2-1* deletion had no
148 significant effect on tumor burden (Fig. 2b). In contrast, *Nkx2-1* deletion in established KRAS^{G12D}-
149 expressing cells at the same time point greatly enhanced tumor burden, as described previously
150 (Fig. 2c) (Snyder et al., 2013; Young et al., 2011). At this same timepoint, we also compared
151 proliferation rates using MCM2 positivity in tumors and found that depletion of NKX2-1 did not
152 impact cell proliferation (Supplementary Figure 2b, c). Long term survival analysis revealed no
153 significant difference between tumor-bearing mice treated with tamoxifen and controls (Fig. 2d).
154 Histopathologic analysis of the survival study revealed that control mice harbored predominantly
155 non-mucinous NKX2-1-positive tumors, whereas tamoxifen-treated mice harbored predominantly
156 NKX2-1-deficient tumors, many of which were high grade, further supporting the notion that
157 NKX2-1 loss is permissive for malignant progression in BRAF-driven lung neoplasia (images and
158 quantitation in Supplementary Figure 2d, e). These data show that loss of NKX2-1 in established
159 BRAF^{V600E} lung adenocarcinoma is tolerated but does not augment tumor growth, in contrast to
160 NKX2-1 loss KRAS^{G12D}-driven tumors. This likely explains why *KRAS* mutations are enriched in

161 IMA (relative to LUAD overall), whereas *BRAF* mutations are diminished in frequency, but not
162 excluded altogether like *EGFR* mutations.
163
164 *Loss of NKX2-1 stimulates MAPK signaling downstream of mutant BRAF*
165 We have previously shown that *Nkx2-1* deletion augments ERK activity in $KRAS^{G12D}$-
166 driven lung adenocarcinoma (Snyder et al., 2013), and feedback inhibition of the MAPK pathway
167 is known to be rate-limiting for the growth of $KRAS^{G12D}$-driven tumors in vivo (Shaw et al., 2007).
168 We therefore asked whether the *Nkx2-1* deletion also alters MAPK activity in $BRAF^{V600E}$-driven
169 lung tumors. We initially hypothesized that pERK levels would be similar in BP and BPN tumors,
170 thus explaining the fact that *Nkx2-1* deletion does not augment $BRAF^{V600E}$-driven lung
171 tumorigenesis. Surprisingly, *Nkx2-1* deletion in both the concomitant and sequential tumor models
172 led to increased MAPK signaling downstream of oncogenic BRAF as assessed by IHC. Whereas
173 NKX2-1-positive (BP) tumors generally exhibited weak, patchy staining for phosphorylated ERK1
174 and ERK2 (pERK), we observed strong pERK staining in NKX2-1-negative (BPN) tumors (Fig. 3a
175 and Supplementary Figure 3a). In contrast, phosphorylated levels of MEK1/2 were similar in BP
176 and BPN tumors, suggesting that activation of ERK1/2 in BPN tumors is largely due to regulation
177 downstream of MEK1/2 activity (Fig. 3a). Moreover, in BPN tumors, we found increased
178 phosphorylation of p90RSK (a direct target of active ERK) and 4E-BP1 and S6 proteins -
179 downstream targets of mTORC1, through which mTORC1 stimulates protein synthesis and cell
180 growth (Carriere et al., 2011; Mendoza et al., 2011; Roux et al., 2007) (Fig. 3a, b and
181 Supplementary Figure 3b). We confirmed differences in degree of pathway activation between
182 BP and BPN tumors by IHC quantitation (Fig. 3c, and Supplementary Figure 3b). Therefore, BPN
183 tumors exhibit hyperactivation of both MAPK and mTORC1 oncogenic pathways. Importantly,
184 several of these distinguishing features observed in vivo, such as the association between low
185 NKX2-1 and high pERK levels are conserved in vitro in primary tumor spheroid cultures from
186 autochthonous BP and BPN tumors (Supplementary Figure 3c).

187 Finally, we performed IHC for pERK on a panel of mucinous (n=17, see Methods for
188 inclusion criteria) and NKX2-1-positive primary human lung adenocarcinomas (n=51). Strong
189 pERK staining was detectable in the majority of mucinous tumors (14/17). Among positive cases,
190 seven tumors exhibited diffuse staining (>90% of tumor cells positive), and another seven
191 exhibited partial positivity (20-90% of tumor cells positive). In contrast, NKX2-1-positive LUAD
192 showed a trend toward lower pERK staining than the mucinous adenocarcinomas. Only 20% of
193 NKX2-1-positive tumors were diffusely positive (vs. 41% of mucinous tumors), and 35% of NKX2-
194 1-positive tumors were negative for pERK (vs. 18% of mucinous tumors). Quantitation and
195 representative pictures are shown in Fig. 3d and Supplementary Figure 3d. The ERK
196 phosphorylation site is more labile than epitopes recognized by antibodies that detect total protein
197 levels. Therefore, staining patterns likely reflect both biologic heterogeneity and variable
198 processing of clinical specimens. Nevertheless, these data show that the high levels of pERK in
199 IMA mouse models can be observed in many cases of human IMA.
200
201 *Response of NKX2-1-positive and NKX2-1-negative tumors to RAF/MEK inhibition*
202 The increase in MAPK activity we observed in both in vivo and in vitro models led us to
203 ask whether NKX2-1 status influenced response to MAPK pathway inhibition. To investigate this,
204 we directly compared the effect of RAF/MEK inhibitors on the growth and proliferation of
205 autochthonous BP and BPN lung tumors. We chose dual inhibition of MEK and BRAF because
206 this combination is the standard of care for $BRAF^{V600E}$-mutant human lung adenocarcinoma
207 (Planchard et al., 2016) and because in other genetically engineered mouse models driven by
208 $BRAF^{V600E}$ e.g., thyroid cancer (McFadden et al., 2014), the combination of the two inhibitors is
209 more effective than either one alone at inhibiting the MAPK pathway in vivo. We found that
210 administration of $BRAF^{V600E}$ inhibitor (PLX4720) in combination with MEK inhibitor (PD0325901)
211 effectively suppressed ERK phosphorylation in lung tumors of both genotypes (Fig. 4a).
212 Combined BRAF/MEK inhibition led to a dramatically lower tumor burden in both BP and BPN

213 mice when assessed after two weeks (Fig. 4b) and four weeks (Fig. 4c) of drug treatment. The
214 decrease in tumor burden in BPN mice was greater by two-fold compared to that in BP mice,
215 suggesting that BPN tumors were overall more sensitive to MAPK inhibition. In fact, we noted that
216 residual MAPK-inhibited BPN tumors resembled hyperplasia induced by *Nkx2-1* deletion alone
217 with respect to both morphology and low pERK levels (Fig. 4a). NKX2-1-positive, $BRAF^{V600E}$-
218 driven lung tumors have been shown to regress when treated with MEK inhibitor, but regrow
219 rapidly after drug cessation (Trejo et al., 2012). We therefore asked whether drug-treated residual
220 BP and BPN cells retain tumorigenic potential. Histopathologic analysis of BP and BPN tumors
221 treated for four weeks with BRAF/MEK inhibitor followed by drug removal showed that the residual
222 cells readily grew back over the course of 1-4 weeks (Supplementary Figure 4a).

223 To gain insights into the mechanisms of drug response in each model, we performed
224 transcriptome profiling by bulk and single cell RNA sequencing. Using the Cre-activated *tdTomato*
225 reporter (Madisen et al. 2010) in the $BRaf^{CA}$ model, we enriched tdTomato-positive tumor cells
226 via fluorescence activated cell sorting (FACS). Tumor cells were isolated from mice of both
227 genotypes (BP and BPN) that had been placed on BRAF/MEK inhibitor-diet or control chow for
228 one week.

229 We first performed Principal Component Analysis (PCA) on bulk RNA sequencing data
230 using the top 500 most variable genes. This analysis revealed that replicate samples cluster
231 together but that the four groups (control and drug treated BP and BPN tumors) could be
232 distinguished from each other at the transcriptomic level. As represented in Fig. 4d, the greatest
233 source of transcriptome diversity was related to deletion of *Nkx2-1* and is reflected by PC1. PC2
234 was related to MAPK inhibition-imposed transcriptomic changes, which appeared to more strongly
235 distinguish BPN tumors than BP tumors. Regardless of treatment, BP tumors expressed higher
236 levels of pulmonary genes (e.g. *Sftpb* and *Sftpc,* Supplementary Figure 4b and Supplementary
237 Table 1) and BPN tumors expressed higher levels of gastric genes (e.g., *Pdx1* as well as a
238 significant subset of HNF4A-target genes as revealed by the Illumina Correlation Engine

239 (Supplementary Figure 4c and Supplementary Table 1)). Furthermore, *Dusp6*, a transcriptional
240 readout of active ERK, was significantly downregulated in MAPK-inhibitor treated BP and BPN
241 tumors compared to their respective controls (Supplementary Figure 4d and Supplementary Table
242 2).

243 Despite these differences, NKX2-1 targets (e.g. *Sftpc)* were detected at higher levels than
244 expected in sorted BPN tumor cells. We had previously observed that a minority of tumors in BPN
245 mice were non-mucinous and retain NKX2-1 expression by IHC. We therefore inferred that a
246 subset of these tumor cells may retain NKX2-1 due to incomplete recombination (Figure 1 and
247 data not shown). Since the presence of incomplete recombinants could compromise our ability to
248 accurately analyze the transcriptional consequences of NKX2-1 deficiency, we performed
249 additional single cell RNAseq analysis of FACS-sorted BPN tumors (following one week of drug
250 or vehicle treatment) using the 10X Genomics platform. We predicted that this would enable us
251 to circumvent the technical difficulty of resolving complete from incomplete recombinants and also
252 investigate therapy response at the single cell level.

253 We characterized the transcriptome of 5,065 control and 5,563 drug-treated single BPN
254 cells (Supplementary Figure 4e). In our initial analysis, rare non-tumor cells clustered separately
255 from tumor cells, and their identity was further validated by the expression of well-known stromal
256 markers including *Vim*, *Ptprc*, *Trpm5*, *Pecam1*, *Mgp*, *Cd79a*, *Itgam*, *Adgre1*, *Cd3g*, and *Marco*.
257 Filtering against contaminating stromal, endothelial, hematopoietic and low-quality cells reduced
258 the dataset to a total of 6,807 high quality tumor cells for further analysis (Supplementary Figure
259 4e). We visualized these cells in reduced dimensionality using UMAPs and identified eight major
260 tumor clusters (Fig. 4e and Supplementary Table 3). The majority of these cells (70%) fell into
261 three NKX2-1-low clusters (1-3) and expressed multiple gastric markers (Fig. 4f and
262 Supplementary Table 3, 4). Examination of bam files confirmed that the rare *Nkx2-1* transcript
263 counts in Clusters 1-3 correspond to residual flanking sequences from complete recombinants at
264 the *Nkx2-1* locus and did not contain reads mapping to splice junctions of Cre-deleted exons in

265 the *Nkx2-1* gene (Supplemental Figure 4f). Cluster 3 exhibited high expression of *AurkB*, *Plk1*,
266 and other genes that suggest that these cells are in G2/M phase (Fig. 4f and see Fig. 5 for more
267 detail). Cluster 1 and cluster 2 overwhelmingly contain cells from control and drug-treated mice,
268 respectively.

269 In contrast, the remaining cells (30%) exhibited frequent and abundant *Nkx2-1*
270 expression, including splicing from Cre-target exons indicating a failure to recombine (Fig. 4f and
271 Supplemental Figure 4f). These cells also frequently expressed the NKX2-1 target *Sftpc* (Fig. 4f).
272 We interpret these cells, which fall into clusters 4-8, to be the incomplete recombinants that we
273 have directly observed microscopically and inferred from bulk RNAseq data. The variable levels
274 of *Nkx2-1* and *Sftpc* in clusters 4-8 (Fig. 4f) suggests that some of these cells represent higher
275 grade tumor cells that stochastically lose NKX2-1 activity and expression, as has been
276 documented in $KRAS^{G12D}$-driven GEMMs (Snyder et al., 2013; Winslow et al., 2011). For example,
277 we noted that cluster 5 cells express high levels of the embryonic marker *Hmga2*, a previously
278 characterized marker of high grade tumor cells (Supplementary Figure 4g). Similar to cluster 3,
279 cluster 8 exhibited high expression of *AurkB*, *Plk1*, and other genes that suggest that these NKX2-
280 1-positive tumor cells are in G2/M phase. In contrast to cluster 3, we note that cluster 8 is
281 comprised almost exclusively of untreated cells, consistent with cell cycle exit of treated cells that
282 retain NKX2-1 (Fig. 4e, f and see Fig. 5 for further analysis). We quantified differences in MAPK
283 pathway activation between BP and BPN tumors in our single cell sequencing data by applying
284 the MEK activity transcriptional signature published in (Dry et al., 2010). This analysis
285 substantiates our conclusions that BPN tumors display higher MAPK signaling than BP tumors
286 (Supplementary Figure 4h). Furthermore, using the Dry et al. signature, we find that RAF/MEK
287 inhibition reduces pathway output in both genotypes (Supplementary Figure 4h).

288

289 *NKX2-1 status influences cell cycle response to RAF/MEK inhibition*

290 The MAPK pathway regulates proliferation by multiple mechanisms, including activating
291 expression of the D-type cyclins, which can drive cells out of quiescence and into the cell division
292 cycle (Lavoie et al., 1996; Tuveson et al., 2004). We therefore evaluated the impact of drug
293 treatment on cell cycle status of BP and BPN lung tumors using IHC for cell cycle markers as well
294 as analysis of RNAseq datasets. We first evaluated drug response by IHC for MCM2, a helicase
295 detectable throughout the cell cycle but not in quiescence (G0). In BP tumors, two weeks of drug
296 treatment led to a significant decline in the percentage of MCM2-positive cells (Fig. 5a and b).
297 Additional IHC analysis showed a decline in the percentage of BP cells positive for BrdU
298 incorporation and phospho-histone H3 (pHH3, M phase marker) (Supplementary Figure 5a-c).
299 Taken together, these data show that drug treatment of BP tumors blocks proliferation and
300 induces cell cycle exit, thereby increasing the proportion of cells in quiescence.

301 In contrast to BP tumors, drug treatment of BPN tumors led to a paradoxical increase in
302 the percentage of MCM2-positive cells (Fig. 5a and b) despite decreased tumor burden (Fig. 4b).
303 In contrast, the percentage of BPN cells positive for BrdU and pHH3 declined to the same extent
304 as BP cells after drug treatment (Supplementary Figure 5a-c). These data suggest that even
305 though BPN cell proliferation is impaired by drug treatment, most residual BPN cells fail to exit
306 the cell cycle and enter quiescence in the absence of MAPK activity.

307 Analysis of bulk RNA sequencing further demonstrated that BP and BPN tumor cells
308 exhibit a differential cell cycle response to MAPK inhibition. Drug-induced transcriptomic changes
309 were highly distinct between genotypes. Pathway analysis (via Illumina Correlation Engine)
310 demonstrated key differences between BP and BPN drug treated lung tumors in the most
311 significant Gene ontology (GO) terms. Specifically, multiple cell cycle-related pathways decline in
312 treated BP tumors, but not in treated BPN tumors, relative to their respective untreated controls
313 (Fig. 5c and Supplementary Table 5, 6). Instead, the top GO pathway terms in treated BPN tumors
314 relative to vehicle controls included pathways related extracellular reorganization and cell motility
315 (Fig. 5d and Supplementary Table 6).

316 We calculated cell cycle scores of control and treated tumor cells in scRNA-seq data using
317 the Seurat package and phased cell cycle gene signatures previously defined in mouse cells
318 (Mizuno et al., 2009). The results of this analysis are consistent with the general conclusion that
319 BP and BPN cells have distinct cell cycle responses to RAF/MEK inhibition (Fig. 5e). However,
320 the Seurat cell cycle score approach is not well adapted to distinguish G0 from G1 phase cells.
321 We therefore developed a novel methodology for analyzing quiescence in scRNA-seq data using
322 diffusion mapping (Haghverdi et al., 2015) and the complete set of fine-scale cell cycle phase
323 signatures from (Mizuno et al., 2009), which includes both quiescent and cycling cells
324 (Supplementary Figure 5d). Using this novel approach, cells with high expression of S-phase or
325 G2/M-phase signatures mapped to successive extremes at the right of the cyclic graph (Fig. 5f),
326 while the majority of cells (>80%) mapped to the left-hand portion corresponding to G0 and G1
327 signature enrichments (Fig. 5f). Remarkably, these scRNA-seq analyses also revealed NKX2-1
328 dependent effects of drug treatment on cell cycle status. Treatment of BP cells caused a marked
329 redistribution toward the left hand extreme of the graph, which is most distal from cycling cells
330 and is enriched for the G0 signature, while the distribution of BPN cells was minimally affected by
331 treatment (Fig. 5g).

332 Given the ability of the MAPK pathway to drive cell cycle entry by activation of D-type
333 cyclin expression, we evaluated the expression patterns of *Ccnd1-3* in bulk and single cell RNA
334 sequencing data. Suppression of MAPK activity led to decreased *Ccnd1* transcript and protein
335 levels in both BP and BPN tumors (Fig. 5h, Supplementary Figure 5e, f) suggesting that the MAPK
336 pathway is a major activator of *Ccnd1* expression in tumors of both genotypes. In contrast, *Ccnd2*
337 mRNA levels were significantly higher in BPN tumors than BP tumors, and drug treatment of BPN
338 tumors led to a further increase in *Ccnd2* levels (Fig. 5h, Supplementary Figure 5e). At the protein
339 level, we have only been able to detect Cyclin D2 by IHC in treated BPN tumors (Supplementary
340 Figure 5g). *Ccnd3* levels were low and relatively stable across all four conditions (Supplemental
341 Table 1 and 4).

342 These data raise the possibility that increased Cyclin D2 levels in treated BPN tumors
343 might maintain CDK4/6 activity, thereby preventing cells from entering quiescence despite their
344 MAPK-low state. To test this idea further, we used IHC to evaluate RB phosphorylation at
345 S807/S811, two sites that can be phosphorylated by CDK4/6 (Fig. 5i). Two weeks of MAPK
346 inhibition significantly decreased the percent of phospho-RB positive cells in BP tumors (Fig. 5i).
347 In contrast, there was no change in phospho-RB S807/S811 levels in treated BPN tumors.
348 To evaluate specifically the potential role of Cyclin D2 in the cell cycle response to MAPK
349 inhibitors, we knocked down Cyclin D2 in BPN organoids using two different shRNAs
350 (Supplementary Figure 5h). We then transplanted these lines into NSG mice subcutaneously,
351 allowed tumors to form and grow for eight weeks, and treated mice with RAF/MEK inhibitor for
352 four weeks. Histopathologic analysis revealed that organoid-derived tumors exhibited a triphasic
353 morphology in vivo, including large cystic structures, glandular adenocarcinoma, and small foci of
354 poorly differentiated adenocarcinoma. Cystic structures appeared to accumulate fluid at a
355 variable rate, precluding the use of tumor size as a metric of drug response. We quantitated
356 MCM2 levels in the glandular adenocarcinomas, the component with the greatest similarity to the
357 autochthonous model. We found that MAPK inhibition failed to reduce the MCM2 rate in control
358 adenocarcinomas, whereas the MCM2 rate declined in tumors with Cyclin D2 knockdown upon
359 drug treatment (Fig. 5j). Although organoid-derived subcutaneous tumors do not perfectly mimic
360 the autochthonous BPN model, these data provide additional orthogonal evidence that Cyclin D2
361 plays a role in the response of NKX2-1-negative lung adenocarcinoma to MAPK inhibition.
362 Taken together, these data show that NKX2-1 status has a profound effect on the cell
363 cycle response of $BRAF^{V600E}$-driven lung tumors to targeted therapy. We propose that Cyclin D2
364 helps maintain CDK4/6 activity and RB phosphorylation in treated BPN tumors, thus preventing
365 cell cycle exit. The inability of residual BPN cells to exit the cell cycle suggests that distinct
366 therapeutic strategies may be needed to eliminate BP versus BPN tumor cells after MAPK
367 inhibition.

368 *MAPK pathway regulates identity of NKX2-1-negative mucinous adenocarcinoma within the*
369 *gastric lineage*

370 Further analysis of gene expression changes in BPN tumors revealed surprising switch-
371 like changes in the expression of lineage markers associated with specific gastric cell types. BPN
372 tumor cells normally express high levels of transcripts that mark surface mucous cells in the
373 stomach, such as *Muc5ac* and *Gkn1*. We find these surface mucous cell markers decline
374 significantly upon MAPK pathway inhibition (Fig. 6a). In parallel, two of the most highly
375 upregulated genes in drug-treated BPN tumor cells were *Pgc* and *Cym* (Fig. 6a and
376 Supplementary Figure 4d), which encode digestive enzymes normally expressed in chief cells
377 found at the base of the stomach gland (Han et al., 2019; Leushacke et al., 2017; McCracken et
378 al., 2017). Additional markers of murine gastric chief cells including *Pga5* and *Clps* were also
379 induced by drug treatment in these tumors (Fig. 6a). *Cym* is expressed predominantly during the
380 neonatal phase of mouse stomach development (Chen et al., 2001; Vallone et al., 2016),
381 suggesting that these treated tumor cells may adopt an immature chief cell-like phenotype. Drug-
382 treated NKX2-1-negative tumor cells also exhibited induction of several markers of chemosensory
383 tuft cells, including the lineage specifier *Pou2f3* (Kaji and Kaunitz, 2017) as well as *Gfi1b* and
384 *Gnat3* (Fig. 6a). We next utilized gene set enrichment analysis (GSEA) to compare the
385 transcriptome of drug treated BPN tumors to published/curated gene expression datasets for
386 gastric epithelial cell types and tuft cells (Haber et al., 2017; Leushacke et al., 2017; Montoro et
387 al., 2018; Ting and von Moltke, 2019; Zhang et al., 2019) (Supplementary Table 7 and 8). GSEA
388 showed that signatures of both *Lgr5*-expressing gastric chief cells as well as tuft cells were
389 significantly enriched in MAPK-inhibited BPN cells (Fig. 6b).

390 A shift in expression of gastric lineage markers was also evident at the single cell level.
391 Our single cell transcriptomics confirmed that gastric surface mucous markers like *Gkn1* and *Tff1*
392 are downregulated by drug treatment in NKX2-1-negative cells (Fig. 6c), whereas chief markers
393 were induced. Many treated BPN cells have higher levels of chief markers (*Cym, Pgc, Pga5*) than

394 the control BPN cells. This suggests true induction of transcription rather than simple selection
395 for a pre-existing population of chief-high cells (Fig. 6c). In contrast, MAPK inhibition appears to
396 increase the fraction of cells positive for the tuft cell marker *Pou2f3*, rather than the absolute levels
397 of transcript per cell (though expression of this marker is low and somewhat sporadically detected
398 in our single cell RNAseq data) (Fig. 6c). *Tff2* transcripts, which mark progenitors located in the
399 isthmus of the normal stomach (Quante et al., 2010), were also increased in drug-treated BPN
400 cells (Fig. 6c).

401 Given this apparent lineage switch, we used IHC to evaluate a subset of lineage markers
402 at the protein level in vivo. GKN1 protein (surface mucous marker) was abundant in control BPN
403 tumors, but was depleted in inhibitor-treated BPN tumors (Supplementary Figure 6a). Control
404 BPN tumors were entirely negative for Pepsinogen C, whereas a subset of treated BPN cells were
405 Pepsinogen C-positive (Fig. 6d, upper row). In contrast, a small subset of control BPN tumor cells
406 were POU2F3 positive, and the fraction of positive cells was higher in treated BPN tumors (Fig.
407 6d, lower row). These data are concordant with our single cell analysis of these two markers in
408 terms of changes in proportion of positive cells vs. induction of absolute levels on a per-cell basis.
409 Both Pepsinogen C and POU2F3-positive cells were found in alveolar hyperplasia induced by
410 *Nkx2-1* deletion, consistent with the microscopic similarity between these hyperplasia and
411 residual treated BPN tumor cells. As expected, all three gastric lineage markers evaluated (GKN1,
412 Pepsinogen C and POU2F3) were undetectable in BP tumors.

413 We also examined POU2F3 by IHC in a panel of primary human LUAD tissues
414 (Supplementary Figure 6b). We found that almost all IMA tumors (15/16) harbor a minority
415 population of POU2F3-positive cells (Supplementary Figure 6b). Like in BPN tumors, these
416 POU2F3-positive cells were relatively rare (~5% or less of tumor cells overall). In contrast, most
417 NKX2-1-positive human lung adenocarcinomas were entirely POU2F3-negative (44/51)
418 (Supplementary Figure 6b, c). Interestingly, we detected a minor population of POU2F3-positive
419 tumor cells in seven NKX2-1-positive cases (Supplementary Figure 6b). This expands upon other

420 recent observations that POU2F3 can be upregulated in specific subtypes of lung cancer (Huang
421 et al., 2018). Thus, a rare population of POU2F3-positive tumors cells is readily detectable in both
422 human IMA and murine models.

423 We next asked whether regulation of gastric lineage by the MAPK pathway is a general
424 feature of IMA, or limited to $BRAF^{V600E}$-driven tumors. To address this question, we generated
425 organoids from autochthonous IMA models driven by $KRAS^{G12D}$ (KPN) or $BRAF^{V600E}$ (BPN). IHC
426 for the tdTomato reporter on sections of primary organoid cultures (Supplementary Figure 6d)
427 showed that all cultures examined are ~90-100% positive for tdTomato. Rare tdTomato-negative
428 organoids have an exclusively epithelial morphology, and thus are unlikely to represent stromal
429 cell contamination in these cultures. We treated BPN and KPN organoids with a MEK inhibitor
430 (Cobimetinib) for 3 days and found that this was sufficient to stimulate the expression of chief
431 (*Cym*, *Gif*, *Pgc*) and tuft (*Pou2f3* and *Gfi1b*) cell markers in both KPN and BPN organoid cultures
432 (Supplementary Figure 6e and f). Furthermore, induction of chief cell markers in BPN organoids
433 occurred rapidly following MEK inhibition (2hrs for *Cym* and 6hrs for *Pgc*), before any change in
434 cell number occurred (Fig. 6e). Thus, the kinetics of *Cym* induction in vitro are more consistent
435 with a true lineage switch rather than selection for a pre-existing *Cym*-high cells, and are also
436 consistent with our interpretation of single cell data from tumors in vivo. Finally, we treated BPN
437 organoids with additional drugs that target MAPK signaling including the ERK-inhibitor GDC-0994,
438 MEK inhibitor PD0325901, and the BRAF inhibitor PLX4720, all of which induce *Cym*
439 (Supplementary Figure 6g). In aggregate, our data show that drug-induced tumor phenotypic
440 changes are not dependent on the non-specific effects of any one inhibitor. Thus, the MAPK
441 pathway modulates gastric lineage in IMA cells driven by distinct oncogenes (KRAS and BRAF)
442 and in distinct settings (i.e. in vivo and in vitro).

443

444 *MAPK inhibition leads to an increase in canonical WNT activity in NKX2-1 negative lung*
445 *adenocarcinoma*

446 LGR5 marks a subset of normal murine chief cells that can function as facultative stem
447 cells (Leushacke et al., 2017). *Lgr5* is also a canonical WNT target gene, and WNT signaling is
448 thought to promote the regenerative capacity of LGR5-positive chief cells. Given that drug
449 treatment led to an enrichment for the signature of LGR5-positive chief cells in BPN mice, we
450 evaluated our gene expression data to determine whether this was indicative of a general
451 increase in WNT signaling.

452 We examined a set of WNT pathway genes derived from the 'WNT signaling' ontology
453 category on AmiGO (Carbon et al., 2008) in our bulk RNA sequencing of BP and BPN tumors.
454 Several of these genes have previously been identified as direct transcriptional targets of
455 canonical WNT signaling, including *Axin2*, *Lgr5*, *Wnt11*, *Fzd*, *Fgf9*, *Notum*, *Sox9*, *Lrp1*, *Sox4*,
456 *Znrf3*, *Wnt3A* ('positive regulation of canonical WNT signaling' category on AmiGO, (Carbon et
457 al., 2008) and were significantly activated in treated BPN tumors (Fig. 7a). Indeed, applying
458 Ingenuity Pathway Analysis (IPA) Upstream Regulator detection to bulk RNAseq data identified
459 β-catenin as the second top upstream regulator underlying the gene expression changes between
460 control and drug treated BPN tumors (Supplementary Figure 7a). The activation z-score suggests
461 an activated state of β-catenin in treated BPN tumors and a more inhibited state in control BPN
462 tumors. Consistent with this, Regulatory Motif analysis in Illumina Correlation Engine uncovered
463 significant differences in TCF1 binding site genesets between control and treated BPN tumors
464 (Supplementary Figure 7b). WNT targets such as *Axin2* (Jho et al., 2002) and *Lgr5* (Barker et al.,
465 2007) were also induced in our single cell analysis (Supplementary Figure 7c). Although their raw
466 values are at the detection limit in our scRNA-seq data, imputation analysis to recover false
467 negatives further supports a robust increase in *Axin2* and *Lgr5* levels after drug treatment
468 (Supplementary Figure 7d).

469 Intriguingly, the pattern of induction was distinct for these two WNT target genes
470 (Supplementary Figure 7c, d). Cells with the highest levels of *Lgr5* are found only in treated BPN

471 tumors, a pattern consistent with our observations of chief cell markers (Fig. 6c). In contrast, we
472 identified cells with high levels of *Axin2* in both control and treated BPN groups, despite the fact
473 that overall *Axin2* levels are higher in treated BPN. This raises the question of whether WNT-high
474 cells pre-exist in control BPN tumors, or whether MAPK inhibition leads to induction of WNT target
475 genes in WNT-low cells. We therefore developed a WNT13 transcriptional signature (see
476 Methods for derivation) that integrates the WNT target genes induced by MAPK inhibitors in BPN
477 tumors. Scoring of cells in scRNA-seq using this WNT13 signature showed a pattern more similar
478 to *Axin2* than *Lgr5* (Fig. 7b). Taken together, these data suggest that WNT-high cells can be
479 detected in control BPN tumors, at least as defined by a WNT13 signature or *Axin2* levels.
480 However, *Lgr5*-high cells are not detectable pre-treatment, showing that even WNT-high cells
481 lack high level expression of certain target genes. This further supports our observations from
482 analysis of gastric lineage markers that MAPK inhibition modulates the transcriptional cell state
483 of BPN tumor cells (including WNT target genes), and does not purely select for pre-existing
484 populations.

485 To further investigate this question, we performed in vitro time course experiments, which
486 showed that MEK inhibition induces *Lgr5* and *Axin2* within 4 hours of treatment before changes
487 in cell number or viability take place (Fig. 7c, 6e). In a different approach to study the emergence
488 of WNT-high cells, we stably transduced a BPN organoid line with a WNT-reporter construct,
489 7TGP, that contains seven TCF binding sites driving eGFP expression (Fig. 7d, e). When cultured
490 in standard WNT-pathway activating 50% L-WRN media, we found that these cells consisted of
491 a mixture of high and low reporting cells (WNT_{rep}-high and WNT_{rep}-low cells respectively). In
492 contrast, most cells were WNT_{rep}-low when cultured in 5% L-WRN media. We then sorted the
493 WNT_{rep}-low subpopulation from standard culture conditions (50% L-WRN media) and found that
494 these cells re-equilibrated to a mix of WNT_{rep}-high and WNT_{rep}-low cells when cultured in 50% L-
495 WRN media (Fig. 7e). Furthermore, culture of the sorted cells in 5% L-WRN media reduced the
496 WNT_{rep}-high percentage, whereas MEK inhibitor increased the WNT_{rep}-high percentage. Taken

497 together, these experiments indicate that WNT signaling can be induced in WNT_{rep}-low cells with
498 rapid kinetics (i.e., prior to a change in cell viability or selection). Although we cannot exclude the
499 possibility that WNT_{rep}-high cells tolerate MEK inhibition to a greater extent than WNT_{rep}-low cells,
500 these data argue that pure selection for a WNT_{rep}-high subpopulation (in the absence of changes
501 in gene expression on a per cell basis) is unlikely to account for our observations on the overall
502 state change of tumors.

503 Previous studies in other cancer types have documented negative feedback loops
504 between the MAPK and WNT signaling pathways. Mechanistically, these have been reported to
505 be mediated by changes in AXIN1 (Zhan et al., 2019), TCF4 isoform levels (Heuberger et al.,
506 2014) or phosphorylation of FAK (Chen et al., 2018) after MAPK inhibition. However, we have not
507 been able to detect consistent changes in any of these parameters after treatment of our
508 organoids with MEK inhibitors (Supplementary Figure 7e).

509

510 *WNT signaling and FoxA1/2 contribute to lineage switching and cell cycle response in NKX2-1-*
511 *negative lung adenocarcinoma treated with RAF/MEK inhibitor*

512 WNT/β-catenin signaling plays an essential role in gastric epithelial patterning during
513 embryogenesis and promotes chief cell differentiation (McCracken et al., 2017). We therefore
514 asked whether the WNT pathway played a role in the lineage switch induced by MAPK inhibition
515 in IMA. We used two different approaches to modulate WNT signaling in organoid cultures. First,
516 we cultured organoids in 5% conditioned media (L-WRN), corresponding to a 10 fold reduction in
517 the amount of exogenous WNT3A and R-spondin 3 in the culture media relative to standard, 50%
518 L-WRN, conditions. Second, we used the small molecule LGK-974, which blocks Porcupine-
519 mediated posttranslational modification of WNT ligands that is required for their secretion and
520 paracrine signaling. Levels of *Axin2* and *Lgr5* were lower in organoids cultured in 5% L-WRN than
521 50% L-WRN, and treatment with LGK-974 led to a further reduction in these transcripts
522 suggesting endogenous WNT ligand production and signaling complements L-WRN media in

523 these cultures (Supplementary Figure 8a). Consistent with prior analyses (Fig. 7c), MEK inhibitor
524 stimulated canonical WNT signaling in BPN and KPN organoids as indicated by increased
525 expression of the *Axin2* and *Lgr5* transcripts within the first 24 hours (Supplementary Figure 8a).
526 The relative effect of this stimulation (i.e. fold induction) was similar whether the organoid media
527 composition contained high or low levels of exogenous WNT3A. Induction of chief markers (*Cym*,
528 *Pgc*, *Gif*) by Cobimetinib was partially impaired when WNT signaling was reduced by using 5%
529 L-WRN media alone or in combination with LGK-974 (Fig. 8a). Levels of some chief markers (e.g.
530 *Cym*) were responsive to WNT signaling levels even in the absence of MEK inhibitor. In contrast,
531 tuft cell markers (*Pou2f3* and *Gfi1b*) were largely unaffected by modulation of WNT signaling.
532 These data show that one component of lineage switching (induction of chief cell markers) is
533 partially WNT-dependent, whereas another component (tuft cell marker induction) is largely WNT-
534 independent.

535 Previously, our lab reported that FoxA1 and FoxA2 are required for gastric differentiation
536 in mouse models of IMA, including surface mucous cell marker expression (Camolotto et al.,
537 2018). Here, using a novel NKX2-1-negative organoid line that harbors conditional alleles of
538 *Foxa1* and *Foxa2*, we show that *Foxa1/2* deletion abrogates the induction of chief cell markers
539 (but not tuft cell markers) upon MEK inhibition (Fig. 8b, Supplementary Figure 8b). Thus, the
540 surface to chief gastric lineage switch is driven by both WNT signaling and FoxA1/2 activity.

541 Finally, we asked whether WNT signaling might play a role in failure of BPN tumors to exit
542 the cell cycle after RAF/MEK inhibition. WNT signaling contributes to oncogenesis in a variety of
543 settings (Zhan et al., 2017), including in NKX2-1-positive LUAD GEMMs driven by $BRAF^{V600E}$
544 (Juan et al., 2014) or $KRAS^{G12D}$ (Tammela et al., 2017). Further, β-catenin activation upon *Apc*
545 deletion in the murine intestinal epithelium specifically upregulates cyclin D2 to augment
546 proliferation and tumorigenesis (Cole et al., 2010). This raises the possibility that activation of the
547 WNT pathway might be sufficient to induce *Ccnd2* in treated BPN tumors and thereby prevent
548 cell cycle exit, despite the lack of MAPK activity.

549 To investigate this possibility, we first correlated known signatures of MEK (Dry et al.,
550 2010) and WNT activity ('positive regulation of canonical WNT signaling' category on AmiGO,
551 (Carbon et al., 2008)) with levels of *Ccnd1* and *Ccnd2* in our single cell data. MEK activity was
552 positively correlated to *Ccnd1* levels across the single cell data set. Conversely, *Ccnd2* levels
553 were inversely correlated to the MEK signature score and positively correlated to the signature
554 for WNT activity (Supplemental Figure 8c). This suggests that *Ccnd1* levels may be primarily
555 dependent on MAPK activity, whereas *Ccnd2* levels may be more directly dependent on WNT
556 activity in this specific context.

557 Given the relationship between WNT activity and *Ccnd2* levels, we asked whether
558 pharmacological WNT inhibition would be sufficient to drive RAF/MEK-inhibited BPN cells into
559 quiescence. To address this question, we initiated lung tumors in a cohort of BPN mice and
560 assigned mice to four groups at six weeks after initiation (vehicle; MAPKi; LGK-974; or MAPKi +
561 LGK-974). MAPK inhibitor was administered for four weeks (i.e., 6-10 weeks after tumor initiation)
562 and LGK-974 was administered for the last two weeks of MAPKi treatment (i.e., 8-10 weeks after
563 tumor initiation). Four weeks of treatment with RAF/MEK inhibitor led to a significant increase in
564 the percentage of MCM2 positive cells (Fig. 8c), consistent with the effects we observed after 1-
565 2 weeks of treatment. In contrast, treatment with LGK-974 alone had no effect on MCM2 in BPN
566 tumors. Strikingly, additional treatment with LGK-974 was sufficient to block the induction of
567 MCM2 by RAF/MEK inhibition in BPN tumors, resulting in an MCM2-positive rate similar to
568 controls (Fig. 8c). This demonstrates that induction of WNT signaling after RAF/MEK inhibition
569 acts to prevent residual BPN tumor cells from entering quiescence. Although the addition of short-
570 term LGK-974 to RAF/MEK inhibition did not reduce tumor burden beyond RAF/MEK inhibition
571 alone (Supplementary Figure 8d), our data show that the biology of residual tumor cells can be
572 manipulated by modulating WNT signaling.

573 To expand upon these results, we performed a larger experiment in which we combined
574 RAF/MEK inhibition with either WNT inhibition (LGK-974) or CDK4/6 inhibition (Palbociclib) for

575 four weeks. We analyzed a subset of mice at the end of 4 weeks of drug treatment and performed
576 a survival study on the remaining mice. In mice analyzed immediately after the final dose of drug,
577 we found that adding either LGK-974 or Palbociclib to RAF/MEK inhibitors increased the number
578 of cells in quiescence compared to RAF/MEK inhibitor alone (Fig. 8d). Addition of Palbociclib to
579 the RAF/MEK inhibitor also reduced the amount of phospho-RB (S807/811) in the tumors (Fig.
580 8e). These data suggest a model in which elevated WNT signaling in treated BPN tumors prevents
581 cell cycle exit by maintaining higher levels of CDK4/6 activity than in BP tumors treated with the
582 same drug. Our gene expression data suggest that Cyclin D2 is the CDK4/6 partner that is most
583 likely to maintain its activity in treated BPN tumors.

584 Despite the short term effects of adding a third drug, we did not see a significant increase
585 in survival when either LGK-974 or Palbociclib was added to RAF/MEK inhibitor (Supplementary
586 Figure 8e). This indicates that driving residual BPN cells further into quiescence is not sufficient
587 to prevent tumor rebound after drug cessation.

588

589 **DISCUSSION**

590 LUAD progression is driven not only by activation of MAPK signaling but also by changes
591 in cellular identity. However, the direct impact of dysregulated MAPK activity on LUAD identity
592 itself remains an unexplored problem in lung cancer. This problem is important not only because
593 of the correlation between cellular identity and intrinsic malignant potential, but also because
594 lineage switching has become an increasingly recognized, common mechanism of resistance to
595 therapies targeting the MAPK pathway. A better understanding of this phenomenon would provide
596 new insights into the natural history of LUAD progression as well as the changes in cellular identity
597 that occur as a result of targeted therapy.

598 Analyses of the histologic spectrum of LUAD in patients and mouse models have identified
599 two cellular differentiation programs that impose barriers to lung tumor progression (Camolotto et
600 al., 2018; Snyder et al., 2013; Winslow et al., 2011). Initially, NKX2-1/FOXA1/2 transcriptional

601 networks maintain a well-differentiated pulmonary identity. We have previously shown that
602 downregulation of NKX2-1 and subsequent relocalization of FOXA1 and FOXA2 to the regulatory
603 elements of gastrointestinal lineage genes allows for loss of surfactant proteins, aberrant
604 upregulation of HNF4A and conversion to gastric cell identity. Loss of both differentiation
605 programs can lead to poorly differentiated tumors containing high levels of HMGA2.

606 Human IMAs, which are associated with adverse clinical outcomes, most commonly
607 contain *KRAS* mutations (Cha and Shim, 2017). *BRAF* mutations are also detectable in IMAs, but
608 at reduced frequency compared to LUAD overall. GEMMs have been valuable in explaining the
609 distinct role of NKX2-1 in LUAD driven by *KRAS* and *EGFR* mutations (Maeda et al., 2012; Snyder
610 et al., 2013). In the present study, we show that NKX2-1 is required for optimal LUAD initiation by
611 $BRAF^{V600E}$, but it is dispensable for growth and progression to high grade states in established
612 tumors. In contrast, loss of NKX2-1 consistently promotes tumorigenesis in $KRAS^{G12D}$-driven
613 GEMMs. Taken together, these data explain why *KRAS* mutations are enriched in IMA, whereas
614 *BRAF* mutations are not. It remains to be determined whether co-mutations can render NKX2-1
615 loss advantageous (rather than neutral) in *BRAF*-mutant LUADs. For example, activating codon
616 201 mutations in *GNAS*, which are predicted to drive cAMP-mediated Protein Kinase A (PKA)
617 activity, occur more frequently in IMA than other LUAD subtypes (Ritterhouse et al., 2017).
618 Although functional studies of GNAS mutations in IMA have not been reported, codon 201 GNAS
619 mutants function as oncogenes in KRAS-driven GEMMs of pancreatic cancer, which expresses
620 some of the same foregut markers as IMA (Patra et al., 2018; Taki et al., 2016). In our RNA
621 sequencing, several mRNAs encoding negative regulators of cAMP-mediated signaling to PKA,
622 including *Prkar2b*, *Rgs7*, and *Adra2a* (Garg et al., 2016; Ghavami et al., 2004; Taylor et al., 2008),
623 were significantly upregulated in BPN cells compared to BP. Interestingly, these transcripts were
624 not elevated in *Nkx2-1* deleted KRAS-driven tumor cells (Camolotto et al., 2018) and decreased
625 cAMP-dependent PKA activity may be one reason why tumor initiation is impaired in BPN tumors.

626 We have previously shown that the gastric differentiation state of IMA is driven by
627 transcription factors such as FoxA1/2 and HNF4α. Here, we show that MAPK and WNT signaling
628 provide an additional layer of regulation, modulating the specific cell type that IMA cells most
629 closely resemble within the gastric lineage. Our data reveal that high MAPK activity drives a gene
630 expression program characteristic of the surface mucous cells of the stomach. In contrast, low
631 ERK levels, in concert with high WNT activity, activate gene expression signatures associated
632 with other gastric cell types, including LGR5-positive chief cells and tuft cells. We also show that
633 FoxA1/2 are required for expression of the chief cell markers. Interestingly, hyperactivation of
634 MAPK signaling (via TGF-α mediated activation of EGFR) is observed in Menetrier's disease, a
635 hypertrophic gastropathy characterized by hyperproliferation of isthmus progenitors and the
636 preferential differentiation of these progenitors into surface mucous cells at the expense of parietal
637 and chief cells (Fiske et al., 2009). Blockade of EGFR results in regression of overgrown surface
638 epithelium and restoration of lineage fidelity in progenitors.

639 Importantly, our results identify crosstalk between the MAPK and WNT pathways in IMA
640 tumors, as suppression of MAPK pathway rapidly activates WNT target gene expression. In the
641 mammalian intestine, reciprocal gradients of WNT and phosphorylated ERK1/2 control the
642 balance between proliferation and differentiation of intestinal stem cells (Kabiri et al., 2018). Some
643 molecular mechanisms driving the crosstalk between WNT and ERK signaling have been
644 reported. In one study, reduction of MEK activity via gut-specific ablation of *Ptpn11* decreased
645 abundance of TCF4M/S isoforms while favoring the binding of β-catenin to TCF4E variants, which
646 are more efficient drivers of WNT target gene activation (Heuberger et al., 2014). Alternatively,
647 treatment of BRAF mutant colorectal cancer models with MAPK inhibitors stimulated WNT
648 pathway through the activation of cytoplasmic focal adhesion kinase (FAK) (Chen et al., 2018) or
649 depletion of AXIN1 protein (Zhan et al., 2019), resulting in the stabilization of β-catenin. Although
650 we find no evidence for the above three mechanisms as mediators of ERK/WNT cross-regulation

651 in our lung tumor model, we did identify three candidate genes induced by MAPK inhibition (bulk
652 and single cell RNA-seq) that might account for the increased WNT signaling: *Dixdc1*, *Sox4* and
653 *Sox9* (Fig. 7a). DIXDC1 (aka CCD1) is a scaffolding protein that promotes assembly of
654 Dishevelled into its biologically active, trimeric, form capable of interacting with AXIN and
655 recruiting the destruction complex to the plasma membrane (Liu et al., 2011). SOX4 is a
656 transcription factor that can interact with AXIN-APC destruction complex and interfere with the
657 phosphorylation of β-catenin, thereby increasing its stability (Bhattaram et al., 2014). On the other
658 hand, SOX9 can directly transactivate WNT target genes in specific contexts (Ma et al., 2016).
659 Our preliminary in vitro data indicates that these transcripts are induced by at least 1.5 fold within
660 one hour of Cobimetinib treatment, preceding the upregulation of *Axin2*/*Lgr5*, and continue to
661 accumulate over the course of 24 hours. However, establishing whether any of these factors are
662 required for the interplay between ERK/WNT signaling axes in drug treated IMAs requires further
663 experimental investigation.

664 Our results also have translational implications for LUAD treatment. *BRAF*-mutant LUADs
665 exhibit a heterogenous response to BRAF/MEK inhibition in clinical trials (Planchard et al., 2016;
666 Planchard et al., 2017). Here we identify NKX2-1 as a determinant of treatment response in a
667 GEMM of this disease. In both NKX2-1-positive and NKX2-1-negative tumors, combined
668 BRAF/MEK inhibition leads to substantial tumor regression, but drug-tolerant cells persist with the
669 potential to relapse. In the absence of NKX2-1, residual tumor cells fail to exit the cell cycle. The
670 different cell cycle positions of residual BP and BPN tumor cells suggest that different therapeutic
671 approaches will be needed to eradicate these cells. Indeed, we were able to identify factors
672 mediating these differences, including elevated Cyclin D2-CDK4/6 activity and sustained
673 phosphorylation of RB. We verified that the cell cycle position of drug treated tumor cells can be
674 manipulated by downregulating Cyclin D2 or blocking CDK4/6 activity via Palbociclib. However,
675 these tripartite drug combination strategies were not efficacious in achieving durable tumor
676 regression or survival benefit. It is interesting to consider these results in the context of two recent

677 studies where the combinatorial effect of Palbociclib and MEK inhibitor (Trametinib) was tested in
678 models of KRAS-driven NKX2-1 positive LUAD (Ruscetti et al., 2018) and in KRAS-driven
679 pancreatic ductal adenocarcinoma (PDAC) (Ruscetti et al., 2020). Consistent with our findings,
680 Trametinib/Palbociclib co-administration in both types of mice elicited a potent inhibition of RB
681 phosphorylation. In addition, combination therapy in KRAS-driven lung tumors resulted in
682 prominent induction of cellular senescence and infiltration of tumors with activated NK cells, which
683 drove tumor cell clearance, and markedly increased survival in dual-treatment mice compared to
684 single agent treated mice (Ruscetti et al., 2018). In PDAC models, however, dual treatment
685 elicited tumor senescence but not NK cell recruitment and failed to elicit robust tumor regression
686 (Ruscetti et al., 2020). Importantly, BPN tumors have a gastric/foregut-like differentiation state
687 that is much closer to PDAC than to KRAS-driven NKX2-1 positive LUAD. Thus, our results
688 expand upon these published observations that lineage state can influence the response to
689 combined inhibition of MAPK and CDK4/6 activity. It appears that immune cell composition of
690 NKX2-1^{+} and NKX2-1^{-} LUAD GEMMs can be distinct (Mollaoglu et al., 2018). Thus, investigations
691 into the tumor microenvironment of IMAs and how it is impacted by combination therapies may
692 also provide important clues as to the mechanisms that maintain drug tolerant states.

693 Additional work is clearly needed to identify specific vulnerabilities of residual IMA cells
694 after MAPK inhibition. The lineage switch we observe in both KRAS and BRAF-driven IMA models
695 is likely to be relevant to the identification of such vulnerabilities. MAPK inhibition causes IMA
696 cells to undergo an identity shift from a surface mucous cell-like phenotype toward a more gastric
697 stem cell-like state or tuft cell identity. These observations support the broader notion that tumor
698 cell plasticity includes the capacity to explore myriad cell states from the developmental repertoire.
699 Lineage switching may be particularly beneficial for tumor cells under the selective pressure of
700 targeted therapy, as diverse lineage programs have distinct dependencies on specific growth and
701 survival mechanisms. We speculate that cell identity changes within the gastric lineage may
702 render residual IMA cells susceptible to specific therapeutic interventions. This would be

703 reminiscent of prior studies of basal cell carcinoma of the skin showing that an identity switch
704 confers resistance to inhibition of the Hedgehog pathway while rendering the cells susceptible to
705 blockade of WNT signaling (Biehs et al., 2018; Sanchez-Danes et al., 2018).
706 In summary, this study characterizes the context-dependent role of NKX2-1 in LUAD and
707 identifies novel mechanisms of cell identity regulation and therapeutic response in this disease
708 (Figure 8g). The data provide new insights into the complex interplay between lineage specifiers,
709 oncogenic signaling pathways and the susceptibility of lung cancer cells to targeted therapy. Thus,
710 in the interest of developing fully effective therapies, these studies call for deep cataloguing of cell
711 states sampled by tumor cells as well as their state-specific vulnerabilities.
712
713 **MATERIALS AND METHODS**
714 *Mice, tumor initiation and drug treatment in vivo*
715 All animal work was done in accordance with a protocol approved by the University of
716 Utah Institutional Animal Care and Use Committee. The following mouse strains were used.
717

Genotype designation	**Reference**	**Identifiers**	**Additional Information**
BRaf$^{CA/+}$	Dankort et al. 2007 PMID 17299132	MGI:3711771	Dr. Martin McMahon (HCI, Salt Lake City, Utah)
BRaf$^{FA/+}$	Shai et al. 2015 PMID 26001956	MGI:	Dr. Martin McMahon (HCI, Salt Lake City, Utah)
Trp53$^{F/F}$	Jonkers et al. 2001 PMID 11694875	MGI:1931011	Dr. Anton Berns, University of Amsterdam; Jackson Laboratories (Bar Harbor, Maine)

Trp53$^{frt/frt}$	Lee et al. 2012 PMID 22228755	MGI:5306612	Dr. David G Kirsch (Duke University Medical Center, Durham, North Carolina)
KRas$^{LSL\text{-}G12D/+}$	Jackson et al. 2001 PMID 11751630	MGI:2429948	Dr. Tyler Jacks (MIT, Cambridge, Massachusetts)
KRas$^{FSF\text{-}G12D/+}$	Young et al. 2011 PMID 21512139	MGI:5007794	Dr. Tyler Jacks (MIT, Cambridge, Massachusetts)
Nkx2-1$^{f/f}$	Kusakabe et al. 2006 PMID 16601074	MGI: 3653706	Dr. Shioko Kimura (NCI, NIH, Bethseda, Maryland)
Rosa26 *LSL-tdTomato*	Madisen et al. 2010 PMID 20023653	MGI: 4436847	Jackson Laboratories (Bar Harbor, Maine)
Rosa26 *FSF-Cre*^{ERT2}	Schonhuber et al. 2014 PMID 25326799	MGI: 5616874	Dr. Dieter Saur (Technische Universitat Munchen, Munchen, Germany)
Foxa1$^{F/F}$	PMID 19141476	MGI: 3831163	Dr. Klaus H. Kaestner (Univ. of Pennsylvania School of Medicine, Philadelphia, PA)
Foxa2$^{F/F}$	PMID 10866673	MGI: 2177357	Dr. Klaus H. Kaestner (Univ. of Pennsylvania School of Medicine, Philadelphia, PA)

718 Tumors were generated by administering mice with PGK-Cre lentivirus at 5 x 10^3 plaque
719 forming units (pfu)/mouse, Ad5CMVFlpO at 2 x 10^7 pfu/mouse; Ad5CMVCre 2.5 x 10^7 pfu/mouse,
720 Ad5SpcCre 5-8 x 10^8 pfu/mouse or pCDH-CRE 2 x 10^4 pfu/mouse. Adenovirus was obtained from
721 University of Iowa Viral Vector Core.
722 Rodent Lab Diet (AIN-76A) was formulated with the vemurafenib-related compound
723 PLX4720 at 200 mg/kg (Tsai et al., 2008) and PD0325901 7 mg/kg (Trejo et al., 2012). Drug
724 formulation was by Plexxikon and chow manufacture was by Research Diets. AIN-76A was used
725 as control chow. Mice were maintained on the indicated drug pellets for the indicated time periods.
726 BrdU incorporation was performed by injecting mice at 50 mg/kg (Sigma) intraperitoneally 1 hour
727 prior to necropsy. Mice in survival studies were monitored for lethargy and respiratory distress, at
728 which time animals were euthanized.
729 LGK-974 and Palbociclib (Selleck Chemicals) were delivered to mice via oral gavage.
730 LGK-974 was formulated in 0.5% (w/v) methylcellulose/0.5% (v/v) Tween-80 solution and given
731 at 7.5mg/kg dose with 5 days ON/ 2 days OFF schedule for 2 weeks (Figures 8C, S8D) or 4
732 weeks (Figures 8D, 8E, S8E). Weights were monitored once or twice weekly and no toxicity was
733 observed in mice. Palbociclib was formulated in 50mM Sodium Lactate and initially given at
734 120mg/kg dose with 5 days ON/ 2 days OFF schedule. Weights were monitored once or twice
735 weekly. Due to weight loss in female mice receiving Palbociclib + MAPK-inhibitor chow
736 combination, the following modifications were made for all mice receiving Palbociclib as single or
737 dual agent. On week 2: 120mg/kg dose with 4 days ON/3 days OFF schedule; week 3: Palbociclib
738 was skipped altogether; week 4: 100mg/kg dose with 4 days ON/3 days OFF schedule.
739
740 *Tamoxifen and Doxycycline administration*
741 Tumor-specific activation of $CreER^{T2}$ nuclear activity was achieved by intraperitoneal
742 injection of tamoxifen (Sigma) dissolved in corn oil at a dose of 120 mg/kg. Mice received a total

743 of 6 injections over the course of 9 days. For survival experiments, mice were additionally given
744 pellets supplemented with 500 mg/kg tamoxifen (Envigo).
745
746 *Cell lines and cell culture*
747 HEK-293T cells were cultured in DMEM/High Glucose medium (Gibco). L-WRN cells
748 (ATCC) were cultured in DMEM/High Glucose medium containing G418 (Sigma) and Hygromycin
749 (InvivoGen) media. All media contained 10% FBS (Sigma). To eliminate mycoplasma
750 contamination, cell lines were treated with 25 µg/mL Plasmocin (InvivoGen) for 2-3 weeks. To
751 maintain cultures mycoplasma free, media were supplemented with 2.5 µg/mL Plasmocin. Cell
752 line identity was authenticated using STR analysis at the University of Utah DNA Sequencing
753 Core.
754
755 *Establishing primary lung organoids*
756 8-10 weeks after tumor initiation with PGK-Cre, tumor bearing mice were euthanized and
757 lungs were isolated. Lungs were then minced under sterile conditions and digested at 37ºC for 30
758 mins with continuous agitation in a solution containing the enzymes, Collagen Type I (Thermo
759 Fisher Scientific, at 450 U/ml final); Dispase (Corning, at 5 U/ml); DNaseI (Sigma, at 0.25 mg/ml)
760 and Antibiotic-Antimycotic solution (Gibco). The digested tissue was passed through an 18 or 20-
761 gauge syringe needle. Enzyme reactions were then stopped by addition of cold DMEM/F-12 with
762 10% FBS and the cell suspension was dispersed through 100 µm, 70 µm and 40 µm series of cell
763 strainers to obtain single cell suspension. Subsequently, cell pellets were treated with erythrocyte
764 lysis buffer (eBioscience). Finally, cell pellets were reconstituted in Advanced DMEM/F-12 (Gibco)
765 supplemented with L-glutamine, 10 mM HEPES, and Antibiotic-Antimycotic. Thereafter, 100,000
766 tumor cells were mixed with 50 µl of Matrigel (Corning) at 1 to 10 ratio and plated in 24-well plates.
767 For the first week of organoid initiation, Matrigel droplets were overlaid with recombinant organoid
768 medium (Advanced DMEM/F-12 supplemented with 1X B27 (Gibco), 1X N2 (Gibco), 1.25 mM

769 nAcetylcysteine (Sigma), 10 mM Nicotinamide (Sigma), 10 nM Gastrin (Sigma) and containing
770 growth factors (100 ng/ml EGF [Peprotech], 100 ng/ml R-spondin1 [Peprotech], 100 ng/ml Noggin
771 [Peprotech], 100 ng/ml FGF10 [Peprotech], as well as the ROCK inhibitor Y27632 [R&D Systems]
772 and the TGF-b type I receptor-inhibitor SB431542 [R&D Systems]) as described in (Barker et al.,
773 2010; Sato et al., 2009).

774 After the initial spheroid culture propagation, organoids were switched to 50% L-WRN
775 conditioned media generated as detailed in (Miyoshi and Stappenbeck, 2013). Briefly, L-WRN
776 cells (ATCC) seeded and maintained in 10% FBS, DMEM high glucose containing 500 µg/ml
777 G418 (Sigma) and 500 µg/ml Hygromycin (InvivoGen) media until confluency. Once confluent, L-
778 WRN cells were switched to Advanced DMEM/F-12 containing 20% FBS, 2 mM L-glutamine, 100
779 U/ml penicillin, 0.1 mg/ml streptomycin. Daily, conditioned supernatant medium was collected
780 from L-WRN cultures, filtered through 0.2 µm vacuum filters and saved at -20°C as stock (100%)
781 L-WRN medium. To use for culturing spheroids, stock L-WRN was diluted with equal volume
782 Advanced DMEM/F-12 (final concentration 50%). Where specified, stock L-WRN media was
783 diluted with Advanced DMEM/F-12 to a final concentration of 5% while still keeping FBS
784 concentration at 10% as described in (VanDussen et al., 2015). For drug studies, organoid media
785 was supplemented with Cobimetinib, GDC-0994 (Genentech), LGK-974, PD0325901, PLX-4720
786 (Selleck Chemicals) at indicated concentrations. Drug containing media was refreshed every 48-
787 72hrs.

788

789 *Lentiviral production and transduction*

790 HEK293T cells were transfected with CRE/FLPO-encoding lentiviral vector, d8.9
791 packaging vector and VSV-G envelope vector mixed with TransIT-293 (Mirus Bio). Virus
792 containing supernatant was collected at 36, 48, 60 and 72 hrs after transfection.
793 Ultracentrifugation at 25,000 r.p.m. for 2 hrs was necessary to concentrate virus for in vivo
794 infection.

795 For stable transduction of organoids, organoid cultures were first prepared into single cell
796 suspensions by subjecting them to successive incubations with Cell Recovery Solution (Corning)
797 and TrypLE (Gibco). Cells were then resuspended in a 1:1 mixture, by volume, of 50% L-WRN
798 and lentivirus containing supernatant. After supplementation with 8 µg/ml polybrene, cells were
799 incubated for 2 hours. Cells were then pelleted, mixed back with Matrigel, and seeded. 72 hours
800 later, Puromycin selection for 1 week was performed to achieve stable lines.
801
802 *Flank tumor transplantation*
803 For subcutaneous allograft experiments, $3x10^5$ single cell suspension of 988 BPN
804 organoid cells stably expressing either the Mission® pLKO.1-puro Non Target shRNA control
805 (shscr) or one of the validated *Ccnd2* Mission® shRNAs, TRCN0000054764 (#64) or
806 TRCN0000054766 (#66), were mixed with in 1:1 volume with 50µl Matrigel. Cells were injected
807 subcutaneously into the right or left flanks of NOD/SCID-gamma chain deficient (NSG) mice.
808 Tumor dimensions were measured with calipers. Tumor volume was calculated using the (L x
809 W^2)/2 formula. When the majority of the tumors reached ~$200mm^3$, mice were randomized into
810 control or drug groups, the latter of which received RAF/MEK inhibitor compounded chow for 4
811 weeks. Tumor volume measurements were not reliable as the tumors formed from organoid
812 cultures became fluid-filled cysts rather than solid. At end of treatment period, tumors were
813 removed and processed for histological analyses.
814
815 *Real-time PCR*
816 Total RNA was isolated using TRIzol followed by PureLink RNA Mini Kit (Thermo Fisher
817 Scientific). RNA was treated with RNase-Free DNAse I (Invitrogen) on-column. For low cell
818 numbers (e.g. after FACS), Animal Tissue RNA Purification Kit (Norgen Biotek) was used instead.
819 RNA was converted to cDNA using iScript Reverse Transcription Supermix (BioRad). cDNA was
820 analyzed either by SYBR green real-time PCR with SsoAdvanced Universal SYBR Green

821 Supermix (BioRad) or by Taqman real-time PCR with SsoAdvanced Universal Probes Supermix
822 (BioRad) using a CFX384 Touch Real-Time PCR Detection System (BioRad). Gene expression
823 was calculated relative to *Ppia* (loading control) using the $2^{-(dCt.x-average(dCt.control))}$ method and
824 normalized to the control group for graphing. Primer sequences and TaqMan Assays used in this
825 study are listed below.
826 *Ppia* (F), TGTGGTCTTTGGGAAGGTGAA; *Ppia* (R), AAATGGTGATCTTCTTGCTGGT
827 *Muc5ac* (F), GTGGTTTGACACTGACTTCCC; *Muc5ac* (R), CTCCTCTCGGTGACAGAGTCT
828 *Ppia* Mm02342429_g1; *Muc5ac* Mm01276718_m1; *Gkn1* Mm01183898_m1
829 *Pgc* Mm00482488_m1; *Cym* Mm01204823_m1; *GIF* Mm00433596_m1
830 *Pou2f3* Mm00478293_m1; *Gfi1b* Mm00492318_m1; *Lgr5* Mm00438890_m1
831 *Axin2* Mm00443610_m1; *Ccnd1* Mm00432359_m1; *Ccnd2* Mm00438070_m1
832
833 *Cell viability and growth assay*
834 For organoids, cells were seeded at a density of 2000 cells per 15 µl Matrigel dome, 4
835 domes per line per time point, each dome in a single well of a 96-well plate. After overnight culture,
836 organoids were treated with different concentrations of the indicated inhibitors and incubated at
837 37°C for indicated times. Subsequently, the relative number of viable cells was measured by by
838 CellTiter-Glo 3D Cell Viability Assay (Promega), according to the manufacturer's instructions.
839 Luminescence was then measured by a microplate reader (EnVision 2105 Multimode Plate
840 Reader, PerkinElmer). Replicate values for each experimental group were averaged and all
841 values were normalized to control treatment group for each line.
842
843 *Immunoblot Analysis*
844 Cells were lysed on ice using RIPA buffer (50 mM HEPES, 140 mM NaCl, 1 mM EDTA,
845 1% triton X-100, 0.1% sodium deoxycholate and 0.1% SDS) supplemented with protease and

846 phosphatase inhibitor cocktails (Roche). Protein extracts were clarified and concentrations were
847 measured with Pierce Coomassie Plus Protein Assay reagent (Thermo Fisher Scientific). Lysates
848 were then resolved on SDS-PAGE gels (BioRad), and transferred to Nitrocellulose blots.
849 Membranes were probed with primary antibodies against AXIN1 (2087, CST), TCF4 (2569, CST)
850 pFAK Y397 (SAB4504403, Sigma), DUSP6 (EPR129Y, Abcam), SPRY2 (EPR4318(2)(B),
851 Abcam), pERK (4370, CST), tERK (4696, CST), Vinculin (EPR8185, Abcam) and β-tubulin (E7,
852 DSHB). Blots were subsequently incubated with HRP conjugated secondary antibodies. For
853 signal development, Supersignal West Femto Substrate kit (Thermo Fisher Scientific) was used,
854 followed by image acquisition using darkroom development. ImageJ was used for band intensity
855 quantitation.
856
857 *Histology and immunohistochemistry*
858 Lung tissues were fixed overnight in 10% neutral buffered formalin, processed through
859 70% ethanol, embedded in paraffin, and sectioned at 4 µm thickness. Staining of hematoxylin and
860 eosin, as well as detection of mucin by Alcian Blue were carried out at the HCI Research Histology
861 Shared Resource. Immunohistochemistry was performed manually as detailed in (Camolotto et
862 al., 2018). The following primary antibodies were used. BrdU (BU1/75, Abcam), Cathepsin E (LS-
863 B523, Lifespan Biosciences), Galectin 4 (AF2128, R and D Systems), Gastrokine 1 (2E5,
864 Abnova), Histone H3 pSer10 (Abcam), HNF4A (C11F12, CST), MCM2 (ab31159, Abcam),
865 Muc5AC (SPM488, Abnova), NKX2-1 (EP1584Y, Abcam), PDX1 (F109-D12, DSHB), RFP
866 (Rockland Immunochemicals), pERK1/2 (D13.14.4E, CST), p4EBP1 T37/46 (2855, CST), pS6
867 S235/236 (D57.2.2E, CST), pS6 S240/244 (D68F8, CST), pMEK1/2 S221 (166F8, CST),
868 Pepsinogen C (HPA031718, Sigma), POU2F3 (HPA019652, Sigma), pRB S807/811 (8516,
869 CST). Pictures were taken on a Nikon Eclipse Ni-U microscope with a DS-Ri2 camera and NIS-
870 Elements software. Tumor quantitation was performed on hematoxylin and eosin-stained or IHC-

871 stained slides using NIS-Elements software. All histopathologic analysis was performed by a
872 board-certified anatomic pathologist (E.L.S.).
873
874 *Primary human tumors*
875 De-identified formalin fixed, paraffin-embedded (FFPE) tumors were obtained from the
876 Intermountain Biorepository, which collects samples in accordance with protocols approved by
877 the Intermountain Healthcare Institutional Review Board. Mucinous tumors were included in the
878 study based on the following criteria: 1. Diagnosis of invasive mucinous adenocarcinoma; OR 2.
879 Diagnosis of mucinous bronchioloalveolar carcinoma (older diagnostic term for IMA); OR 3.
880 Mucinous lung adenocarcinoma with strong morphologic features of IMA, such as abundant
881 intracellular mucin. Colloid adenocarcinomas were excluded, as these are considered to be a
882 discrete subtype of lung cancer.
883
884 *Fluorescence-activated cell sorting (FACS) for in vivo tumors and in vitro organoid cultures*
885 Tumor bearing lungs were isolated in ice-cold PBS. Lungs were enzymatically digested
886 as described above in the procedure for establishing primary organoids. Once single cell
887 suspensions were obtained, cells were reconstituted in phenol red-free DMEM/F-12 with HEPES
888 containing 2% FBS, 2% BSA and DAPI. Cells were sorted using BD FACS Aria for tdTomato-
889 positive and DAPI-negative cells into DMEM/F-12 and 30% serum. After sorting, cells were
890 pelleted and flash frozen or resuspended TRIzol then frozen at -80°C.
891 To study the dynamics of WNT signaling in vitro, BPN organoids were stably transduced
892 with the β-catenin/TCF-dependent GFP reporter lentiviral construct 7TGP (Addgene plasmid
893 #24305). Single cells were isolated from Matrigel using Cell Recovery Solution and TrypLE
894 incubations. Cells were analyzed on BD LSRFortessa or BD FACSAria and sorted on BD
895 FACSAria. Events first passed through a routine light-scatter and doublet discrimination gates,
896 followed by exclusion of DAPI-positive dead cells. Viable tumor organoids were further identified

897 as tdTomato-high cells. 7TGP organoids grown in 5% L-WRN media for 2 – 3 days were used as
898 control for setting the GFP-negative gate. This gating strategy was applied to 7TGP organoids
899 that were cultured in standard 50% L-WRN media in order to identify and sort for the WNT-
900 reporter-low fraction. This fraction was collected in 50% L-WRN and expanded for ~1 week. After
901 expansion, sorted 7TGP organoids were seeded and treated with 50% L-WRN (± Cobimetinib) or
902 5% L-WRN (± Cobimetinib) for 24h, 48h and 72h. Then, the fraction of WNT-reporter-high
903 population under the above four conditions was analyzed. Flow cytometric data analyses was
904 performed using FlowJo software.
905
906
907 *Bulk RNA sequencing*
908 Library preparation was performed using the TruSeq Stranded mRNA Library Preparation
909 Kit with poly(A) selection (Illumina). Purified libraries were qualified on an Agilent Technologies
910 2200 TapeStation using a D1000 ScreenTape assay. The molarity of adapter-modified molecules
911 was defined by quantitative PCR using the Kapa Biosystems Kapa Library Quant Kit. Individual
912 libraries were normalized to 5nM and equal volumes were pooled in preparation for Illumina
913 sequence analysis. Libraries were sequenced on Illumina HiSeq 2500 (50 cycle single-read
914 sequencing v4).
915
916 *Bulk RNAseq analysis*
917 Adapters in raw FASTQ files containing 50-bp single-end reads were trimmed with
918 cutadapt. QC metrics were generated for each sample with FastQC and Picard's
919 CollectRnaSeqMetrics after aligning reads to genome with STAR (Dobin et al., 2013). QC metrics
920 were summarized by MultiQC. From this QC analysis, one sample (id 14489X13) did not group
921 with other samples in the MultiQC report. It was later confirmed that very limited starting material
922 was a contributing factor to its difference from the others. This sample was removed from

923 downstream analysis because the noise in the sample was likely a larger negative trade-off than
924 the gains from increasing biological replicates for that condition.

925 Next, Salmon v0.9.1 quantified RNA transcript expression with two steps (Patro et al.,
926 2017); first, the mouse transcriptome downloaded from Gencode (release 26) was indexed using
927 k-mers of length 19 with type 'quasi'; second, Salmon quasi-mapped reads and corrected for
928 sequence-specific bias (see option –seqBias). Salmon-based transcript expression estimates
929 were converted to gene expression estimates with R package tximport (Soneson et al., 2015).
930 Differential gene expression modeling with DESeq2 (Love et al., 2014) and EdgeR (Robinson et
931 al., 2010) evaluated 4 distinct contrasts testing (i) genotype effects within control groups [BP C
932 vs. BPN C]; (ii) genotype effects within treatment groups [BP Tx vs. BPN Tx]; (iii) treatment effects
933 within BP genotype [BP C vs. BP Tx]; (iv) treatment effects within BPN genotype [BPN C vs. BPN
934 Tx]. Prior to fitting a single-factor DESeq2 regression (4 factor levels: BP C, BPN C, BP Tx, BPN
935 Tx), genes were filtered if there were less than 5 total counts across all samples. PCA was done
936 on the top 500 most variable genes subject to a regularized log transform to confirm within-group
937 variation was similar. A Wald test was applied to the fitted model for each of the 4 contrasts
938 specified above, where the null hypothesis was gene expression differences less than or equal to
939 log2(2) fold change in absolute value and the alternative hypothesis was that differences exceed
940 log2(2). Significance of gene-wise differences was controlled by a false discovery rate of 10%
941 (Benjamini and Hochberg, 1995).

942 Differential gene expression modeling with EdgeR for volcano plots used package
943 edgeR_3.24.3 with ggplot2_3.1.1. Significance of gene-wise differences was calculated by tag-
944 wise exact test. WNT signaling genes were delineated in the bulk sequencing matrix using AmiGO
945 pathway annotations (http://amigo.geneontology.org) for "Wnt Signaling" (Carbon et al., 2008).
946 WNT genes were restricted to those annotated for *mus musculus* with direct experimental
947 evidence. The most differentially expressed genes between treated and untreated sample groups
948 (Bonferonni corrected Student's t-test) were thresholded at >2 fold change between means of

949 treated and untreated samples. The 13 genes meeting this criterion and showing upregulation in
950 RAF/MEK inhibitor treated cells (BPN Tx) was designated as the WNT13 signature in this study.
951 Gene set enrichment analysis (GSEA) was carried out on bulk data (and single cell data
952 (below)) by comparing gene expression profiles with archived gene sets from Hallmarks
953 [ftp.broadinstitute.org://pub/gsea/gene_sets/h.all.v7.0.symbols.gmt] and Oncogenic signatures
954 [ftp.broadinstitute.org://pub/gsea/gene_sets/c6.all.v7.0.symbols.gmt] as well as with the cell type
955 specific genes sets described in (Haber et al., 2017; Leushacke et al., 2017; Montoro et al., 2018;
956 Zhang et al., 2019).
957
958 *Single-cell RNA sequencing*
959 All protocols to generate scRNA-seq data on 10x Genomics Chromium platform
960 including library prep, instrument and sequencing setting can be found at:
961 https://support.10xgenomics.com/single-cell-gene-expression
962 The Chromium Single Cell Gene Expression Solution with 3' chemistry, version 3 (PN-1000075)
963 was used to barcode individual cells with 16 bp 10x Barcode and to tag cell specific transcript
964 molecules with 10 bp Unique Molecular Identifier (UMI) according to the manufacturer's
965 instructions. The following protocol was performed at High-Throughput Genomics Shared
966 Resources at Huntsman Cancer Institute, University of Utah. First, FACS sorted single cell
967 suspensions of tdTomato-positive lung tumors were resuspended in phosphate buffered saline
968 with 0.04% bovine serum albumin. The cell suspension was filtered through 40 micron cell
969 strainer. Viability and cell count were assessed on Countess I (Thermo Scientific). Equilibrium to
970 targeted cell recovery of 6,000 cells, along with 10x Gel Beads and reverse transcription reagents
971 were loaded to Chromium Single Cell A (PN-120236) to form Gel Beads-in emulsions (GEMs),
972 the nano-droplets. Within individual GEMs, cDNA generated from captured and barcoded mRNA
973 was synthesized by reverse transcription at the setting of 53°C for 45 min followed by 85°C for 5
974 min. Subsequent A tailing, end repair, adaptor ligation and sample indexing were performed in

975 bulk according to the manufacturer's instructions. he resulting barcoding libraries were qualified
976 on Agilent D1000 ScreenTape on Agilent Technology 2200 TapeStation system and quantified
977 by quantification PCR using KAPA Biosystems Library Quantification Kit for Illumine Platforms
978 (KK4842). Multiple libraries were then normalized and sequenced on NovaSeq 6000 with 2x150
979 PE mode.
980
981 *Single-cell RNAseq analysis*
982 Demultiplexing and data alignment: Single cell RNAseq data were demultiplexed with 10x
983 cellranger mkfastq version 3.1.0 to create fastq files with the I1 sample index, R1 cell
984 barcode+UMI and R2 sequence. Reads were aligned to the mouse genome (mm10 with custom
985 tdTomato reference) and feature counts were generated using cellranger count 3.1.0 with
986 expected-cells set to 6000 per library. QC reporting, clustering, dimension reduction, and
987 differential gene expression analysis were performed in 10x Genomics' Cell Loupe Browser
988 (v3.1.1). For the BPN control sample, we captured 5,065 cells and obtained 46,894 mean reads
989 per cell; 3,544 median genes per cell. For the BPN treated sample, we captured 5,563 cells and
990 obtained 37,488 mean reads per cell; 2,771 median genes per cell. For further details of the
991 primary Cell Ranger data processing, see https:// support.10xgenomics.com/single-cell-gene-
992 expression/software/pipelines/latest/algorithms/.
993 Visualization and expression analysis: Single cell expression data was analyzed using
994 Seurat (3.1.0) (Butler et al., 2018; Stuart et al., 2019) and visualized in Loupe browser (3.1.1).
995 Alternatively, single cell data was processed mostly in R (3.5.1). Cells with unique feature counts
996 over 7,500 or less than 200 and more than 20% mitochondrial counts have been filtered out. For
997 visualization, the umap-learn package, from Seurat (McInnes et al., 2018), was used to reduce
998 the dimensionality of the data.
999 Clustering: The Seurat package clustering method was used to designate cluster
1000 membership of single cell transcriptomics profiles. Seurat clustering is heavily inspired by (Levine

1001 et al., 2015; Xu and Su, 2015), which has 2 steps in the first step, the findNeighbors function is
1002 employed to embed single cell profiles in a K-nearest neighbor (KNN) graph based euclidean
1003 distance in a (20 PCs) PCA space, followed by refining the edge weights based on jaccard
1004 similarity (https://satijalab.org/seurat/v3.0/pbmc3k_tutorial.html). In the second step, the
1005 FindClusters function employs Louvain algorithm modularity optimization techniques to iteratively
1006 group cells together (https://satijalab.org/seurat/v3.0/pbmc3k_tutorial.html).

1007 Stromal cell designations: Clusters of cells sharing highly similar positions in
1008 dimensionality reduced UMAP-space were examined for differential expression using Loupe
1009 browser's built-in differential expression calculator, and genes showing significant cluster specific
1010 expression were screened manually against the literature for markers of known cell types. Those
1011 clusters representing minority populations that were highly distinct in Umap-space from the bulk
1012 of cells in the analysis and which bear distinctive expression of stromal marker genes were
1013 considered as stromal contaminants and removed from subsequent, tumor-specific Umap data
1014 visualization and cluster specific gene expression level analysis.

1015 Differential Gene Expression using Seurat: For the DEG test the "FindMarkers" function
1016 from the Seurat package with default setting was used, including Wilcoxon Rank Sum test, and
1017 Bonferroni multi-testing correction based on the total number of genes in the dataset.

1018 Cell cycle phase modeling: We calculated cell cycle scores of control and treated tumor
1019 cells in scRNA-seq data using the Seurat package and the cell cycle genes defined by (Mizuno
1020 et al., 2009). The Seurat package uses the scoring strategy described in (Tirosh et al., 2016) and
1021 assigns scores for cells based on the expression of G2/M and S phase marker genes, with low
1022 scoring cells defaulting to G1. In an alternative approach, we modeled cell cycle phase by
1023 determining mean expression per cell of each phased cell cycle signature described in (Mizuno
1024 et al., 2009). A matrix of these values was then graphed as a diffusion map using the Destiny
1025 package (Angerer et al., 2015) in R. A coherent cell cycle loop through three dimensional space
1026 using the first three diffusion components was projected onto two dimensions using an heuristic

1027 arithmetic, diffusion component combination. To this graph a principal curve was fit using
1028 Princurve (Hastie and Stuetzle, 1989) and tangents for each point (lambdas) were used as cellular
1029 positions along a trajectory designated as Q-depth based on the observed position of G0-
1030 signature enriched cells (an indicator related to quiescence) at the extreme distal to cells enriched
1031 in G1 signatures or the S and G2/M signatures.

1032 MEK activation signature and WNT signature expression: Average expression of an 18
1033 gene signature from Dry et al. (Dry et al., 2010) was determined per cell across the single cell
1034 data set to model MEK activation state. Enrichment for the WNT13 signature described above
1035 was similarly examined across the single cell dataset.

1036 Data Imputation: We used a novel data imputation approach to model the expression of
1037 low-detection genes in single cell data (https://github.com/elnazmirzaei/Fiesta; Mirzaei
1038 Merhabad and Spike et al, *unpublished*). Briefly, a weighted non-negative matrix factorization
1039 was carried out on the single cell data matrix using machine learning based factor optimization.
1040 Subsequently, optimized factors were used to reconstruct an idealized completed matrix with
1041 values recommended for many gene nodes that were originally below the detection threshold.

1042 Recombination fidelity: Cluster specific BAM files were parsed from the concatenated
1043 scRNA-Seq BAM files using subset-bam tool (https://github.com/10XGenomics/subset-bam). The
1044 presence of select splice junctions was visualized using IGV (version 2.7.2) (Robinson et al.,
1045 2011) against mouse genome version (mm10).

1046

1047 *Statistics*

1048 p-Values were calculated using the unpaired two-tailed t-test. RNAseq statistics are
1049 described above.

1050

1051 **DATA AVAILABILITY**

1052 All sequencing data generated in this study are available at Gene Expression Omnibus (GEO:
1053 GSE145152).
1054

1055 **ACKNOWLEDGEMENTS**

1056 We are grateful to members of the Snyder lab for suggestions and comments. We acknowledge
1057 Plexxikon for providing PLX4720 and PD0325901; Research Diets for compounding. We thank
1058 Brian Dalley and Opal Allen for sequencing expertise, Chris Conley for RNA sequencing data
1059 analysis expertise, James Marvin for FACS expertise and David H Lum and members of the
1060 Preclinical Research Shared Resource core for in vivo drug administration. Work in the flow
1061 cytometry core was supported by the National Center for Research Resources of the National
1062 Institutes of Health under Award Number 1S20RR026802-1. Research reported in this publication
1063 utilized shared resources (including Flow Cytometry, High Throughput Genomics, Bioinformatics,
1064 Biorepository and Molecular Pathology, and Preclinical Research Resource) at the University of
1065 Utah and was supported by Huntsman Cancer Foundation and the National Cancer Institute of
1066 the National Institutes of Health under Award Number P30CA042014. E.L.S. was supported in
1067 part by a Career Award for Medical Scientists from the Burroughs Wellcome Fund, a V Scholar
1068 Award, the NIH (R01CA212415, R01CA240317), a Pilot Project Award from the Lung Cancer
1069 Center of the Huntsman Cancer Institute, and institutional funds (Department of Pathology and
1070 Huntsman Cancer Institute, University of Utah). GO was supported by the NIH (F31CA243427
1071 and the Eunice Kennedy Shriver National Institute of Child Health & Human Development of the
1072 National Institutes of Health under Award Number T32HD007491). The content is solely the
1073 responsibility of the authors and does not necessarily represent the official views of the NIH.
1074

1075 **COMPETING INTERESTS**

1076 None.
1077

1078 **AUTHORS' CONTRIBUTIONS**

1079 Conception and design: ELS, RZ; Acquisition of data: RZ, ELS, PF, KG; Computational analysis:
1080 BS, EMM; Technical/material support: KI, SAC, GO, AJ, MCM; Writing, review of manuscript: all;
1081 Study supervision: ELS

1082

1083 **REFERENCES**

1084

1085 Angerer, P., Haghverdi, L., Büttner, M., Theis, F. J., Marr, C., and Buettner, F. (2015). destiny:
1086 diffusion maps for large-scale single-cell data in R. Bioinformatics *32*, 1241-1243.

1087 Barker, N., Huch, M., Kujala, P., van de Wetering, M., Snippert, H. J., van Es, J. H., Sato, T.,
1088 Stange, D. E., Begthel, H., and van den Born, M. (2010). Lgr5+ ve stem cells drive self-renewal
1089 in the stomach and build long-lived gastric units in vitro. Cell stem cell *6*, 25-36.

1090 Barker, N., Van Es, J. H., Kuipers, J., Kujala, P., Van Den Born, M., Cozijnsen, M., Haegebarth,
1091 A., Korving, J., Begthel, H., and Peters, P. J. (2007). Identification of stem cells in small intestine
1092 and colon by marker gene Lgr5. Nature *449*, 1003.

1093 Barletta, J. A., Perner, S., Iafrate, A. J., Yeap, B. Y., Weir, B. A., Johnson, L. A., Johnson, B. E.,
1094 Meyerson, M., Rubin, M. A., Travis, W. D.*, et al.* (2009). Clinical significance of TTF-1 protein
1095 expression and TTF-1 gene amplification in lung adenocarcinoma. J Cell Mol Med *13*, 1977-1986.

1096 Benjamini, Y., and Hochberg, Y. (1995). Controlling the false discovery rate: a practical and
1097 powerful approach to multiple testing. Journal of the Royal statistical society: series B
1098 (Methodological) *57*, 289-300.

1099 Bhattaram, P., Penzo-Méndez, A., Kato, K., Bandyopadhyay, K., Gadi, A., Taketo, M. M., and
1100 Lefebvre, V. (2014). SOXC proteins amplify canonical WNT signaling to secure nonchondrocytic
1101 fates in skeletogenesis. Journal of Cell Biology *207*, 657-671.

1102 Biehs, B., Dijkgraaf, G. J. P., Piskol, R., Alicke, B., Boumahdi, S., Peale, F., Gould, S. E., and de
1103 Sauvage, F. J. (2018). A cell identity switch allows residual BCC to survive Hedgehog pathway
1104 inhibition. Nature *562*, 429-433.

1105 Butler, A., Hoffman, P., Smibert, P., Papalexi, E., and Satija, R. (2018). Integrating single-cell
1106 transcriptomic data across different conditions, technologies, and species. Nature biotechnology
1107 *36*, 411.

1108 Camolotto, S. A., Pattabiraman, S., Mosbruger, T. L., Jones, A., Belova, V. K., Orstad, G., Streiff,
1109 M., Salmond, L., Stubben, C., and Kaestner, K. H. (2018). FoxA1 and FoxA2 drive gastric
1110 differentiation and suppress squamous identity in NKX2-1-negative lung cancer. Elife *7*, e38579.

1111 Campos-Parra, A. D., Aviles, A., Contreras-Reyes, S., Rojas-Marin, C. E., Sanchez-Reyes, R.,
1112 Borbolla-Escoboza, R. J., and Arrieta, O. (2014). Relevance of the novel IASLC/ATS/ERS
1113 classification of lung adenocarcinoma in advanced disease. Eur Respir J *43*, 1439-1447.

1114 Carbon, S., Ireland, A., Mungall, C. J., Shu, S., Marshall, B., Lewis, S., Hub, A., and Group, W.
1115 P. W. (2008). AmiGO: online access to ontology and annotation data. Bioinformatics *25*, 288-289.

1116 Carriere, A., Romeo, Y., Acosta-Jaquez, H. A., Moreau, J., Bonneil, E., Thibault, P., Fingar, D.
1117 C., and Roux, P. P. (2011). ERK1/2 phosphorylate Raptor to promote Ras-dependent activation
1118 of mTOR complex 1 (mTORC1). Journal of Biological Chemistry *286*, 567-577.

1119 Cha, Y. J., and Shim, H. S. (2017). Biology of invasive mucinous adenocarcinoma of the lung.
1120 Translational lung cancer research *6*, 508.

1121 Chen, G., Gao, C., Gao, X., Zhang, D. H., Kuan, S.-F., Burns, T. F., and Hu, J. (2018). Wnt/β-
1122 catenin pathway activation mediates adaptive resistance to BRAF inhibition in colorectal cancer.
1123 Molecular cancer therapeutics *17*, 806-813.

1124 Chen, X., Rosenfeld, C. S., Roberts, R. M., and Green, J. A. (2001). An aspartic proteinase
1125 expressed in the yolk sac and neonatal stomach of the mouse. Biology of reproduction *65*, 1092-
1126 1101.

1127 Cole, A. M., Myant, K., Reed, K. R., Ridgway, R. A., Athineos, D., Van den Brink, G. R., Muncan,
1128 V., Clevers, H., Clarke, A. R., and Sicinski, P. (2010). Cyclin D2–cyclin-dependent kinase 4/6 is
1129 required for efficient proliferation and tumorigenesis following Apc loss. Cancer research *70*,
1130 8149-8158.

1131 Dankort, D., Filenova, E., Collado, M., Serrano, M., Jones, K., and McMahon, M. (2007). A new
1132 mouse model to explore the initiation, progression, and therapy of BRAFV600E-induced lung
1133 tumors. Genes & development *21*, 379-384.

1134 Dobin, A., Davis, C. A., Schlesinger, F., Drenkow, J., Zaleski, C., Jha, S., Batut, P., Chaisson, M.,
1135 and Gingeras, T. R. (2013). STAR: ultrafast universal RNA-seq aligner. Bioinformatics *29*, 15-21.

1136 Dry, J. R., Pavey, S., Pratilas, C. A., Harbron, C., Runswick, S., Hodgson, D., Chresta, C.,
1137 McCormack, R., Byrne, N., and Cockerill, M. (2010). Transcriptional pathway signatures predict
1138 MEK addiction and response to selumetinib (AZD6244). Cancer research *70*, 2264-2273.

1139 Ferrara, M. G., Di Noia, V., D'Argento, E., Vita, E., Damiano, P., Cannella, A., Ribelli, M., Pilotto,
1140 S., Milella, M., and Tortora, G. (2020). Oncogene-Addicted Non-Small-Cell Lung Cancer:
1141 Treatment Opportunities and Future Perspectives. Cancers *12*, 1196.

1142 Fiske, W. H., Tanksley, J., Nam, K. T., Goldenring, J. R., Slebos, R. J., Liebler, D. C., Abtahi, A.
1143 M., La Fleur, B., Ayers, G. D., and Lind, C. D. (2009). Efficacy of cetuximab in the treatment of
1144 Menetrier's disease. Science translational medicine *1*, 8ra18-18ra18.

1145 Garg, A., Sankella, S., Xing, C., and Agarwal, A. K. (2016). Whole-exome sequencing identifies
1146 ADRA2A mutation in atypical familial partial lipodystrophy. JCI Insight *1*.

1147 Ghavami, A., Hunt, R. A., Olsen, M. A., Zhang, J., Smith, D. L., Kalgaonkar, S., Rahman, Z., and
1148 Young, K. H. (2004). Differential effects of regulator of G protein signaling (RGS) proteins on

1149 serotonin 5-HT1A, 5-HT2A, and dopamine D2 receptor-mediated signaling and adenylyl cyclase
1150 activity. Cell Signal *16*, 711-721.

1151 Haber, A. L., Biton, M., Rogel, N., Herbst, R. H., Shekhar, K., Smillie, C., Burgin, G., Delorey, T.
1152 M., Howitt, M. R., and Katz, Y. (2017). A single-cell survey of the small intestinal epithelium.
1153 Nature *551*, 333.

1154 Haghverdi, L., Buettner, F., and Theis, F. J. (2015). Diffusion maps for high-dimensional single-
1155 cell analysis of differentiation data. Bioinformatics *31*, 2989-2998.

1156 Han, S., Fink, J., Jörg, D. J., Lee, E., Yum, M. K., Chatzeli, L., Merker, S. R., Josserand, M.,
1157 Trendafilova, T., and Andersson-Rolf, A. (2019). Defining the identity and dynamics of adult
1158 gastric isthmus stem cells. Cell stem cell.

1159 Hastie, T., and Stuetzle, W. (1989). Source: Journal of the American Statistical Association, Vol.
1160 84, No. 406,(Jun., 1989), pp. 502. Journal of the American Statistical Association *84*, 502.

1161 Heuberger, J., Kosel, F., Qi, J., Grossmann, K. S., Rajewsky, K., and Birchmeier, W. (2014).
1162 Shp2/MAPK signaling controls goblet/paneth cell fate decisions in the intestine. Proceedings of
1163 the National Academy of Sciences *111*, 3472-3477.

1164 Huang, Y.-H., Klingbeil, O., He, X.-Y., Wu, X. S., Arun, G., Lu, B., Somerville, T. D., Milazzo, J.
1165 P., Wilkinson, J. E., and Demerdash, O. E. (2018). POU2F3 is a master regulator of a tuft cell-
1166 like variant of small cell lung cancer. Genes & development *32*, 915-928.

1167 Jho, E.-h., Zhang, T., Domon, C., Joo, C.-K., Freund, J.-N., and Costantini, F. (2002). Wnt/β-
1168 catenin/Tcf signaling induces the transcription of Axin2, a negative regulator of the signaling
1169 pathway. Molecular and cellular biology *22*, 1172-1183.

1170 Jonkers, J., Meuwissen, R., van der Gulden, H., Peterse, H., van der Valk, M., and Berns, A.
1171 (2001). Synergistic tumor suppressor activity of BRCA2 and p53 in a conditional mouse model for
1172 breast cancer. Nature genetics *29*, 418.

1173 Juan, J., Muraguchi, T., Iezza, G., Sears, R. C., and McMahon, M. (2014). Diminished WNT ->
1174 beta-catenin -> c-MYC signaling is a barrier for malignant progression of BRAFV600E-induced
1175 lung tumors. Genes Dev *28*, 561-575.

1176 Kabiri, Z., Greicius, G., Zaribafzadeh, H., Hemmerich, A., Counter, C. M., and Virshup, D. M.
1177 (2018). Wnt signaling suppresses MAPK-driven proliferation of intestinal stem cells. Journal of
1178 Clinical Investigation *128*, 3806-3812.

1179 Kaji, I., and Kaunitz, J. D. (2017). Luminal chemosensing in the gastroduodenal mucosa. Current
1180 opinion in gastroenterology *33*, 439-445.

1181 Khunger, A., Khunger, M., and Velcheti, V. (2018). Dabrafenib in combination with trametinib in
1182 the treatment of patients with BRAF V600-positive advanced or metastatic non-small cell lung
1183 cancer: clinical evidence and experience. Therapeutic advances in respiratory disease *12*,
1184 1753466618767611.

1185 Kusakabe, T., Kawaguchi, A., Hoshi, N., Kawaguchi, R., Hoshi, S., and Kimura, S. (2006).
1186 Thyroid-specific enhancer-binding protein/NKX2. 1 is required for the maintenance of ordered
1187 architecture and function of the differentiated thyroid. Molecular endocrinology *20*, 1796-1809.

1188 Lavoie, J. N., L'Allemain, G., Brunet, A., Muller, R., and Pouyssegur, J. (1996). Cyclin D1
1189 expression is regulated positively by the p42/p44MAPK and negatively by the p38/HOGMAPK
1190 pathway. J Biol Chem *271*, 20608-20616.

1191 Lee, C.-L., Moding, E. J., Huang, X., Li, Y., Woodlief, L. Z., Rodrigues, R. C., Ma, Y., and Kirsch,
1192 D. G. (2012). Generation of primary tumors with Flp recombinase in FRT-flanked p53 mice.
1193 Disease models & mechanisms *5*, 397-402.

1194 Leushacke, M., Tan, S. H., Wong, A., Swathi, Y., Hajamohideen, A., Tan, L. T., Goh, J., Wong,
1195 E., Denil, S. L., and Murakami, K. (2017). Lgr5-expressing chief cells drive epithelial regeneration
1196 and cancer in the oxyntic stomach. Nature cell biology *19*, 774.

1197 Levin, P. A., Mayer, M., Hoskin, S., Sailors, J., Oliver, D. H., and Gerber, D. E. (2015). Histologic
1198 Transformation from Adenocarcinoma to Squamous Cell Carcinoma as a Mechanism of
1199 Resistance to EGFR Inhibition. J Thorac Oncol *10*, e86-e88.

1200 Levine, J. H., Simonds, E. F., Bendall, S. C., Davis, K. L., El-ad, D. A., Tadmor, M. D., Litvin, O.,
1201 Fienberg, H. G., Jager, A., and Zunder, E. R. (2015). Data-driven phenotypic dissection of AML
1202 reveals progenitor-like cells that correlate with prognosis. Cell *162*, 184-197.

1203 Liu, Y.-T., Dan, Q.-J., Wang, J., Feng, Y., Chen, L., Liang, J., Li, Q., Lin, S.-C., Wang, Z.-X., and
1204 Wu, J.-W. (2011). Molecular basis of Wnt activation via the DIX domain protein Ccd1. Journal of
1205 Biological Chemistry *286*, 8597-8608.

1206 Love, M. I., Huber, W., and Anders, S. (2014). Moderated estimation of fold change and dispersion
1207 for RNA-seq data with DESeq2. Genome biology *15*, 550.

1208 Ma, F., Ye, H., He, H. H., Gerrin, S. J., Chen, S., Tanenbaum, B. A., Cai, C., Sowalsky, A. G., He,
1209 L., and Wang, H. (2016). SOX9 drives WNT pathway activation in prostate cancer. The Journal
1210 of clinical investigation *126*, 1745-1758.

1211 Madisen, L., Zwingman, T. A., Sunkin, S. M., Oh, S. W., Zariwala, H. A., Gu, H., Ng, L. L., Palmiter,
1212 R. D., Hawrylycz, M. J., and Jones, A. R. (2010). A robust and high-throughput Cre reporting and
1213 characterization system for the whole mouse brain. Nature neuroscience *13*, 133.

1214 Maeda, Y., Tsuchiya, T., Hao, H., Tompkins, D. H., Xu, Y., Mucenski, M. L., Du, L., Keiser, A. R.,
1215 Fukazawa, T., and Naomoto, Y. (2012). Kras G12D and Nkx2-1 haploinsufficiency induce
1216 mucinous adenocarcinoma of the lung. The Journal of clinical investigation *122*, 4388-4400.

1217 McCracken, K. W., Aihara, E., Martin, B., Crawford, C. M., Broda, T., Treguier, J., Zhang, X.,
1218 Shannon, J. M., Montrose, M. H., and Wells, J. M. (2017). Wnt/β-catenin promotes gastric fundus
1219 specification in mice and humans. Nature *541*, 182.

1220 McFadden, D. G., Vernon, A., Santiago, P. M., Martinez-McFaline, R., Bhutkar, A., Crowley, D.
1221 M., McMahon, M., Sadow, P. M., and Jacks, T. (2014). p53 constrains progression to anaplastic
1222 thyroid carcinoma in a Braf-mutant mouse model of papillary thyroid cancer. Proceedings of the
1223 National Academy of Sciences *111*, E1600-E1609.

1224 McInnes, L., Healy, J., and Melville, J. (2018). Umap: Uniform manifold approximation and
1225 projection for dimension reduction. arXiv preprint arXiv:180203426.

1226 Mendoza, M. C., Er, E. E., and Blenis, J. (2011). The Ras-ERK and PI3K-mTOR pathways: cross-
1227 talk and compensation. Trends in biochemical sciences *36*, 320-328.

1228 Miyoshi, H., and Stappenbeck, T. S. (2013). In vitro expansion and genetic modification of
1229 gastrointestinal stem cells in spheroid culture. Nature protocols *8*, 2471.

1230 Mizuno, H., Nakanishi, Y., Ishii, N., Sarai, A., and Kitada, K. (2009). A signature-based method
1231 for indexing cell cycle phase distribution from microarray profiles. BMC genomics *10*, 137.

1232 Mollaoglu, G., Jones, A., Wait, S. J., Mukhopadhyay, A., Jeong, S., Arya, R., Camolotto, S. A.,
1233 Mosbruger, T. L., Stubben, C. J., and Conley, C. J. (2018). The lineage-defining transcription
1234 factors SOX2 and NKX2-1 determine lung cancer cell fate and shape the tumor immune
1235 microenvironment. Immunity *49*, 764-779. e769.

1236 Montoro, D. T., Haber, A. L., Biton, M., Vinarsky, V., Lin, B., Birket, S. E., Yuan, F., Chen, S.,
1237 Leung, H. M., and Villoria, J. (2018). A revised airway epithelial hierarchy includes CFTR-
1238 expressing ionocytes. Nature *560*, 319.

1239 Osaki, L., and Gama, P. (2013). MAPKs and signal transduction in the control of gastrointestinal
1240 epithelial cell proliferation and differentiation. International journal of molecular sciences *14*,
1241 10143-10161.

1242 Patra, K. C., Kato, Y., Mizukami, Y., Widholz, S., Boukhali, M., Revenco, I., Grossman, E. A., Ji,
1243 F., Sadreyev, R. I., Liss, A. S.*, et al.* (2018). Mutant GNAS drives pancreatic tumourigenesis by
1244 inducing PKA-mediated SIK suppression and reprogramming lipid metabolism. Nature cell
1245 biology *20*, 811-822.

1246 Patro, R., Duggal, G., Love, M. I., Irizarry, R. A., and Kingsford, C. (2017). Salmon provides fast
1247 and bias-aware quantification of transcript expression. Nature methods *14*, 417.

1248 Planchard, D., Besse, B., Groen, H. J., Souquet, P.-J., Quoix, E., Baik, C. S., Barlesi, F., Kim, T.
1249 M., Mazieres, J., and Novello, S. (2016). Dabrafenib plus trametinib in patients with previously
1250 treated BRAFV600E-mutant metastatic non-small cell lung cancer: an open-label, multicentre
1251 phase 2 trial. The Lancet Oncology *17*, 984-993.

1252 Planchard, D., Smit, E. F., Groen, H. J., Mazieres, J., Besse, B., Helland, Å., Giannone, V.,
1253 D'Amelio Jr, A. M., Zhang, P., and Mookerjee, B. (2017). Dabrafenib plus trametinib in patients

1254 with previously untreated BRAFV600E-mutant metastatic non-small-cell lung cancer: an open-
1255 label, phase 2 trial. The Lancet Oncology *18*, 1307-1316.

1256 Quante, M., Marrache, F., Goldenring, J. R., and Wang, T. C. (2010). TFF2 mRNA transcript
1257 expression marks a gland progenitor cell of the gastric oxyntic mucosa. Gastroenterology *139*,
1258 2018-2027. e2012.

1259 Ritterhouse, L. L., Vivero, M., Mino-Kenudson, M., Sholl, L. M., Iafrate, A. J., Nardi, V., and Dong,
1260 F. (2017). GNAS mutations in primary mucinous and non-mucinous lung adenocarcinomas. Mod
1261 Pathol *30*, 1720-1727.

1262 Robinson, J. T., Thorvaldsdóttir, H., Winckler, W., Guttman, M., Lander, E. S., Getz, G., and
1263 Mesirov, J. P. (2011). Integrative genomics viewer. Nature biotechnology *29*, 24.

1264 Robinson, M. D., McCarthy, D. J., and Smyth, G. K. (2010). edgeR: a Bioconductor package for
1265 differential expression analysis of digital gene expression data. Bioinformatics *26*, 139-140.

1266 Rotow, J., and Bivona, T. G. (2017). Understanding and targeting resistance mechanisms in
1267 NSCLC. Nature reviews Cancer *17*, 637-658.

1268 Roux, P. P., Shahbazian, D., Vu, H., Holz, M. K., Cohen, M. S., Taunton, J., Sonenberg, N., and
1269 Blenis, J. (2007). RAS/ERK signaling promotes site-specific ribosomal protein S6 phosphorylation
1270 via RSK and stimulates cap-dependent translation. Journal of Biological Chemistry *282*, 14056-
1271 14064.

1272 Ruscetti, M., Leibold, J., Bott, M. J., Fennell, M., Kulick, A., Salgado, N. R., Chen, C.-C., Ho, Y.-
1273 j., Sanchez-Rivera, F. J., and Feucht, J. (2018). NK cell–mediated cytotoxicity contributes to tumor
1274 control by a cytostatic drug combination. Science *362*, 1416-1422.

1275 Ruscetti, M., Morris IV, J. P., Mezzadra, R., Russell, J., Leibold, J., Romesser, P. B., Simon, J.,
1276 Kulick, A., Ho, Y.-j., and Fennell, M. (2020). Senescence-induced vascular remodeling creates
1277 therapeutic vulnerabilities in pancreas cancer. Cell.

1278 Russell, P. A., Wainer, Z., Wright, G. M., Daniels, M., Conron, M., and Williams, R. A. (2011).
1279 Does lung adenocarcinoma subtype predict patient survival?: A clinicopathologic study based on
1280 the new International Association for the Study of Lung Cancer/American Thoracic
1281 Society/European Respiratory Society international multidisciplinary lung adenocarcinoma
1282 classification. J Thorac Oncol *6*, 1496-1504.

1283 Sanchez-Danes, A., Larsimont, J. C., Liagre, M., Munoz-Couselo, E., Lapouge, G., Brisebarre,
1284 A., Dubois, C., Suppa, M., Sukumaran, V., Del Marmol, V.*, et al.* (2018). A slow-cycling LGR5
1285 tumour population mediates basal cell carcinoma relapse after therapy. Nature *562*, 434-438.

1286 Sato, T., Vries, R. G., Snippert, H. J., Van De Wetering, M., Barker, N., Stange, D. E., Van Es, J.
1287 H., Abo, A., Kujala, P., and Peters, P. J. (2009). Single Lgr5 stem cells build crypt–villus structures
1288 in vitro without a mesenchymal niche. Nature *459*, 262.

1289 Schönhuber, N., Seidler, B., Schuck, K., Veltkamp, C., Schachtler, C., Zukowska, M., Eser, S.,
1290 Feyerabend, T. B., Paul, M. C., and Eser, P. (2014). A next-generation dual-recombinase system
1291 for time-and host-specific targeting of pancreatic cancer. Nature medicine *20*, 1340.

1292 Shai, A., Dankort, D., Juan, J., Green, S., and McMahon, M. (2015). TP53 silencing bypasses
1293 growth arrest of BRAFV600E-induced lung tumor cells in a two-switch model of lung
1294 tumorigenesis. Cancer research *75*, 3167-3180.

1295 Shaw, A. T., Meissner, A., Dowdle, J. A., Crowley, D., Magendantz, M., Ouyang, C., Parisi, T.,
1296 Rajagopal, J., Blank, L. J., Bronson, R. T.*, et al.* (2007). Sprouty-2 regulates oncogenic K-ras in
1297 lung development and tumorigenesis. Genes Dev *21*, 694-707.

1298 Skoulidis, F., Byers, L. A., Diao, L., Papadimitrakopoulou, V. A., Tong, P., Izzo, J., Behrens, C.,
1299 Kadara, H., Parra, E. R., Canales, J. R.*, et al.* (2015). Co-occurring genomic alterations define
1300 major subsets of KRAS-mutant lung adenocarcinoma with distinct biology, immune profiles, and
1301 therapeutic vulnerabilities. Cancer Discov *5*, 860-877.

1302 Skoulidis, F., and Heymach, J. V. (2019). Co-occurring genomic alterations in non-small-cell lung
1303 cancer biology and therapy. Nat Rev Cancer *19*, 495-509.

1304 Snyder, E. L., Watanabe, H., Magendantz, M., Hoersch, S., Chen, T. A., Wang, D. G., Crowley,
1305 D., Whittaker, C. A., Meyerson, M., and Kimura, S. (2013). Nkx2-1 represses a latent gastric
1306 differentiation program in lung adenocarcinoma. Molecular cell *50*, 185-199.

1307 Soneson, C., Love, M. I., and Robinson, M. D. (2015). Differential analyses for RNA-seq:
1308 transcript-level estimates improve gene-level inferences. F1000Research *4*.

1309 Stuart, T., Butler, A., Hoffman, P., Hafemeister, C., Papalexi, E., Mauck III, W. M., Hao, Y.,
1310 Stoeckius, M., Smibert, P., and Satija, R. (2019). Comprehensive Integration of Single-Cell Data.
1311 Cell.

1312 Taki, K., Ohmuraya, M., Tanji, E., Komatsu, H., Hashimoto, D., Semba, K., Araki, K., Kawaguchi,
1313 Y., Baba, H., and Furukawa, T. (2016). GNAS(R201H) and Kras(G12D) cooperate to promote
1314 murine pancreatic tumorigenesis recapitulating human intraductal papillary mucinous neoplasm.
1315 Oncogene *35*, 2407-2412.

1316 Tammela, T., Sanchez-Rivera, F. J., Cetinbas, N. M., Wu, K., Joshi, N. S., Helenius, K., Park, Y.,
1317 Azimi, R., Kerper, N. R., and Wesselhoeft, R. A. (2017). A Wnt-producing niche drives proliferative
1318 potential and progression in lung adenocarcinoma. Nature *545*, 355.

1319 Taylor, S. S., Kim, C., Cheng, C. Y., Brown, S. H., Wu, J., and Kannan, N. (2008). Signaling
1320 through cAMP and cAMP-dependent protein kinase: diverse strategies for drug design. Biochim
1321 Biophys Acta *1784*, 16-26.

1322 Ting, H.-A., and von Moltke, J. (2019). The immune function of tuft cells at gut mucosal surfaces
1323 and beyond. The Journal of Immunology *202*, 1321-1329.

1324 Tirosh, I., Izar, B., Prakadan, S. M., Wadsworth, M. H., Treacy, D., Trombetta, J. J., Rotem, A.,
1325 Rodman, C., Lian, C., and Murphy, G. (2016). Dissecting the multicellular ecosystem of metastatic
1326 melanoma by single-cell RNA-seq. Science *352*, 189-196.

1327 Travis, W. D., Brambilla, E., Noguchi, M., Nicholson, A. G., Geisinger, K., Yatabe, Y., Powell, C.
1328 A., Beer, D., Riely, G., Garg, K.*, et al.* (2011). International Association for the Study of Lung
1329 Cancer/American Thoracic Society/European Respiratory Society: international multidisciplinary
1330 classification of lung adenocarcinoma: executive summary. Proceedings of the American
1331 Thoracic Society *8*, 381-385.

1332 Trejo, C. L., Juan, J., Vicent, S., Sweet-Cordero, A., and McMahon, M. (2012). MEK1/2 inhibition
1333 elicits regression of autochthonous lung tumors induced by KRASG12D or BRAFV600E. Cancer
1334 research *72*, 3048-3059.

1335 Tsai, J., Lee, J. T., Wang, W., Zhang, J., Cho, H., Mamo, S., Bremer, R., Gillette, S., Kong, J.,
1336 and Haass, N. K. (2008). Discovery of a selective inhibitor of oncogenic B-Raf kinase with potent
1337 antimelanoma activity. Proceedings of the National Academy of Sciences *105*, 3041-3046.

1338 Tuveson, D. A., Shaw, A. T., Willis, N. A., Silver, D. P., Jackson, E. L., Chang, S., Mercer, K. L.,
1339 Grochow, R., Hock, H., and Crowley, D. (2004). Endogenous oncogenic K-rasG12D stimulates
1340 proliferation and widespread neoplastic and developmental defects. Cancer cell *5*, 375-387.

1341 Vallone, V. F., Leprovots, M., Strollo, S., Vasile, G., Lefort, A., Libert, F., Vassart, G., and Garcia,
1342 M.-I. (2016). Trop2 marks transient gastric fetal epithelium and adult regenerating cells after
1343 epithelial damage. Development *143*, 1452-1463.

1344 VanDussen, K. L., Marinshaw, J. M., Shaikh, N., Miyoshi, H., Moon, C., Tarr, P. I., Ciorba, M. A.,
1345 and Stappenbeck, T. S. (2015). Development of an enhanced human gastrointestinal epithelial
1346 culture system to facilitate patient-based assays. Gut *64*, 911-920.

1347 Winslow, M. M., Dayton, T. L., Verhaak, R. G., Kim-Kiselak, C., Snyder, E. L., Feldser, D. M.,
1348 Hubbard, D. D., DuPage, M. J., Whittaker, C. A., and Hoersch, S. (2011). Suppression of lung
1349 adenocarcinoma progression by Nkx2-1. Nature *473*, 101.

1350 Xu, C., and Su, Z. (2015). Identification of cell types from single-cell transcriptomes using a novel
1351 clustering method. Bioinformatics *31*, 1974-1980.

1352 Young, N. P., Crowley, D., and Jacks, T. (2011). Uncoupling cancer mutations reveals critical
1353 timing of p53 loss in sarcomagenesis. Cancer research *71*, 4040-4047.

1354 Zhan, T., Ambrosi, G., Wandmacher, A. M., Rauscher, B., Betge, J., Rindtorff, N., Häussler, R.
1355 S., Hinsenkamp, I., Bamberg, L., and Hessling, B. (2019). MEK inhibitors activate Wnt signalling
1356 and induce stem cell plasticity in colorectal cancer. Nature communications *10*, 1-17.

1357 Zhan, T., Rindtorff, N., and Boutros, M. (2017). Wnt signaling in cancer. Oncogene *36*, 1461-
1358 1473.

1359 Zhang, P., Yang, M., Zhang, Y., Xiao, S., Lai, X., Tan, A., Du, S., and Li, S. (2019). Dissecting
1360 the Single-Cell Transcriptome Network Underlying Gastric Premalignant Lesions and Early
1361 Gastric Cancer. Cell reports *27*, 1934-1947. e1935.

1362 Zhang, Y., Wang, R., Li, Y., Pan, Y., Hu, H., Zhang, Y., Li, H., Shen, L., Yu, Y., Sun, Y., and Chen,
1363 H. (2015). Negative Thyroid Transcription Factor 1 Expression Defines an Unfavorable Subgroup
1364 of Lung Adenocarcinomas. Journal of Thoracic Oncology *10*, 1444-1450.
1365
1366
1367

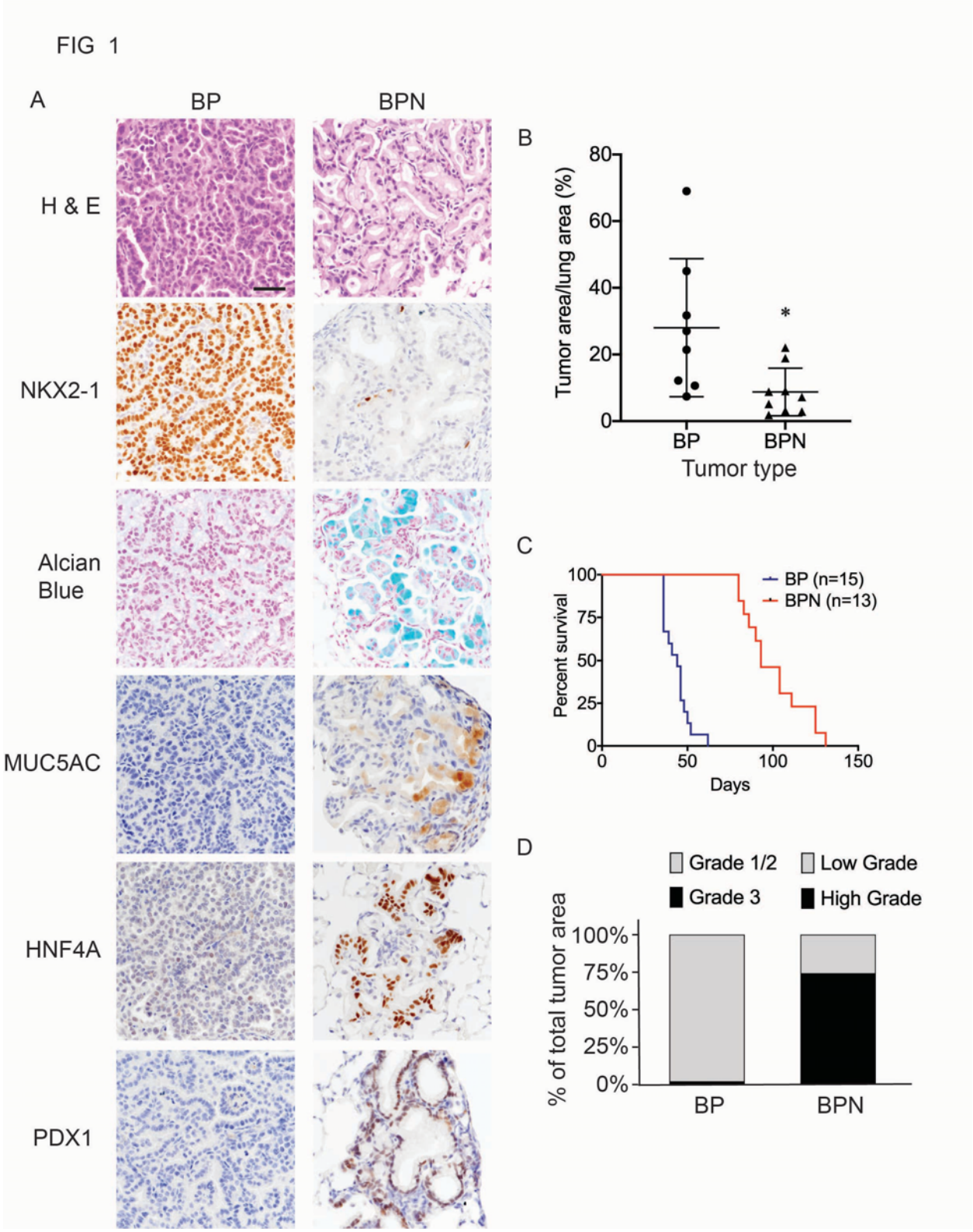
FIG 1
A
BP
BPN
H & E
NKX2-1
Alcian Blue
MUC5AC
HNF4A
PDX1
B
Tumor area/lung area (%)
80
60
40
20
0
*
BP
BPN
Tumor type
C
Percent survival
100
75
50
25
0
0
50
100
150
Days
BP (n=15)
BPN (n=13)
D
Grade 1/2
Low Grade
Grade 3
High Grade
% of total tumor area
100%
75%
50%
25%
0%
BP
BPN

1368

Suppl FIG S1

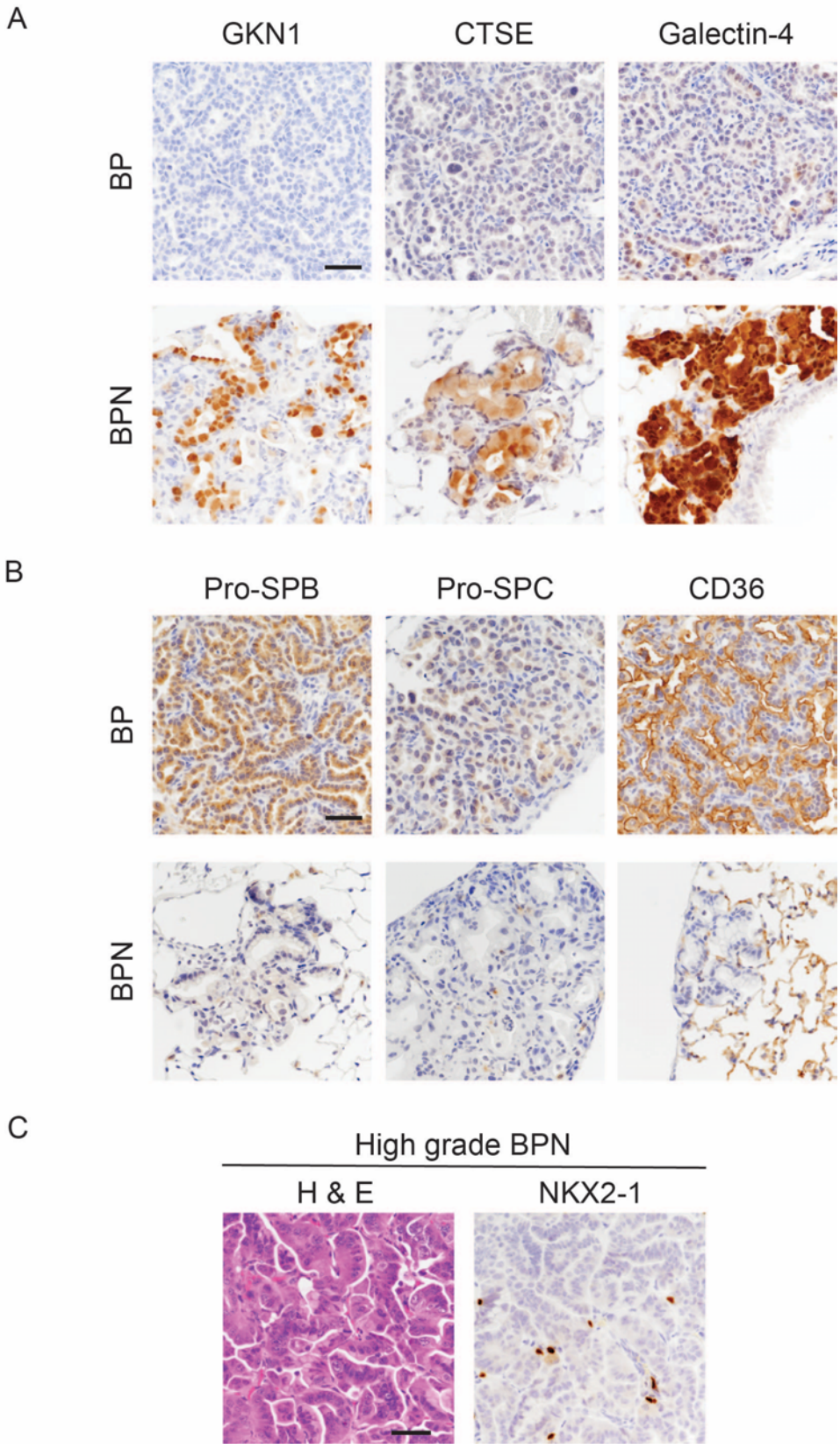

1369

1370 **Figure 1. *Nkx2-1* deletion induces mucinous adenocarcinoma but impairs tumor**
1371 **initiation in BRAF^{V600E}-driven lung adenocarcinoma.**
1372 (A) Representative photomicrographs of lung neoplasia arising 8 weeks after initiation
1373 with PGK-Cre lentivirus (5x10^3 pfu/mouse). BP mice are *BRaf$^{CA/+}$;Trp53$^{f/f}$;Nkx2-*
1374 *1$^{f/+}$;Rosa26$^{tdTomato/tdTomato}$*. BPN mice are *BRaf$^{CA/+}$;Trp53$^{f/f}$;Nkx2-1$^{f/f}$;Rosa26$^{tdTomato/tdTomato}$*.
1375 Hematoxylin and eosin (H&E), Alcian blue stain for mucin production, and
1376 immunohistochemistry (IHC) for NKX2-1, plus, markers of gastrointestinal differentiation.
1377 Scale bar: 100 μm. (B) Quantitation of lung tumor burden 8 weeks after initiation with
1378 PGK-Cre lentivirus (5x10^3 pfu/mouse) in indicated genotypes of mice: BP (n=8), BPN
1379 (n=9). *P=0.019 by Student's t-test. (C) Long-term survival after tumor initiation with Ad5-
1380 CMV-Cre adenovirus (2.5x10^7 pfu/mouse) in mice of indicated genotypes. P< 0.0001 by
1381 Log-rank test. (D) Histopathologic assessment of the percentage of tumors of indicated
1382 grade for mice enrolled in survival study (C).
1383
1384 The following figure supplement is available for figure 1:
1385
1386 **Figure S1. *Nkx2-1* deletion induces mucinous adenocarcinoma but impairs tumor**
1387 **initiation in BRAF^{V600E}-driven lung adenocarcinoma.**
1388 (A, B) Histologic phenotype of lung neoplasia arising 8 weeks after initiation with PGK-
1389 Cre lentivirus (5x10^3 pfu/mouse) in *BRaf$^{CA/+}$;Trp53$^{f/f}$;Nkx2-1$^{f/+}$;Rosa26$^{tdTomato/tdTomato}$* (BP)
1390 and *BRaf$^{CA/+}$;Trp53$^{f/f}$;Nkx2-1$^{f/f}$;Rosa26$^{tdTomato/tdTomato}$* (BPN) mice. Immunostaining for
1391 markers of gastrointestinal (A) and pulmonary (B) differentiation. (C) H&E and NKX2-1
1392 IHC of a representative high grade BPN lung tumor. Scale bar: 100 μm.

FIG 2

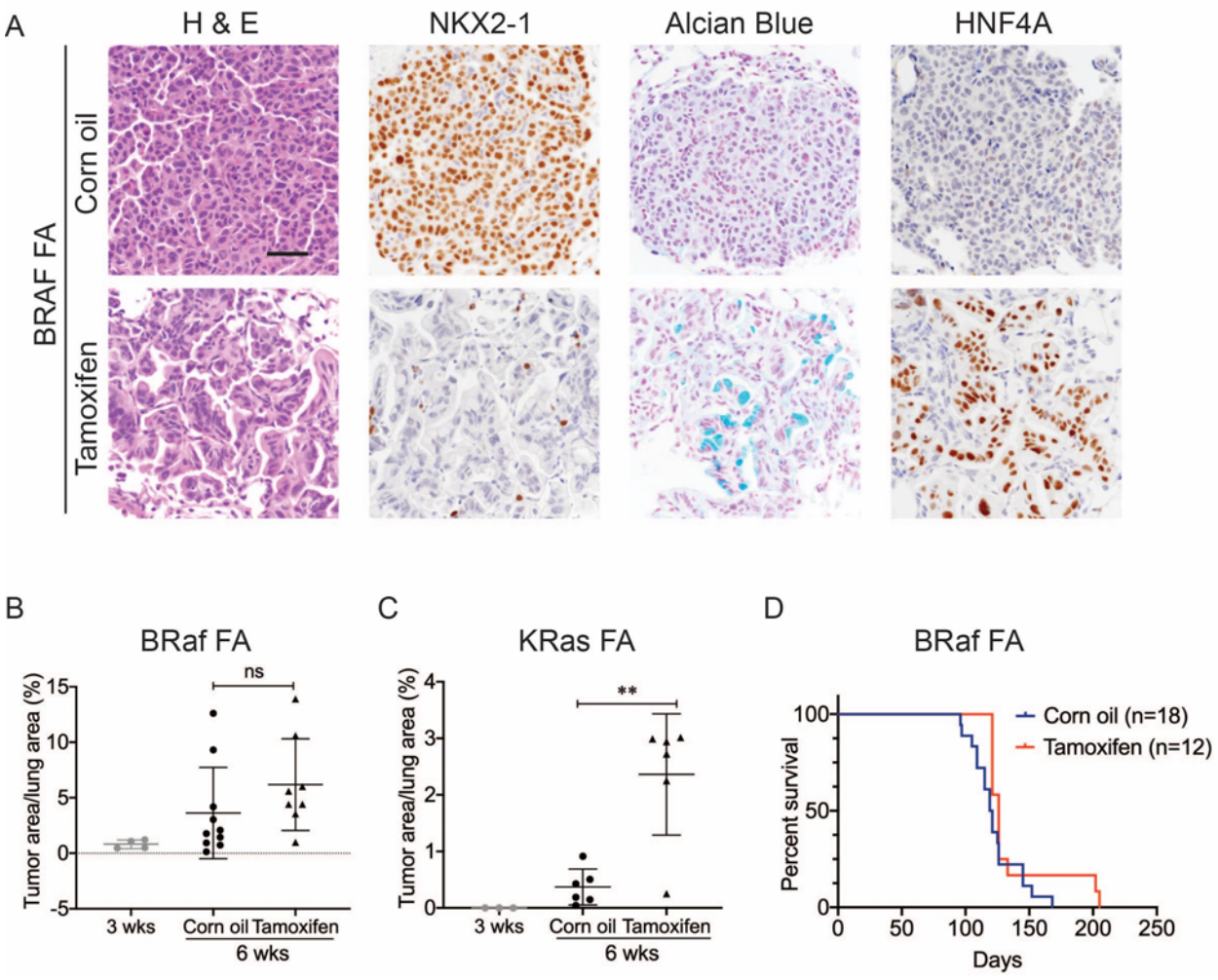

1393

1394

1395

Suppl FIG 2

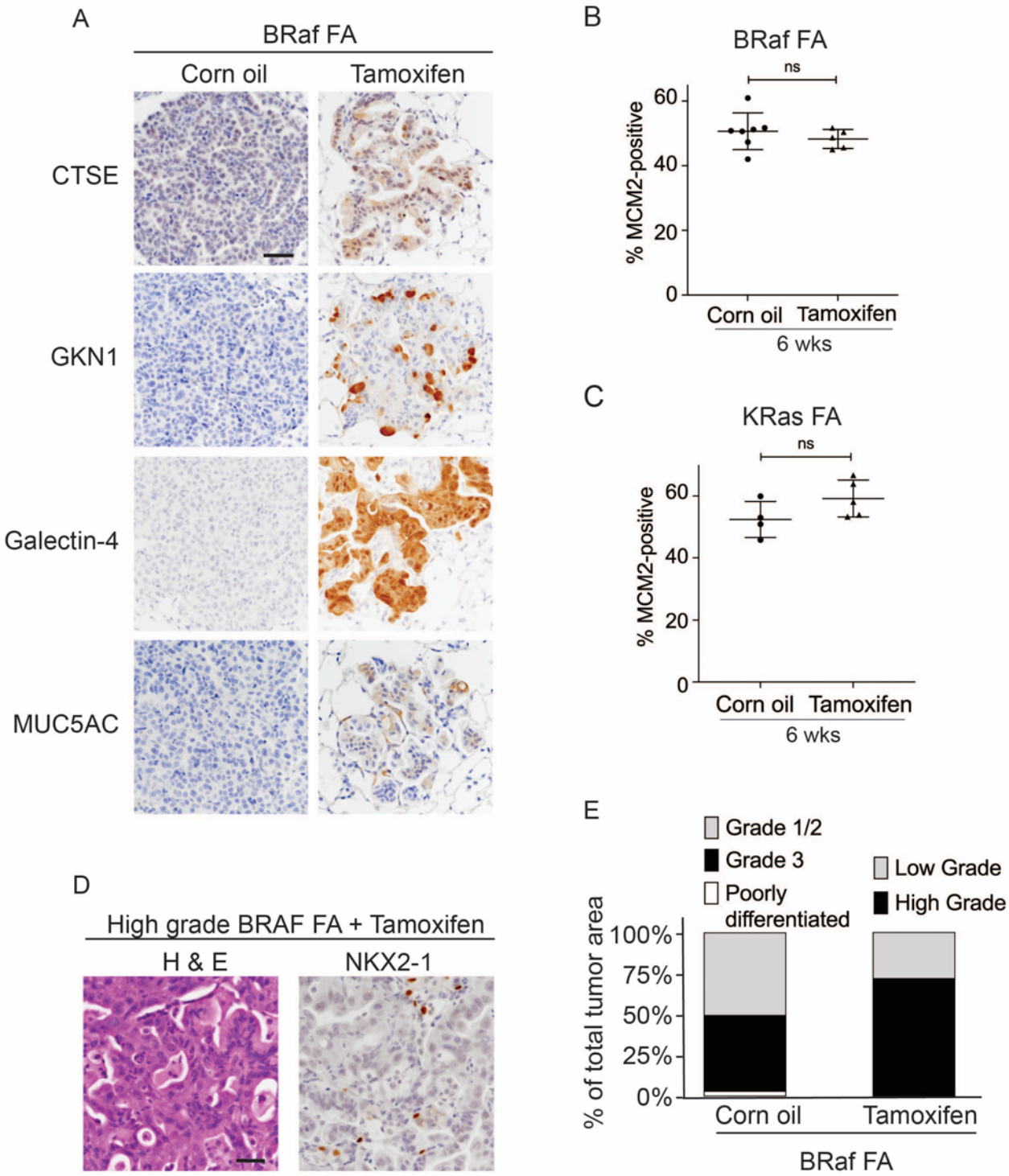

1396

1397

1398

1399 **Figure 2. *Nkx2-1* deletion in established BRAF-mutant LUAD induces mucinous**
1400 **adenocarcinoma without altering tumor growth.**
1401 (A, B) All mice are *BRaf*$^{FA/+}$;*Trp53*$^{frt/frt}$;*Nkx2-1*$^{f/f}$;*Rosa26*$^{CreERT2/CreERT2}$. Viral FlpO-
1402 recombinase expression simultaneously activated BRAF^{V600E} and Cre^{ERT2} and deleted
1403 *Trp53* by excision of *Frt* sites. 3 weeks post-tumor initiation, mice were injected with corn
1404 oil (as vehicle control) or with tamoxifen to recombine *LoxP*-sites within *Nkx2-1* alleles by
1405 Cre^{ERT2} recombinase. Lungs were harvested 3 weeks thereafter. (A) H&E, Alcian blue,
1406 NKX2-1 and HNF4A staining of lung neoplasia arising 6 weeks after initiation with Ad-
1407 FlpO adenovirus (2x10^{7} pfu/mouse). Scale bar: 100 μm. (B) Quantitation of tumor burden
1408 at 3 weeks (n=4 mice), and at 6 weeks after initiation, following corn oil treatment (n=10
1409 mice) or tamoxifen injections (n=8 mice). Tamoxifen administration consisted of 6
1410 intraperitoneal doses over 9 days. Graphs represent mean ± S.D. *P* values are not
1411 statistically significant. (C) Mice are *KRas*$^{FSF-G12D/+}$;*Trp53*$^{frt/frt}$;*Nkx2-1*$^{f/f}$;*Rosa26*$^{FSF-}$
1412 $^{CreERT2/CreERT2}$ and were administered with corn oil (n=6 mice) or tamoxifen (n=6 mice)
1413 injections as described in (B). Shown is the quantitation of tumor burden at 3 weeks and
1414 at 6 weeks post-initiation. Graphs represent mean ± S.D. ***P*=0.0014 by Student's *t*-test.
1415 (D) Survival of *BRaf*$^{FA/+}$;*Trp53*$^{frt/frt}$;*Nkx2-1*$^{f/f}$;*Rosa26*$^{FSF-CreERT2/CreERT2}$ mice that were
1416 treated with tamoxifen or vehicle starting at 3 weeks following tumor initiation. Tamoxifen
1417 administration consisted of 6 intraperitoneal doses over 9 days, followed by tamoxifen-
1418 containing chow for 1 month.
1419
1420 The following figure supplement is available for figure 2:
1421

1422 **Figure S2. *Nkx2-1* deletion in established BRAF-mutant LUAD induces mucinous**
1423 **adenocarcinoma without altering tumor growth.**
1424 (A) Immunostaining for indicated mucin/gastric markers in NKX2-1-positive and -negative
1425 LUADs. Lung tumor sections were obtained from corn oil or tamoxifen treated
1426 *BRaf*$^{FA/+}$;*Trp53*$^{frt/frt}$;*Nkx2-1*$^{f/f}$;*Rosa26*$^{FSF\text{-}CreERT2/CreERT2}$ mice 6 weeks post-initiation with Ad-
1427 FlpO adenovirus (2x10^{7} pfu/mouse). Scale bar: 100 μm. (B, C) Quantitation of MCM2-
1428 positive cells in lung tumors at 6 weeks after initiation, and following corn oil/tamoxifen
1429 injections at 3 weeks. Lung neoplasia was initiated with Ad-FlpO adenovirus (2x10^{7}
1430 pfu/mouse) in *BRaf*$^{FA/+}$;*Trp53*$^{frt/frt}$;*Nkx2-1*$^{f/f}$;*Rosa26*$^{FSF\text{-}CreERT2/CreERT2}$ and *KRas*$^{frtSfrt\text{-}}$
1431 $^{G12D/+}$;*Trp53*$^{frt/frt}$;*Nkx2-1*$^{f/f}$;*Rosa26*$^{FSF\text{-}CreERT2/CreERT2}$ mice. Graphs represent mean ± S.D.
1432 Multiple tumors in *BRaf*^{FA} oil (n=7 mice); tamoxifen administered (n=5 mice); *KRas*^{FA} oil
1433 (n=4 mice) and tamoxifen administered (n=5 mice) were analyzed. (D) Representative
1434 images of high grade tumors obtained from a BRaf FA mouse that had received tamoxifen
1435 injections. Scale bar: 100 μm. (E) Grades for individual tumors based on criteria described
1436 for Fig. 1d. Histopathologic assessment was performed for mice enrolled in survival study
1437 (Fig. 2d).

FIG 3

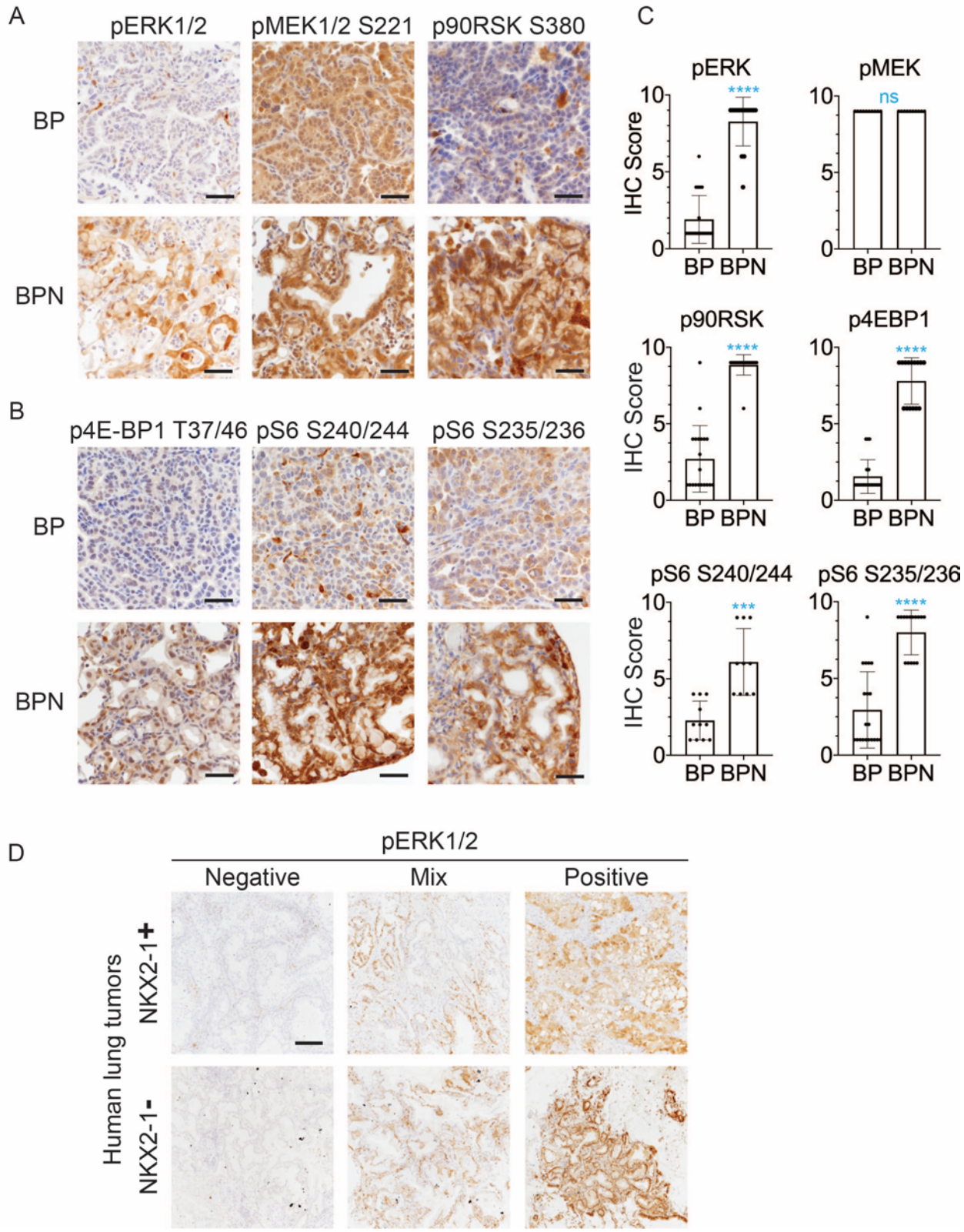

1438

1439

Suppl FIG 3

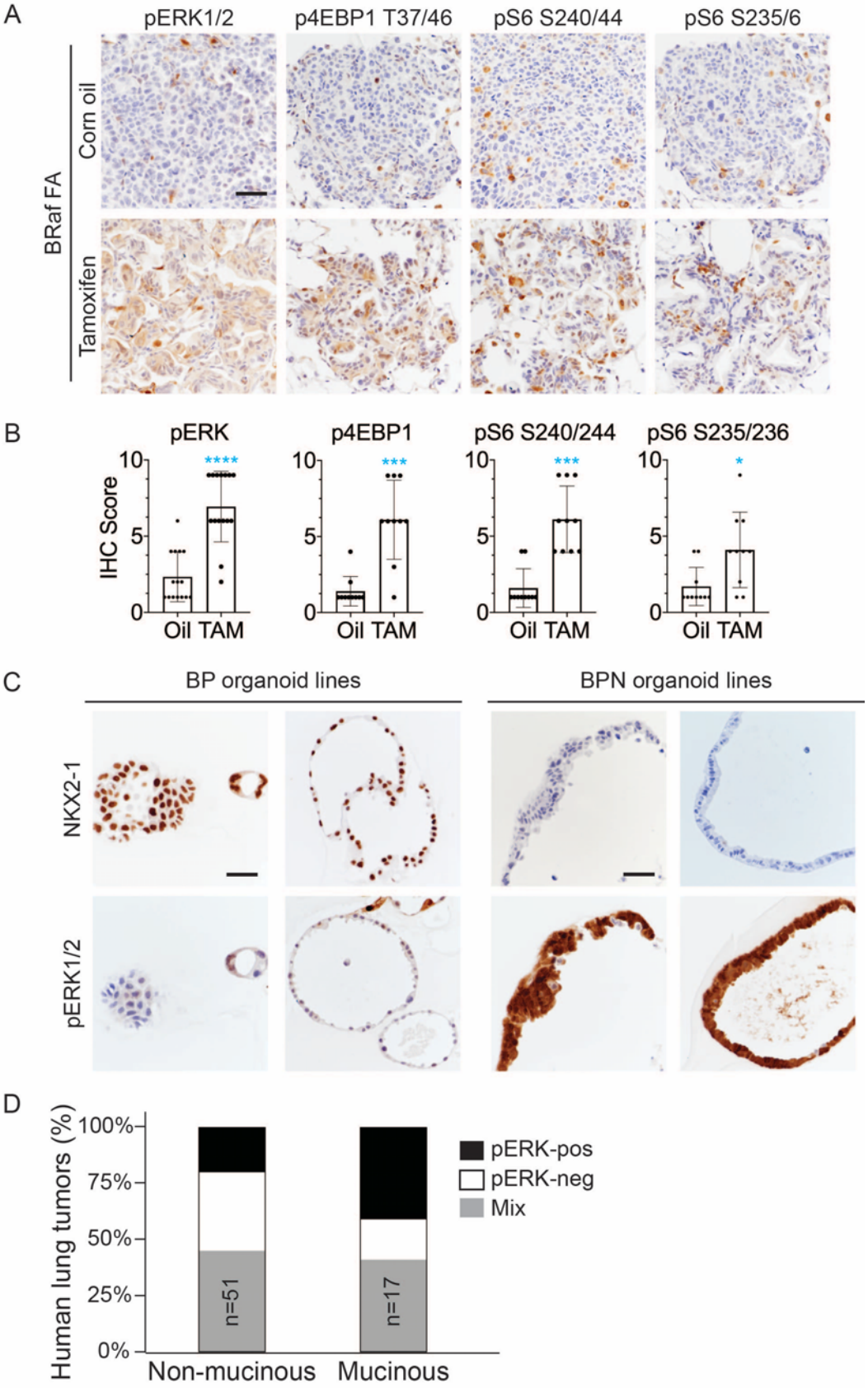

1440

1441

1442 **Figure 3. NKX2-1 regulates MAPK pathway in BRAF^{V600E}-driven LUAD.**

1443 (A, B) IHC for indicated proteins in lung neoplasia present at 8 weeks post-initiation in
1444 *BRaf$^{CA/+}$;Trp53$^{f/f}$;Nkx2-1$^{f/+}$;Rosa26$^{tdTomato/tdTomato}$* and *BRaf$^{CA/+}$;Trp53$^{f/f}$;Nkx2-*
1445 *1$^{f/f}$;Rosa26$^{tdTomato/tdTomato}$* mice. (C) IHC quantitation of phosphoproteins in indicated tumor
1446 types (n=2-4 mice/genotype). Each dot represents one tumor. Error bars indicate mean
1447 ± S.D. ****P<0.0001, ***P<0.001, ns= not significant by Mann-Whitney test. (D)
1448 Representative staining of phospho-ERK in human non-mucinous (NKX2-1-positive,
1449 n=51) and mucinous (NKX2-1-negative, n=17) lung tumors. Scale bar: 500 μm.

1450

1451 The following figure supplement is available for figure 3:

1452

1453 **Figure S3: NKX2-1 regulates MAPK pathway in BRAF^{V600E}-driven LUAD.**

1454 (A) IHC for indicated phospho-proteins in NKX2-1-positive and -negative LUADs. Lung
1455 tumor sections were obtained from corn oil or tamoxifen treated *BRaf$^{FA/+}$;Trp53$^{frt/frt}$;Nkx2-*
1456 *1$^{f/f}$;Rosa26$^{FSF\text{-}CreERT2/CreERT2}$* mice 6 weeks post-initiation with Ad-FlpO. (B) IHC
1457 quantitation of phosphoproteins in indicated tumor types. Error bars indicate mean ± S.D.
1458 ****P< 0.0001, ***P<0.001, *P<0.05 by Mann-Whitney test. At least 10 tumors across 2-
1459 3 mice were analyzed. (C) Long-term 3D cultures of primary mouse LUAD cells isolated
1460 from *BRaf$^{CA/+}$;Trp53$^{f/f}$;Nkx2-1$^{f/+}$;Rosa26$^{tdTomato/tdTomato}$* (BP) and *BRaf$^{CA/+}$;Trp53$^{f/f}$;Nkx2-*
1461 *1$^{f/f}$;Rosa26$^{tdTomato/tdTomato}$* (BPN) mice 8 weeks post-initiation. Shown are representative
1462 IHC photomicrographs. Scale bar: 100 μm. (D) Quantitation of phospho-ERK levels in
1463 human lung tumors relative to NKX2-1 expression/histologic subtype.

FIG 4

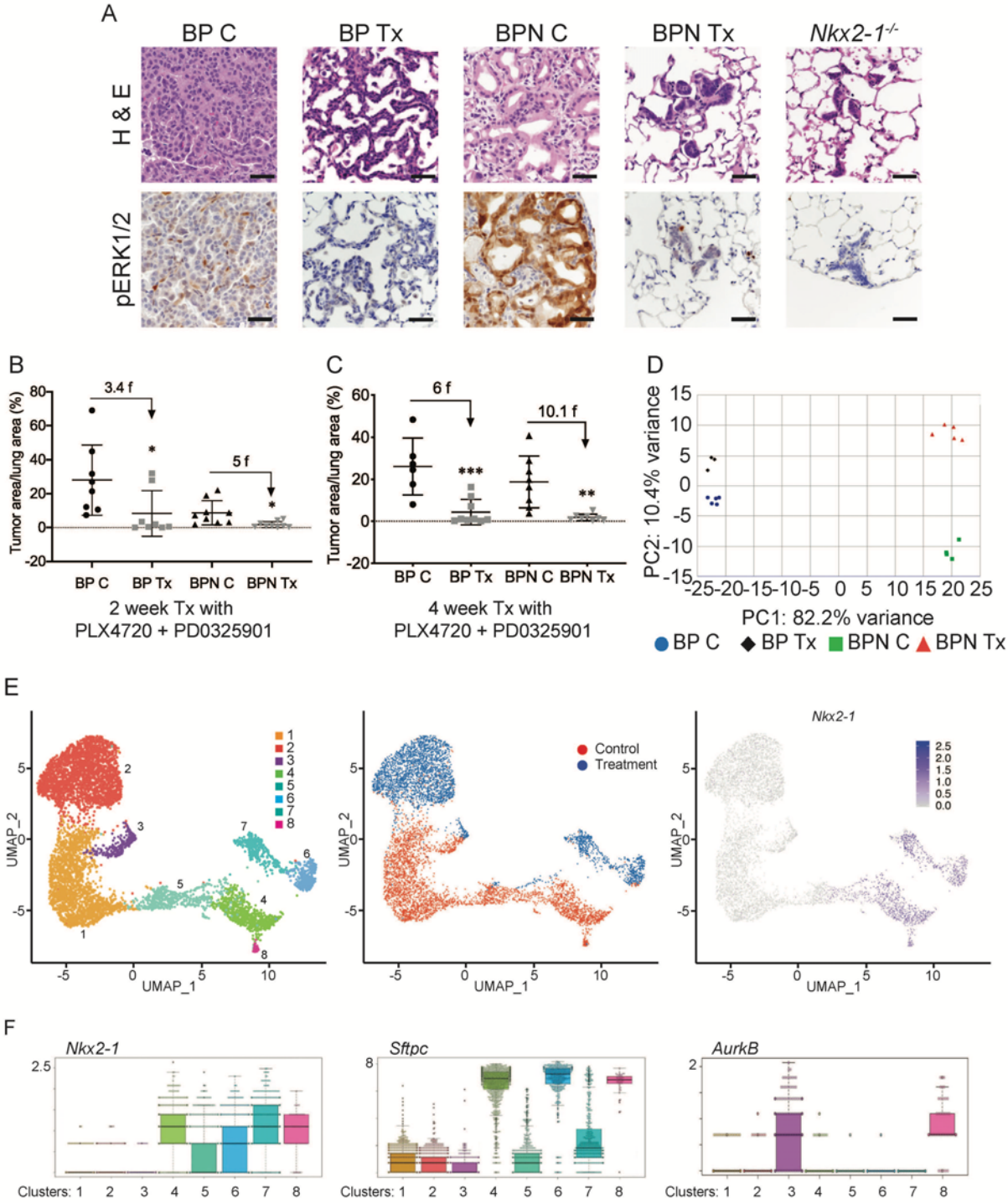

1464

1465

Suppl FIG 4

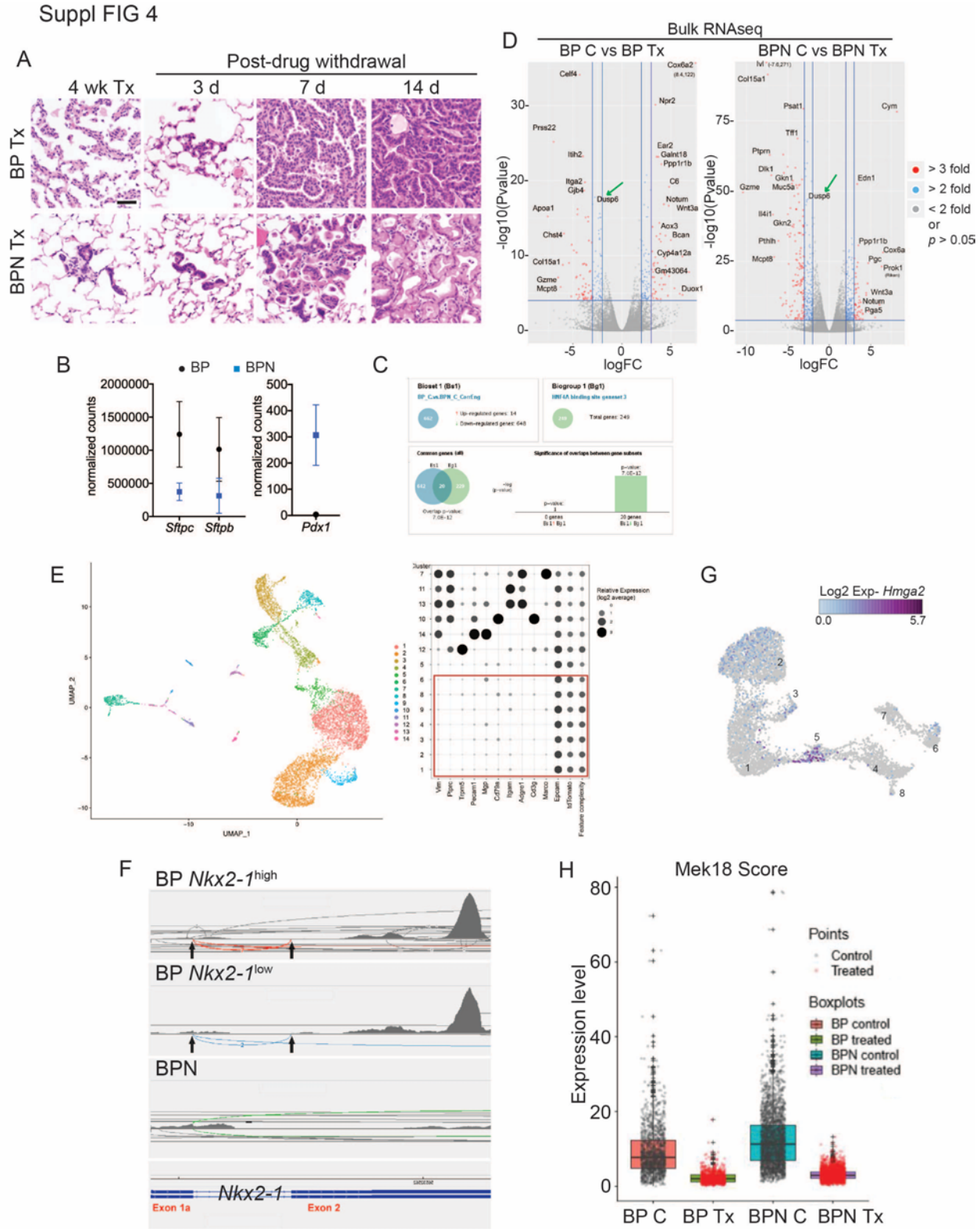

1466

1467

1468

1469 **Figure 4. NKX2-1 status modulates response to MAPK pathway inhibitors.**

1470 (A) Representative H&E and phospho-ERK1/2 immunostaining photomicrographs of
1471 paraffin-embedded lung sections from *BRaf*$^{CA/+}$*;Trp53*$^{f/f}$*;Nkx2-1*$^{f/+}$*;Rosa26*$^{tdTomato/tdTomato}$
1472 and *BRaf*$^{CA/+}$*;Trp53*$^{f/f}$*;Nkx2-1*$^{f/f}$*;Rosa26*$^{tdTomato/tdTomato}$ mice that were treated with control
1473 chow (BP C/BPN C) or chow containing PLX4720 (200 mg/kg) and PD0325901 (7 mg/kg)
1474 inhibitors (BP Tx/BPN Tx) for two weeks starting at 6 weeks post-tumor initiation with
1475 PGK-Cre lentivirus (5x10^3 pfu/mouse). Scale bar: 100 μm. (B, C) Quantitation of tumor
1476 burden in BP and BPN mice that were fed control chow or chow containing MAPK
1477 inhibitors starting at 6 weeks post-tumor initiation with PGK-Cre lentivirus (5x10^3
1478 pfu/mouse). Graphs represent mean ± S.D. (B) Chow treatment lasted 2 weeks and lungs
1479 were harvested at the 8 week timepoint. BP C (n=8), BP Tx (n=8), BPN C (n=9), BPN Tx
1480 (n=9). *P<0.05 by Student's t-test. Numbers indicated above graphs represent the fold
1481 reduction in tumor burden upon inhibitor-chow administration. (C) Chow treatment lasted
1482 4 weeks and lungs were harvested at the 10 week timepoint. BP C (n=6), BP Tx (n=9),
1483 BPN C (n=8), BPN Tx (n=8). **P<0.01, ***P<0.001. Numbers indicated above graphs
1484 represent the fold reduction in tumor burden with inhibitor-chow administration. (D) Global
1485 gene expression analyses were performed on RNAs from FACS-sorted tdTomato$^+$ BP C
1486 (n=5), BP Tx (n=3), BPN C (n=4) and BPN Tx (n=5) murine lung tumor cells isolated at 7
1487 weeks following initiation with Ad5-Spc-Cre adenovirus (5x10^8 pfu/mouse for BP and
1488 8x10^8 pfu/mouse for BPN mice). Control and MAPK-inhibitor chow treatments were given
1489 for 1 week at 6 weeks post-adenoviral instillation. Shown is the principal-component
1490 analysis (PCA) plot of the top 500 most variable genes showing that the four experimental
1491 groups of lung tumors, BP C, BP Tx, BPN C and BPN Tx, had distinct global patterns of

1492 gene expression. (E) UMAP plots showing relatedness of high quality, tumor cell scRNA-
1493 seq profiles from BPN control (n=2) and BPN MAPKi-treated (n=2) mice. Tumor cluster
1494 designations are indicated (left). Control and treated cells indicated (middle). *Nkx2-1*
1495 expression in scRNA-seq data indicating that clusters 4-8 represent incomplete
1496 recombinants (right). Single tumor cells were obtained by FACS-sorting tdTomato^{+} cells
1497 isolated at 7 weeks following initiation with Ad5-Spc-Cre adenovirus ($8x10^{8}$ pfu/mouse).
1498 Control and MAPK-inhibitor chow treatments were given for 1 week at 6 weeks post-
1499 adenoviral instillation. (F) Beeswarm plots of single cell sequencing data showing
1500 expression levels of *Nkx2-1*, *Sftpc* and *AurkB* transcripts in tumor clusters 1-8.
1501
1502 The following figure supplement is available for figure 4:
1503
1504 **Figure S4. NKX2-1 status modulates response to MAPK pathway inhibitors.**
1505 (A) Representative histology of BP and BPN tumors after 4 weeks of combined BRAF^{V600E}
1506 and MEK inhibitor chow treatment, as well as at different timepoints following drug
1507 withdrawal demonstrating rapid tumor relapse. (B) Graphs comparing absolute
1508 expression levels of direct NKX2-1 targets (*Sftpc* and *Sftpb*) as well as the gastrointestinal
1509 marker *Pdx1* in BP (n=8) and BPN (n=9) tumors, data obtained from bulk RNA
1510 sequencing. (C) Bulk RNAseq analyses of BP and BPN tumors via Illumina Correlation
1511 Engine indicating that HNF4α binding site geneset 3 becomes significantly enriched upon
1512 loss of *Nkx2-1*. (D) Volcano plots of bulk RNA sequencing data from control and MAPK
1513 inhibitor-treated BP tumors (left) and BPN tumors (right) indicating differentially expressed
1514 genes (EdgeR) (see also Supplementary Tables 2, 3). Select highly differentially

1515 expressed genes are highlighted. (E) Left- UMAP visualization of single cell transcriptome
1516 relatedness indicating 14 distinct clusters. Right- Relative expression of stromal marker
1517 genes and feature complexity score used in selecting high complexity tumor clusters that
1518 lack stromal marker gene expression for further analysis (red box). * Lower than average
1519 complexity. (F) Sashimi plots visualizing raw RNAseq densities along *Nkx2-1* exons and
1520 splice junction for *Nkx2-1*-positive and *Nkx2-1*-negative single tumor cells from their
1521 alignment data. Exon 1a-2 junctions and exon 2 reads are only detected in cells
1522 expressing *Nkx2-1* to variable degree indicating that these are incomplete recombinants
1523 (BP cells). (G) UMAP visualization of *Hmga2* expression in tumor clusters 1-8. (H)
1524 Quantitation of MAPK activation levels in single cell RNA sequencing data using Mek18
1525 transcriptional signature (Dry et al., 2010). BP indicates cells from clusters 4-8; BPN
1526 indicates cells from clusters 1-3 (see Fig. 4e-f). C: control, Tx= drug treatment.

FIG 5

A

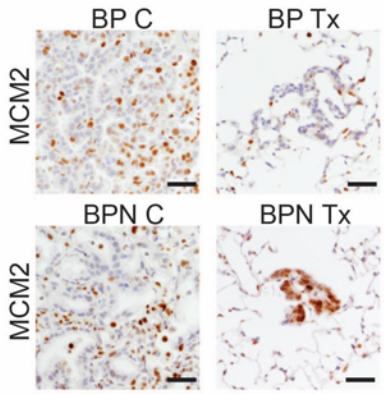

C

BP C vs BP Tx: Gene Ontology analysis by Illumina Correlation Engine				
BIOGROUP NAME	SCORE	COMMON GENES	DIRECTION	P-VALUE
cell division	105.76	41	up	1.20E-46
mitosis	104.37	36	up	4.70E-46
nuclear division	104.37	36	up	4.70E-46
kinetochore	51.24	16	up	5.60E-23
spindle	49.21	17	up	4.30E-22

D

BPN C vs BPN Tx: Gene Ontology analysis by Illumina Correlation Engine				
BIOGROUP NAME	SCORE	COMMON GENES	DIRECTION	P-VALUE
extracellular matrix	46.96	24	up	4.00E-21
proteinaceous extracellular matrix	46.76	23	up	4.90E-21
vascular development	23.87	16	up	4.30E-11
tissue morphogenesis	23.28	16	up	7.70E-11
regulation of vascular development	19.58	10	up	3.10E-09

B

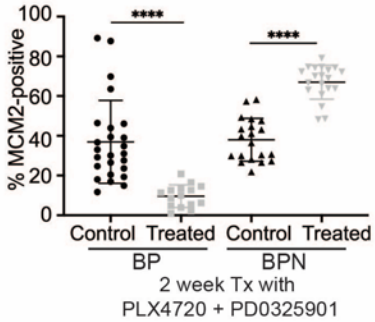

E

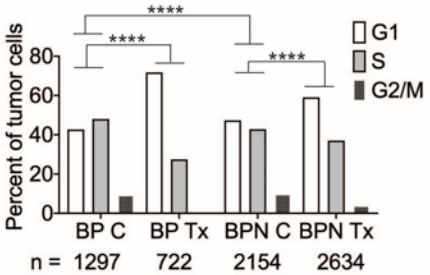

F

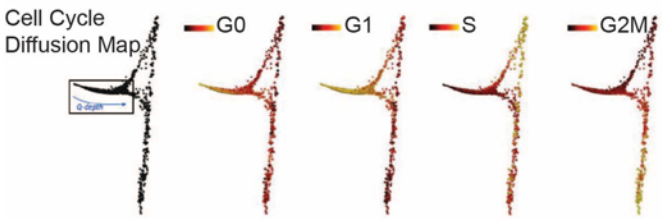

G

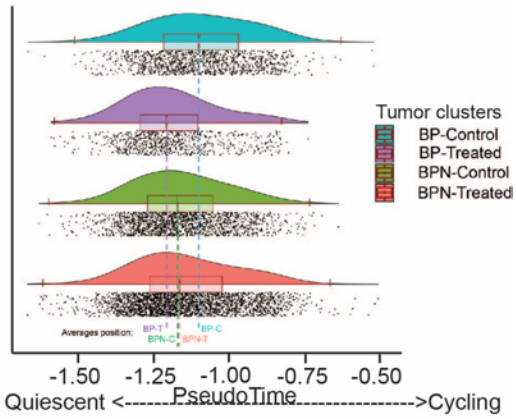

H

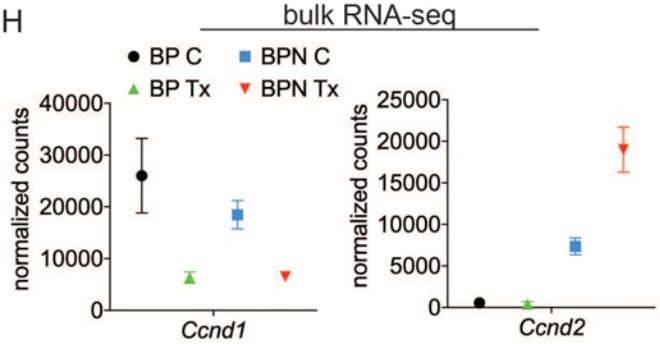

I

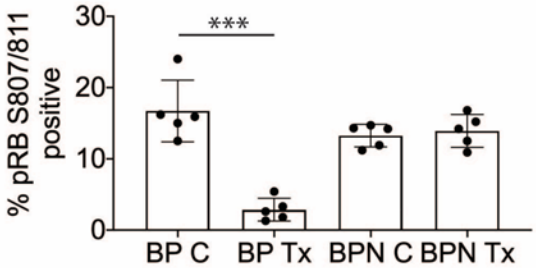

J

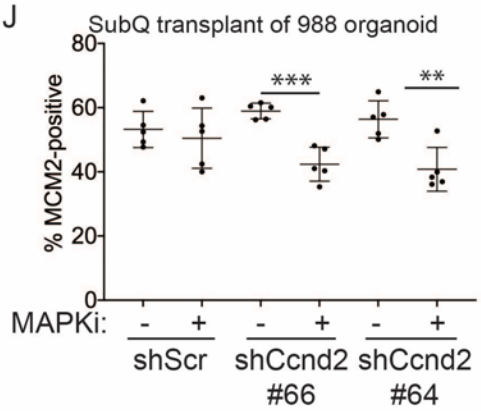

1527

Suppl FIG 5

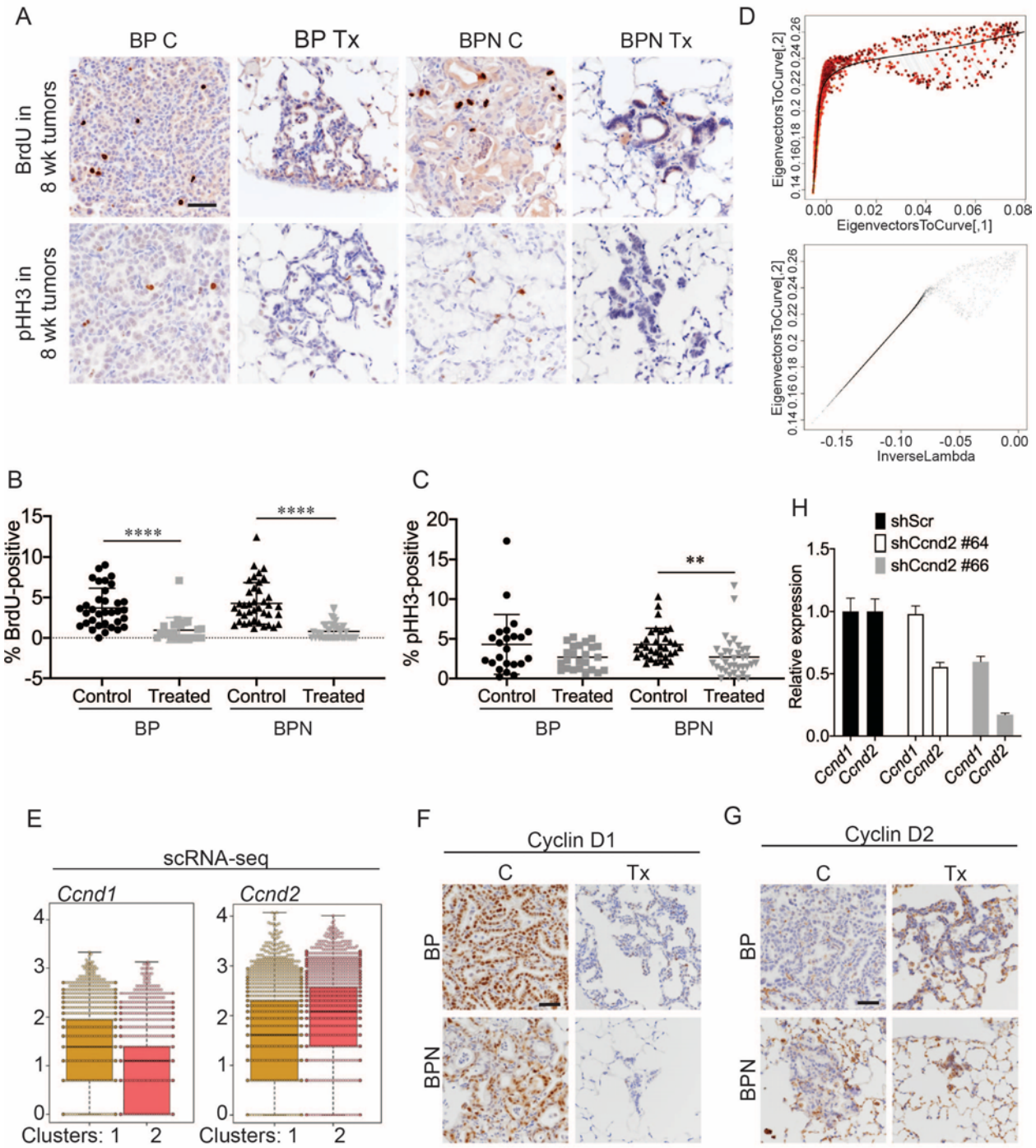

1528

1529

1530

1531 **Figure 5. Differential impact of MAPK inhibitors on the cell cycle in NKX2-1-positive**
1532 **and NKX2-1-negative tumors.**
1533 (A, B) Immunostaining for and quantitation of the proliferation marker MCM2 in tumors
1534 from BP and BPN mice at 8 weeks post-initiation. Control or MAPK-inhibitor infused chow
1535 feeding started at 6 weeks and was maintained for 2 weeks. BP C (25 tumors from 4
1536 mice), BP Tx (15 tumors from 3 mice), BPN C (20 tumors from 3 mice), BPN Tx (20
1537 tumors from 3 mice). Scale bar: 100 μm. Graphs represent mean ± S.D. ****P<0.0001 by
1538 Student's *t*-test. (C, D) Lists of the top-scoring Gene Ontology pathway terms of
1539 differentially expressed genes between control- and drug-chow treated BP (C) or BPN
1540 (D) tumors, as determined by Illumina Correlation Engine analyses of bulk RNAseq data.
1541 UP = enriched in control relative to treated samples. (E) Analysis of cell cycle score in
1542 single cell RNA sequencing data using Seurat package. Utilized cell cycle genes as
1543 defined by Mizuno et al., 2009. ****P<0.0001 by Wilcox test. BP C= clusters 4, 5, 8; BP
1544 Tx= clusters 6, 7; BPN C= clusters 1, 3control; BPN Tx= clusters 2, 3treated (see Fig.
1545 4e). (F) Diffusion map of cell cycle phase signatures in scRNA-seq data showing coherent
1546 enrichment for phase specific signatures at specific graphical regions. >80% of cells are
1547 disturbed in the box that correlates with G0 and G1 signatures and along which we fit a
1548 principle curve to model likely depth of quiescence (Q-depth). (G) Positioning of scRNA-
1549 seq profiles from the indicated cell clusters along the Q-depth curve. BPN control = cluster
1550 1; BPN treated = cluster 2; BP control = cluster 4+5; BP treated = cluster 6+7. (H) Graph
1551 comparing absolute expression levels of *Ccnd1* and *Ccnd2*, data obtained from bulk RNA
1552 sequencing. (I) Quantitation of phospho-RB-positive tumor cells in the indicated tumor
1553 types at 8 weeks post-initiation. Control or MAPK-inhibitor chow feeding started at 6

1554 weeks and was maintained for 2 weeks. Graphs represent mean ± S.D. Multiple lesions
1555 per mouse, for five mice in each cohort, were analyzed. ***P<0.001. (J) Effect of knocking
1556 down CyclinD2 on MCM2 marker expression. A BPN organoid line was stably transduced
1557 with control or *Ccnd2*-targeting shRNA constructs followed by subcutaneous
1558 transplantation and MAPK-inhibitor chow treatment after 8 weeks of growth.
1559 Subcutaneous tumors were harvested after 1 month of drug treatment. MCM2
1560 quantitation was confined to glandular structures that most closely resemble
1561 autochthonous BPN tumors. Graphs are mean ± S.D. ***P < 0.001, **P < 0.01. N=5 mice
1562 per cohort.
1563
1564 The following figure supplement is available for figure 5:
1565
1566 **Figure S5. Differential impact of MAPK inhibitors on the cell cycle in NKX2-1-**
1567 **positive and NKX2-1-negative tumors.**
1568 (A) Detection of proliferation markers, BrdU incorporation and phospho-histone H3 Ser10,
1569 by IHCs in neoplasia arising 8 weeks after tumor initiation with PGK-Cre lentivirus ($5x10^3$
1570 pfu/mouse). At the 6 week timepoint, BP and BPN mice were given control or PLX4720
1571 plus PD0325901 inhibitor chow for 2 weeks. Scale bar: 100 μm. (B) Quantitation of BrdU-
1572 positive tumor cells from mice treated as in (A). Graphs represent mean ± S.D. BP C (34
1573 tumors from 3 mice), BP Tx (23 tumors from 3 mice), BPN C (39 tumors from 3 mice),
1574 BPN Tx (40 tumors from 3 mice) were analyzed. ****P < 0.0001. (C) Quantitation of
1575 phospho-HH3-positive tumor cells from mice treated as in (A). Graphs represent mean ±
1576 S.D. BP C (23 tumors from 2 mice), BP Tx (24 tumors from 2 mice), BPN C (34 tumors

1577 from 2 mice), BPN Tx (34 tumors from 2 mice) were analyzed. ***P* = 0.0058. (D) Graphs
1578 showing how the trajectory for Q-depth was set. Top is a flattened version of the diffusion
1579 map based on arithmetic combination of the first three diffusion components with a
1580 principal curve to the resulting two dimensional graph and bottom plot is a pseudotime
1581 trajectory based on lambda values of the principal curve referred to here as Quiescence
1582 depth and shown on the x-axis. (E) Relative abundance of *Ccnd1* and *Ccnd2* transcripts
1583 in scRNA-seq data on a cell-by-cell basis for clusters 1 and 2. (F, G) Representative IHC
1584 images for Cyclin D1 and Cyclin D2 immunostaining on tumors from BP and BPN mice
1585 at 8 weeks post-initiation. Control or MAPK-inhibitor chow was administered for 2 weeks.
1586 Scale bar: 100 μm. (H) Efficiency of CyclinD2 knockdown by control versus *Ccnd2*-
1587 targeting short hairpins in stably transduced 988 organoids as assessed by qRT-PCR.
1588

FIG 6

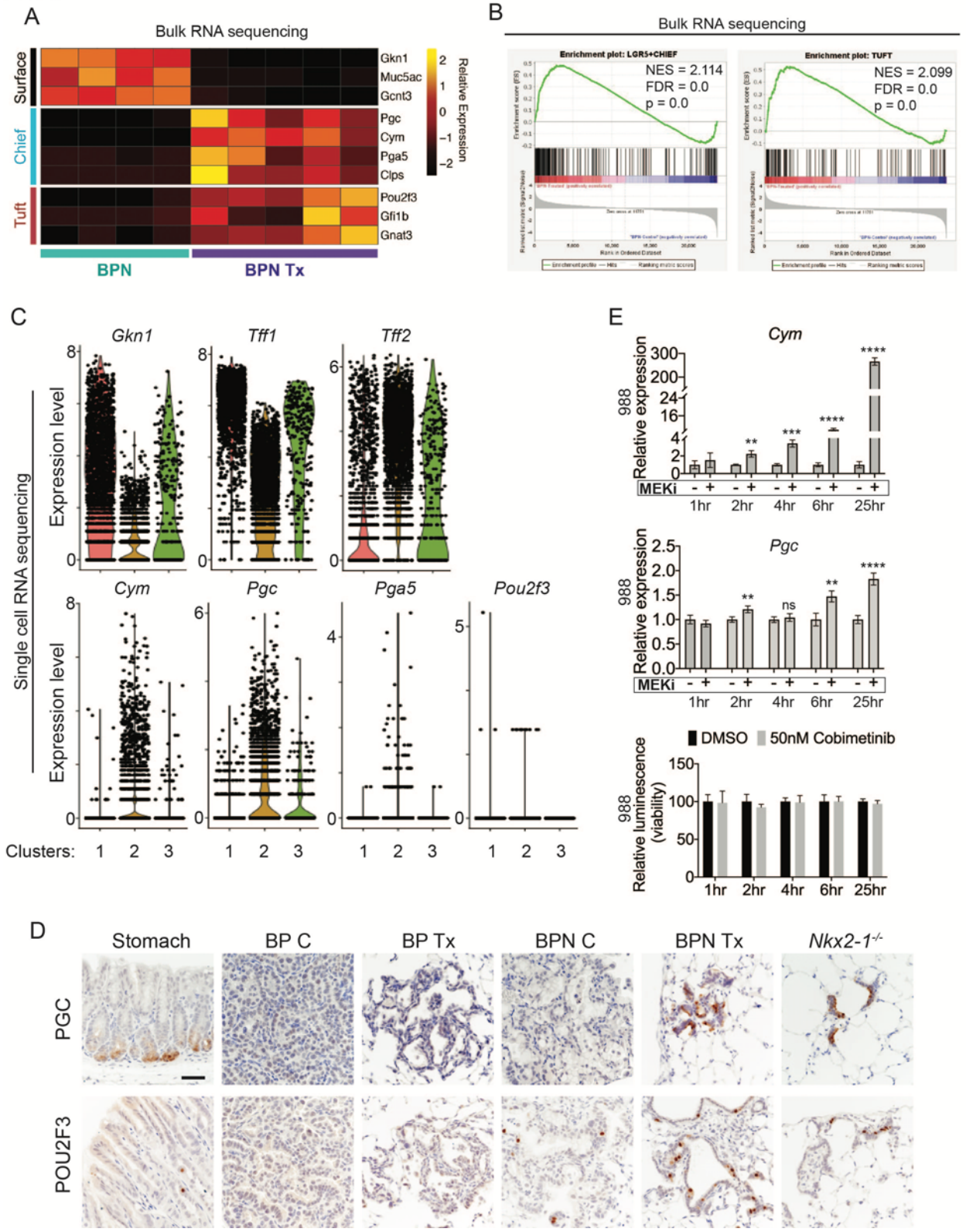
A
Bulk RNA sequencing
Surface
Chief
Tuft
Gkn1
Muc5ac
Gcnt3
Pgc
Cym
Pga5
Clps
Pou2f3
Gfi1b
Gnat3
Relative Expression
BPN
BPN Tx
B
Bulk RNA sequencing
Enrichment plot: LGR5+CHIEF
NES = 2.114
FDR = 0.0
p = 0.0
Enrichment plot: TUFT
NES = 2.099
FDR = 0.0
p = 0.0
C
Single cell RNA sequencing
Expression level
Gkn1
Tff1
Tff2
Cym
Pgc
Pga5
Pou2f3
Clusters: 1 2 3
E
Cym
Pgc
988 Relative expression
MEKi
1hr 2hr 4hr 6hr 25hr
DMSO
50nM Cobimetinib
988 Relative luminescence (viability)
D
Stomach
BP C
BP Tx
BPN C
BPN Tx
Nkx2-1-/-
PGC
POU2F3

1589

Suppl FIG 6

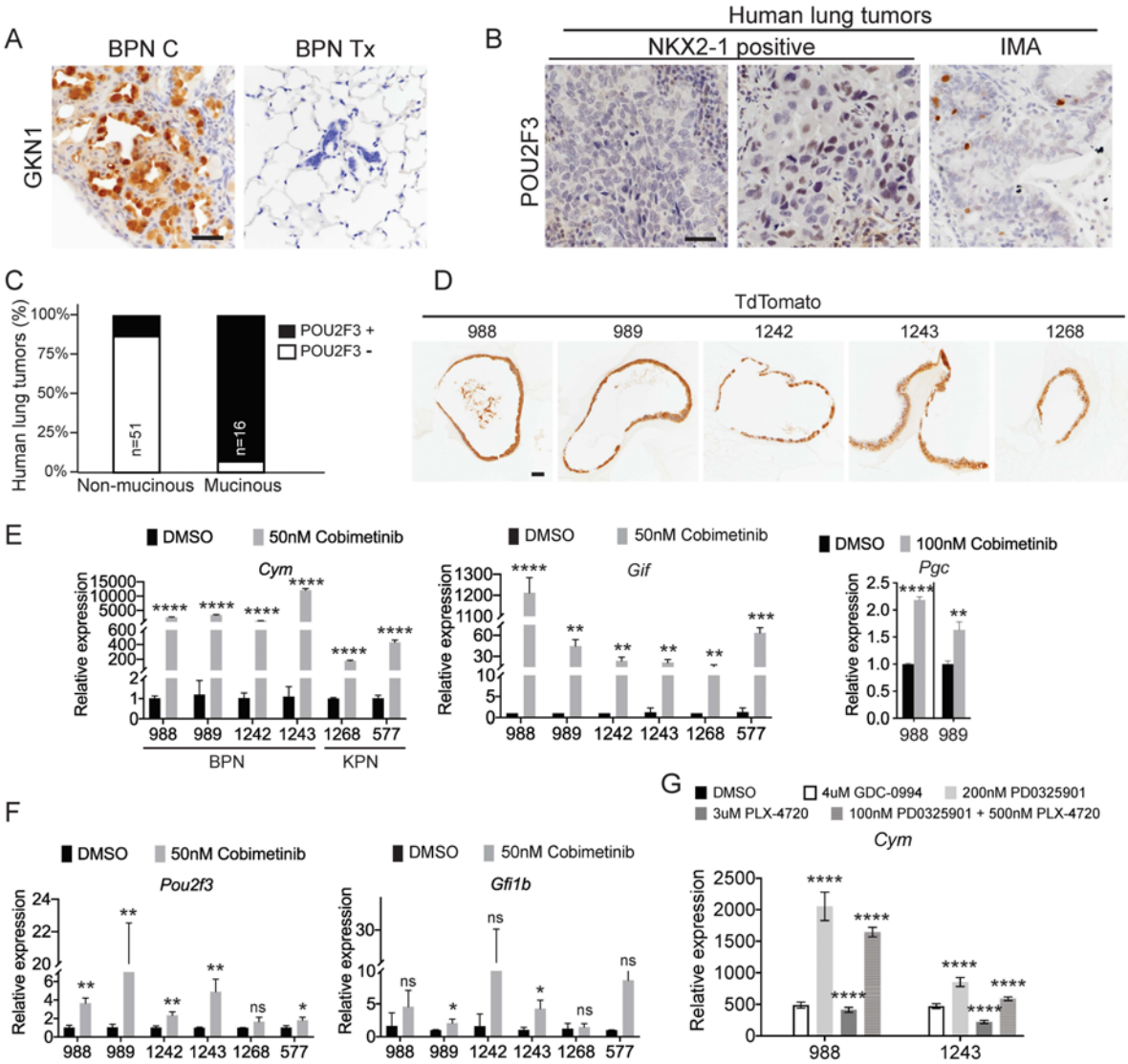

1590

1591

1592 **Figure 6. MAPK activity regulates cellular identity in NKX2-1-negative tumors.**
1593 (A) Transcriptome analysis comparing control BPN cells with drug-treated BPN tumor
1594 cells. Heatmap depicts gastric surface mucous cell markers whose expression diminished
1595 versus gastric chief cell or tuft cell markers whose expression increased in MAPK-inhibitor
1596 treated BPN cells relative to untreated. *adjP*<0.05 for each comparison. RNAseq data
1597 was derived from tdTomato-expressing tumor cells FACS-sorted from BPN mice. 6 weeks
1598 after tumor initiation, mice were treated for 1 week with control chow (n=4) or chow
1599 containing $BRAF^{V600E}$ inhibitor plus MEK inhibitor (n=5). (B) GSEA against chief and tuft
1600 cell signatures. (C) Violin plots of single cell sequencing data showing expression levels
1601 of *Gkn1*, *Tff1*, *Tff2*, *Cym*, *Pgc*, *Pga5* and *Pou2f3* transcripts in BPN tumor clusters 1-3
1602 and highlighting key drug-mediated cell-identity changes. (D) IHC for a gastric chief cell
1603 marker (Pepsinogen C) and a tuft cell marker (POU2F3) on LUAD sections derived 7
1604 weeks following tumor initiation with PGK-Cre lentivirus ($5x10^3$ pfu/mouse). At 6 weeks,
1605 *BRaf*$^{CA/+}$*;Trp53*$^{f/f}$*;Nkx2-1*$^{f/+}$*;Rosa26*$^{tdTomato/tdTomato}$ and *BRaf*$^{CA/+}$*;Trp53*$^{f/f}$*;Nkx2-*
1606 *1*$^{f/f}$*;Rosa26*$^{tdTomato/tdTomato}$ mice were given control or MAPK-inhibitor chow for 1 week. Also
1607 shown are sections of normal stomach epithelium as positive controls. Note that in
1608 hyperplasia that arise from *Nkx2-1* deletion in distal lung without concomitant oncogenic
1609 activation also upregulate these lineage-restricted markers. *Nkx2-1*$^{f/f}$ mice were infected
1610 with Ad5-Spc-Cre (10^9 pfu/mouse). Lungs were harvested 16 weeks later. Scale bar: 100
1611 μm. (E) Chief cell markers are rapidly induced in tumor organoids treated with 50nM
1612 Cobimetinib. qRT-PCR analysis of chief cell markers *Cym* and *Pgc* on RNA isolated from
1613 drug/DMSO treated organoids for the indicated times. Data are mean ± S.D. ****P<
1614 0.0001, ***P<0.001, **P<0.01, ns= not significant. A representative experiment of three

1615 is shown. Bottom plot: Measurement of viability in organoid cultures treated with vehicle
1616 or Cobimetinib using 3D CellTiter-Glo Luminescent cell viability assay at the indicated
1617 timepoints. Data are mean ± S.D. A representative experiment of three is shown.
1618
1619 The following figure supplement is available for figure 6:
1620
1621 **Figure S6. MAPK activity regulates cellular identity in NKX2-1-negative tumors.**
1622 A) IHC for detection of the surface neck mucous marker, GKN1, in control BPNs and BPN
1623 tumors that were treated with drug chow for 2 weeks. Scale bar: 100 μm. (B) IHC for the
1624 tuft cell marker, POU2F3, in human non-mucinous lung adenocarcinoma and IMA tumors.
1625 Scale bar: 100 μm. (C) Percentage of NKX2-1^{+} and NKX2-1^{-} human lung
1626 adenocarcinomas that contain POU2F3-positive tumor cells. (D) Immunostaining for
1627 tdTomato on BPN and KPN organoid FFPE sections indicating that primary spheroid
1628 cultures contain only tumor-derived epithelial cells. (E-G) qRT-PCR determination of the
1629 expression levels of select stomach epithelium lineage markers in multiple lung tumor
1630 organoid lines. Spheroid cultures were established from *BRaf*$^{CA/+}$*;Trp53*$^{f/f}$*;Nkx2-*
1631 *1*$^{f/f}$*;Rosa26*$^{tdTomato/tdTomato}$ mice (for BPN lines: 988, 989, 1242 and 1243), or for the KPN
1632 lines from *KRas*$^{LSL-G12D/+}$*;Trp53*$^{f/f}$*;Nkx2-1*$^{f/f}$*;Rosa26*$^{tdTomato/tdTomato}$ mice (for 1268), and from
1633 tamoxifen treated *KRas*$^{FSF-G12D/+}$*;Trp53*$^{frt/frt}$*;Nkx2-1*$^{f/f}$*;Rosa26*$^{FSF-CreERT2/CreERT2}$ mice (for
1634 577). Spheroids were subsequently cultured long term in 50% L-WRN conditioned media.
1635 For experiments, organoids were seeded (day 0) and allowed to recover overnight in the
1636 absence of DMSO/inhibitors. In each case, data are presented as fold change (mean ±
1637 S.D.) compared with DMSO control values. (E, F) RNA derived from indicated BPN and

1638 KPN organoid lines that had been treated with DMSO or Cobimetinib for 72 hours. (E)
1639 qRT-PCR for detection of markers of gastric gland base cell types. (F) qRT-PCR for
1640 detection of tuft cell-specific transcripts. Data shown for each marker are representative
1641 of least 3 independent experiments. (G) Chief cell marker, *Cym*, is significantly induced
1642 in organoids treated with additional MAPK-pathway inhibitors for 24 hours: GDC-0994
1643 (ERKi), PD0325901 (MEKi), and PLX4720 (BRAFi). Data is representative of two
1644 independent experiments. (E – G) ****P< 0.0001, ***P<0.001, **P<0.01, *P<0.05, ns= not
1645 significant.

FIG 7

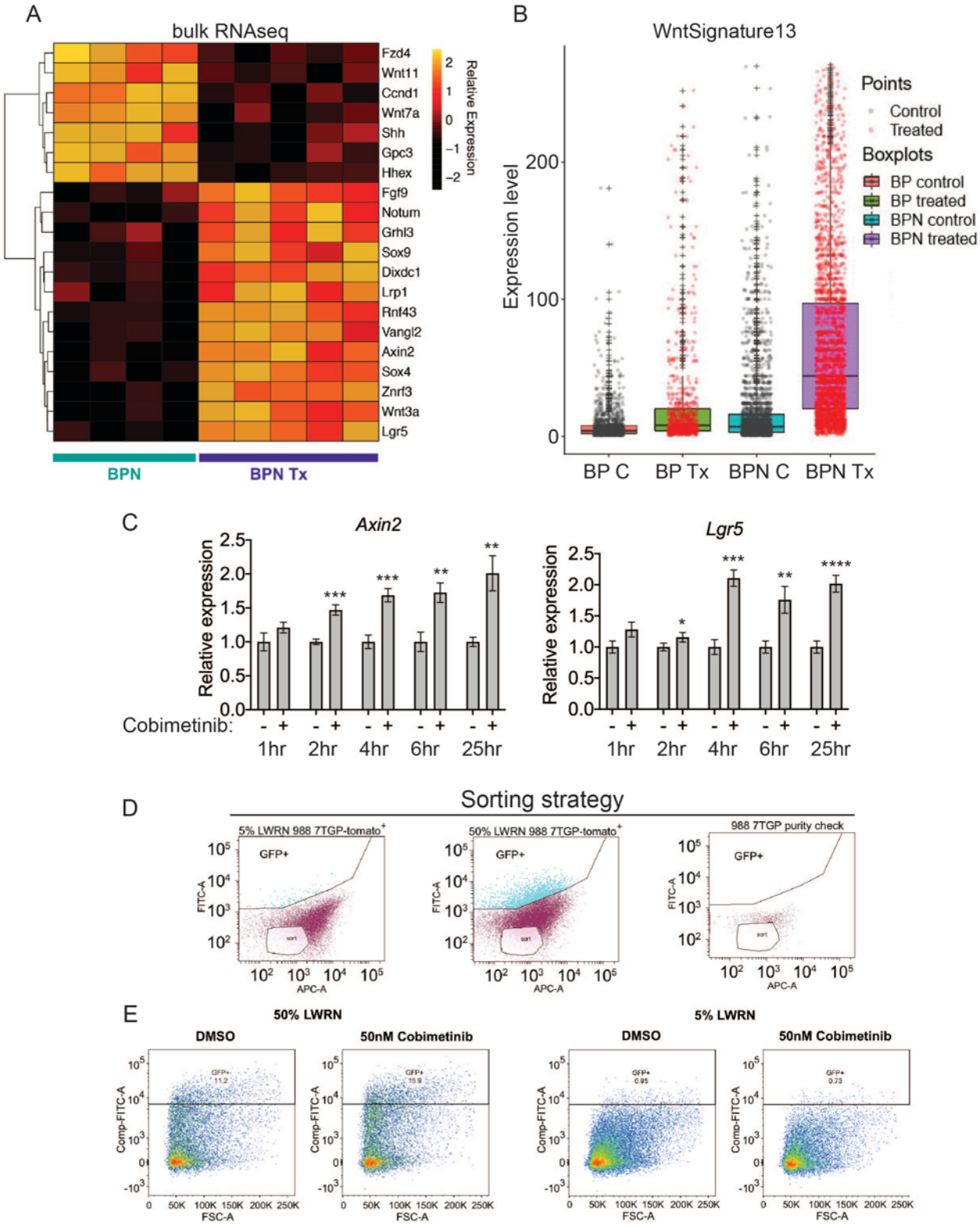
A
bulk RNAseq
Fzd4
Wnt11
Ccnd1
Wnt7a
Shh
Gpc3
Hhex
Fgf9
Notum
Grhl3
Sox9
Dixdc1
Lrp1
Rnf43
Vangl2
Axin2
Sox4
Znrf3
Wnt3a
Lgr5
Relative Expression
BPN
BPN Tx
B
WntSignature13
Expression level
Points
Control
Treated
Boxplots
BP control
BP treated
BPN control
BPN treated
BP C
BP Tx
BPN C
BPN Tx
C
Axin2
Lgr5
Relative expression
Cobimetinib:
1hr
2hr
4hr
6hr
25hr
D
Sorting strategy
5% LWRN 988 7TGP-tomato+
50% LWRN 988 7TGP-tomato+
988 7TGP purity check
GFP+
FITC-A
APC-A
E
50% LWRN
5% LWRN
DMSO
50nM Cobimetinib
Comp-FITC-A
FSC-A

1649

Suppl FIG 7

A

Bulk RNAseq

BPN C vs BPN Tx Upstream Regulators analysis by IPA		
Upstream regulator	**Activation Z-score**	**P-value of overlap**
IL10RA	-1.786	2.02E-12
CTNNB1	-0.105	1.24E-11
TGFB1	0.114	3.57E-10
PDGF BB	-1.511	1.6E-09
JUN	1.676	2.93E-09

B

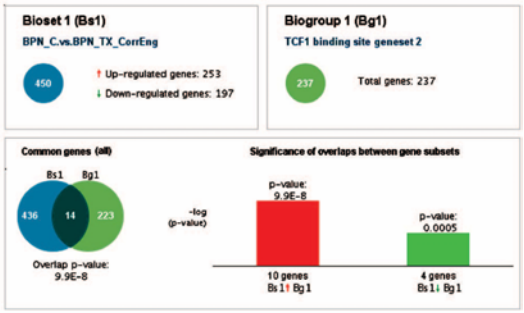

C

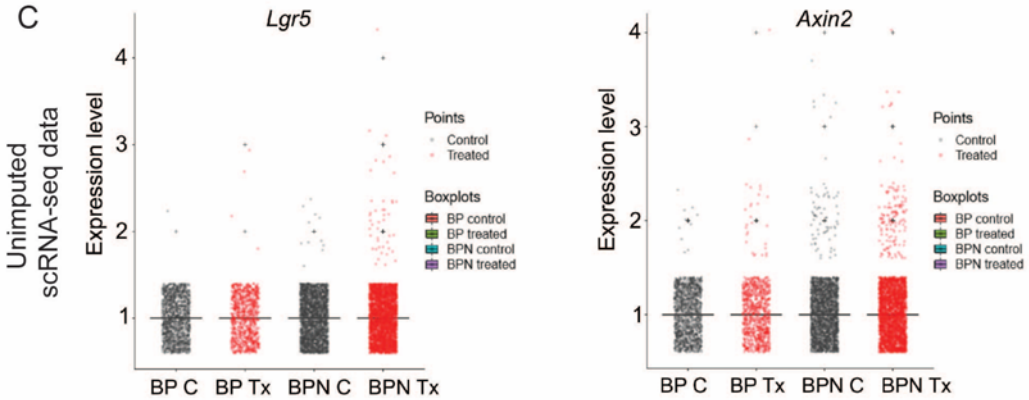

D

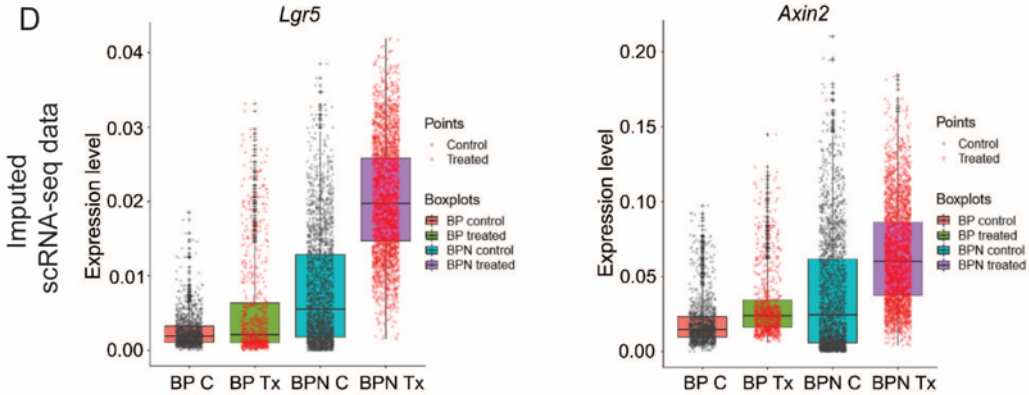

E

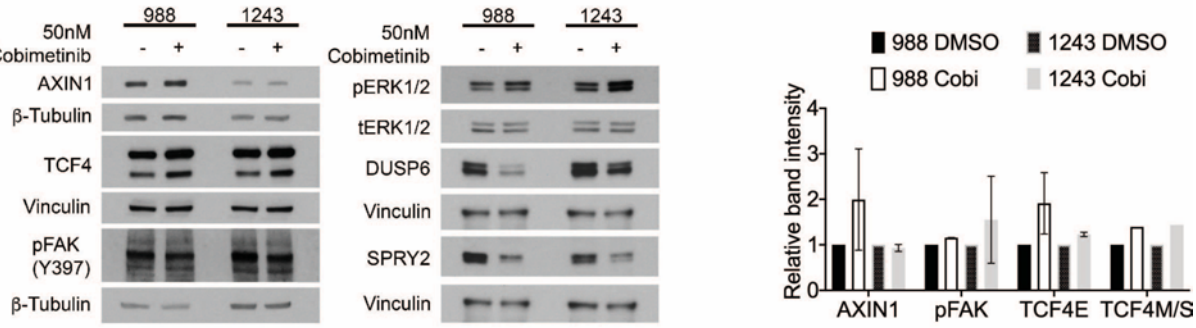

1650
1651

1652 **Figure 7. MAPK inhibition activates WNT signaling in NKX2-1-negative tumors.**
1653 (A) Transcriptome analysis of genes comprising the canonical WNT pathway gene
1654 ontology (AmiGO) in RNA purified from FACS-sorted BPN tumor cells 1 week post-
1655 treatment with PLX4720+PD0325901 or control chow. *adjP*<0.05 for each comparison.
1656 Color key indicates normalized expression levels (Log10). (B) Analysis of WNT pathway
1657 activity in scRNAseq data using a WNT activation signature. BP indicates cells from
1658 clusters 4-8; BPN indicates cells from clusters 1-3 (see Fig. 4e-f). C: control, Tx= drug
1659 treatment. (C) Kinetics of WNT signaling induction following MAPK-inhibitor treatment as
1660 indicated by qRT-PCR analysis of the canonical WNT signaling markers, *Axin2* and *Lgr5*,
1661 on RNA isolated from drug/DMSO treated organoids for the indicated times. Data are
1662 mean ± S.D. A representative experiment of three is shown. ****P< 0.0001, ***P<0.001,
1663 **P<0.01, *P<0.05. (D, E) WNT-low cells can give rise to WNT-high cells. BPN organoid
1664 lines, 988 shown here, were stably transduced with a WNT-reporter construct (7TGP,
1665 Addgene Plasmid #24305) and FACS-sorted to isolate cells with undetectable WNT
1666 activity (pink gate) (D). (E) Dynamics of sorted WNT-low cells when cultured in WNT rich
1667 spheroid media (50% LWRN vs. 5% LWRN) or in the presence of MEK-inhibitor. Numbers
1668 shown are the percentage of live tdTomato^{+}GFP^{+} cells in each culture as quantified by
1669 flow cytometry (FlowJo). Data shown is a representative of two independent sorting
1670 experiments.
1671
1672
1673
1674

1675 The following figure supplement is available for figure 7:

1676

1677 **Figure S7. MAPK inhibition activates WNT signaling in NKX2-1-negative tumors.**

1678 (A) List of the top-scoring genes in IPA Upstream Regulator analysis when comparing
1679 differentially expressed genes between control- and drug-chow treated BPN tumors in
1680 bulk RNA sequencing data. (B) Regulator Motif analysis by Illumina Correlation Engine
1681 identifies significant differences in TCF1 binding site genesets between control and
1682 treated BPN tumors. (C, D) Plots of normalized raw and imputed expression values for
1683 *Lgr5* and *Axin2* transcripts in scRNA-seq data as readouts of canonical WNT activation
1684 levels in indicated clusters. (E) Candidate mechanisms by which a cross-talk between
1685 ERK and WNT pathways can occur as evaluated by immunoblotting. Representative
1686 western blot image and quantitation of band intensity (ImageJ) from two independent
1687 experiments is provided. None of the changes in protein abundance between control and
1688 drug treated (24 hours) organoid samples are statistically significant. Graphs indicate
1689 mean ± S.D.

FIG 8

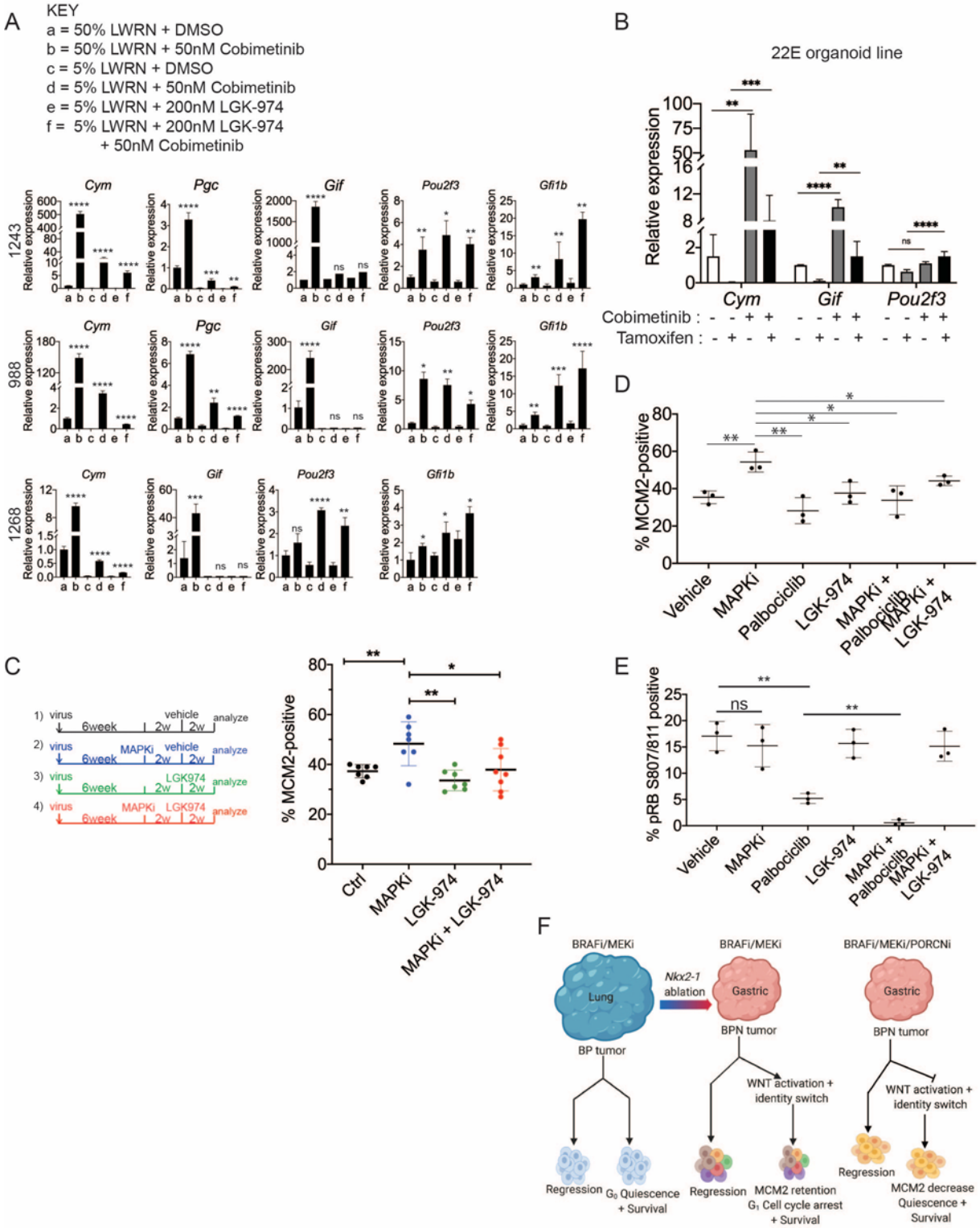

1690
1691

Suppl FIG 8

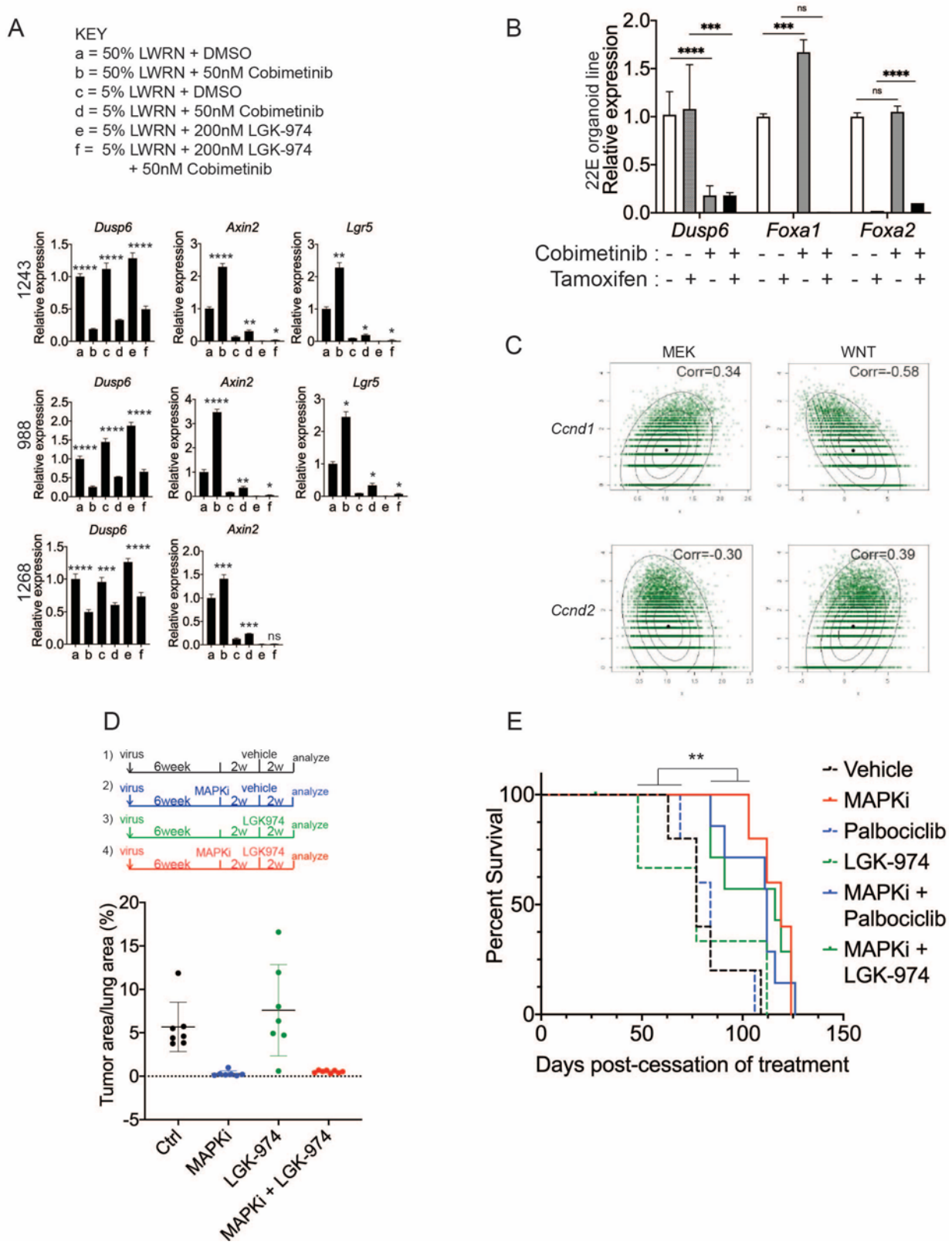

1692

1693 **Figure 8. WNT signaling and the transcription factors FoxA1/FoxA2 are partially**
1694 **required for lineage switching induced by MAPK inhibition.**
1695 (A) Analyses of indicated gene expression levels in BPN (1243 and 988) and KPN (1268)
1696 tumor organoid lines by qRT-PCR at 24 hours and under different treatment conditions.
1697 Organoids were cultured in 50% L-WRN (a, b) or reduced 5% L-WRN media (c, d, e, f)
1698 and treated with DMSO (a, c), single agent Cobimetinib (b, d) or the Porcupine inhibitor,
1699 LGK-974 (e), and both inhibitors (f). Graphs indicate mean ± S.D. [*P*values are for *a-b*;
1700 *c-d*; or *e-f* comparisons]. Experiment was reproducibly performed 3 times. (B) qRT-PCR
1701 analysis of the expression levels of indicated cell identity markers in the 22E organoid line
1702 under four different conditions. 22E, a KF1F2 organoid line, lacks NKX2-1 expression and
1703 harbors conditional alleles of *Foxa1* and *Foxa2*. Tamoxifen treatment induces Cre^{ERT2}-
1704 mediated *Foxa1*/*Foxa2* deletion. Data are mean ± S.D and a pool of two independent
1705 experiments. ***$P < 0.001$, **$P < 0.01$. (C) Quantitation of the proliferation marker MCM2
1706 in 10 week autochthonous BPN lung tumors under four different treatment conditions: 1)
1707 control (n=7); 2) MAPK-inhibitor chow (n=7); 3) LGK-974 (n=7); and 4) MAPK-inhibitor
1708 chow and LGK-974 (n=8). (D, E) Abundance of MCM2 or phospho-RB positive cells in 10
1709 week autochthonous lung tumors from BPN mice under the indicated conditions. Vehicle
1710 or drug treatments were administered at 6 weeks post tumor initiation for 4 weeks.
1711 Multiple tumors from n=3 mice/group were quantitated. (A – E) ****$P < 0.0001$, ***$P<0.001$,
1712 **$P<0.01$, *$P<0.05$, ns= not significant. (F) Graphical depiction of the molecular and
1713 pharmacological regulation of differentiation programs in LUAD (BioRender). Here, we
1714 investigated genotype-specific drug response. Cancer therapy triggers two alternative
1715 fates in drug-treated tumors of both genotypes: either regression or survival in a drug

1716 tolerant state. Molecularly, the drug tolerant state appears distinct in BP versus BPN
1717 tumors and can be exploited pharmacologically by targeting the cell cycle and/or drug-
1718 induced signaling pathways.
1719
1720 The following figure supplement is available for figure 8:
1721
1722 **Figure S8. WNT signaling and the transcription factors FoxA1/FoxA2 are partially**
1723 **required for lineage switching induced by MAPK inhibition.**
1724 (A) Analyses of indicated gene expression levels in BPN (1243 and 988) and KPN (1268)
1725 tumor organoid lines by qRT-PCR at 24 hours and under different treatment conditions.
1726 Organoids were cultured in 50% L-WRN (a, b) or reduced 5% L-WRN media (c, d, e, f)
1727 and treated with DMSO (a, c), single agent Cobimetinib (b, d) or the Porcupine inhibitor,
1728 LGK-974 (e), and both inhibitors (f). Graphs indicate mean±S.D. ****P< 0.0001,
1729 ***P<0.001, **P<0.01, *P<0.05, ns= not significant. [Pvalues are for *a-b*; *c-d*; or *e-f*
1730 comparisons]. Experiment was reproducibly performed 3 times. (B) qRT-PCR analysis of
1731 indicated gene expression in a KPNF1F2 organoid line under MEK inhibition
1732 (Cobimetinib) and/or tamoxifen induced *Foxa1* and *Foxa2* deletion. Data are mean ± S.D
1733 and a representative of two independent experiments. ****P < 0.0001, ***P < 0.001, ns=
1734 not significant. (C) Density plots and correlation values for a MEK activation signature (x-
1735 axis left two panels) and a WNT signature (x-axis right two panels) versus *Ccnd1* and
1736 *Ccnd2* transcript levels as indicated based on scRNA-seq. (D) Quantitation of lung tumor
1737 burden 10 weeks post-initiation in BPN mice under four different treatment conditions: 1)
1738 control (n=7); 2) MAPK-inhibitor chow (n=7); 3) LGK-974 (n=7); and 4) MAPK-inhibitor

1739 chow and LGK-974 (n=8). (E) Overall survival of BPN tumor bearing mice that were
1740 enrolled in 6 different treatment conditions for 4 weeks. Vehicle (n=5), MAPK-inhibitor
1741 chow (n=5), Palbociclib (n=5), LGK-974 (n=4); MAPK-inhibitor chow + Palbociclib (n=7),
1742 and MAPK-inhibitor chow + LGK-974 (n=7). ***P*=0.0017 by Log-rank test.
1743